Statics and Dynamics of Fluctuations in Interfaces Driven by Non-uniform Fields

A THESIS SUBMITTED FOR

THE DEGREE OF DOCTOR OF PHILOSOPHY (SCIENCE)

OF THE UNIVERSITY OF JADAVPUR

Abhishek Chaudhuri

S. N. Bose National Centre for Basic Sciences

Block - JD, Sector-III, Salt Lake

Kolkata - 700 098, India

January 2006

CERTIFICATE FROM THE SUPERVISOR

This is to certify that the thesis entitled "**Statics and Dynamics of Fluctuations in Interfaces Driven by Non-uniform Fields**" submitted by **Sri Abhishek Chaudhuri**, who got his name registered on **11th May, 2004** for the award of **Ph.D.(Science) degree of Jadavpur University** , is absolutely based upon his own work under the supervision of **Dr. Surajit Sengupta** and that neither this thesis nor any part of its has been submitted for any degree / diploma or any other academic award anywhere before.

Date:

<div align="right">

Surajit Sengupta
Reader
S. N. Bose National Centre for Basic Sciences
Block-JD, Sector-III, Salt Lake, Kolkata - 700098, India

</div>

Acknowlegements

First, I would like to thank my supervisor, Surajit Sengupta, for his continuous support in the Ph.D program. He was always there to listen and to give advice. Interactions with him were always so friendly that it gave me ample opportunity to ask questions and express my ideas. He showed me the different ways to approach a research problem and always insisted on staying focussed and working hard. It has really been a wonderful experience working with him.

I would like to thank my collaborators, P. A. Sreeram and Debasish Chaudhuri at S. N. Bose National Centre for Basic Sciences (SNBNCBS), and Madan Rao at Raman Research Institute. Sreeram helped me make my life with computers much simpler than I would have imagined. I enjoyed working with him. Madan always impressed me with his ideas and his encouragement to do good work. The innumerable discussions that I had with Debasish during my Ph.D program helped me to understand the diverse aspects of my research problem. He has been a guiding force in my research work. He was always there to meet and talk about my ideas, to proofread, and to ask me good questions to help me think through my problems.

As for other members of our group, I would like to thank Ankush Sengupta, with whom I have always shared a brotherly relationship. His vibrancy and wonderful attitude always kept me going and academic discussions with him are also acknowledged. Tamoghna and Arya always brought with them a breath of fresh air and interacting with them was fun. They provided the much needed boost in the final year of my Ph.D and helped a lot while I was writing my thesis.

I would like to acknowledge helpful discussions with M. Barma (Tata Institute of Fundamental Research), J. Krug (Universität Essen, Germany), J. K. Bhattacharya (Indian Association for the Cultivation of Science), S. N. Majumdar (CNRS, France), G. I. Menon (Indian Institute of Mathematical Sciences), P.B. Sunil Kumar (I.I.T. Chennai), A. Mookerjee, S. S. Manna and A. K. Raychaudhuri (SNBNCBS) during the course of my research work. A special thanks to P.B. Sunil Kumar and G. I. Menon and all the folks at Sunil's lab for the wonderful time that I had at Chennai during my visit there. I would also like to acknowledge the Council of Scientific and

List of Publications

I. articles in journals/contributions to books/unpublished eprints:

[1] Abhishek Chaudhuri, Surajit Sengupta and Madan Rao, *Stress relaxation in a perfect nanocrystal by coherent ejection of lattice layers*, Phys. Rev. Lett. **95**, 266103 (2005).

[2] Abhishek Chaudhuri, P. A. Sreeram and Surajit Sengupta, *A Kinetics driven commensurate - incommensurate transition*, Phase Transitions **77**, 691 (2004).

[3] Abhishek Chaudhuri, P. A. Sreeram and Surajit Sengupta, *Growing smooth interfaces with inhomogeneous, moving external fields: dynamical transitions, devil's staircases and self-assembled ripples*, Phys. Rev. Lett. **89**, 176101 (2002).

II. published contributions in academic conferences:

[1] Abhishek Chaudhuri, Debasish Chaudhuri and Surajit Sengupta, *Induced Interfaces at Nano-scales: Structure and Dynamics*, International Journal of Nanoscience 2005 (in press). Proceedings of International Conference on Nanoscience and Technology, Hyaat Regency, Kolkata, 17-20 December 2003.

[2] Abhishek Chaudhuri and Surajit Sengupta, *Profile-driven interfaces in 1+1 dimensions: periodic steady states, dynamical melting and detachment*, Physica A, **318**, 30 (2003). Proceedings of the International conference on Statistical Physics, Statphys - Kolkata IV, IACS, Kolkata (14-16 January, 2002) and SNBNCBS, Kolkata (17-19 January, 2002).

Abstract

In the study of condensed matter systems, a paradigm which is very generally invoked is that of a ground state and its low energy excitations. A classical solid, for example, is a periodic crystal with low energy, long wavelength phonon fluctuations. Often these low energy excitations appear due to the complete or partial breaking of a spatial symmetry e.g. rotational or translational symmetry. What happens if explicit constraints are introduced such that these low energy modes are unavailable?

This question has assumed some importance in recent years due to the advent of nano technology and the growing use of nanometer scale devices and structures. In a small system, the size limits the scale of the fluctuations and makes it imperative for us to understand how the response of the system is altered in such a situation. In this thesis, this question is answered for the special case of interfacial fluctuations in two dimensions (2d). The energy of an interface between two phases in equilibrium is invariant with respect to translations perpendicular to the plane (or line in 2d) of the interface. We study the consequence of breaking this symmetry explicity using an external field gradient. One expects that since low energy excitations are suppressed, the interface would be flat and inert at all times. We show that surprisingly there are novel fluctuations and phenomena associated with such constrained interfaces which have static as well as dynamic consequences.

After a couple of chapters containing introductory material on interfaces, in Chapter 3 we investigate static and dynamic properties of an Ising interface defined on a 2d oriented square lattice. The interface is constrained by a non-uniform external field with a profile which is such that the field changes sign across a (straight) line which we call the "edge" of the profile. The Ising interface lies as close to the edge as possible and the presence of the symmetry breaking field suppresses long wavelength interfacial fluctuations as expected. The interface therefore remains essentially flat over long length scales. At short scales of the order of a few lattice parameters, however, the interface begins to show "self-assembled" patterns depending on the orientation of the edge. These patterns may be indexed by all possible rational fractions. The energy of the interface depends on the index of the rational fraction and the interface deforms locally to conform to low energy states. The local orientation of the interface plotted as a function of

the average orientation shows a complete Devil's staircase structure. If the external field profile is now translated perpendicular to the interface with a fixed velocity, the interface follows the profile, but we now have transitions among the patterns which occur in a way so as to render the Devil's staircase incomplete. Low index patterns are stable while patterns indexed by higher order rationals either transform to low index ones or remain "amorphous" i.e. fluctuate randomly between nearby stable states. At very high velocities the interface detaches from the field edge and coarsens dynamically. We believe that our results have some relevance on real crystal growing techniques apart from being of theoretical interest due to the presence of an infinite hierarchy of driven dynamical transitions.

The later part of the thesis deals with a more realistic interface (also in 2d) namely that between a classical liquid and a solid. Similar to the Ising interface, this is created using a chemical potential field in the form of an atomic trap. The presence of the trap allows the atoms to condense into a solid which is separated from the surrounding liquid by a liquid solid interface. For reasons similar to the Ising case, the interface is flat and "crystallization waves" which normally tend to roughen a solid liquid interface are suppressed. The small size solid thus formed can exchange particles with the liquid through the interface. We show that this transfer of particles happens predominantly by a coherent addition and removal of entire atomic layers as the depth of the potential well is changed. The elastic energy cost of flaking off incomplete layers is prohibitively large if the thickness of the crystal is below a certain critical amount. This ensures that only whole, single, layers are exchanged. This provides a novel mechanism of stress relaxation in a nano-sized single crystal. Topological defects like dislocations tend to destroy this coherence but are rapidly eliminated once they appear on the interface as steps.

Finally, we study momentum and energy transfer across the liquid solid interface in the presence of this "layering" transition using molecular dynamics simulations. With the depth of the potential held close to the value required for a layering transition, a tiny momentum pulse is generated, near a free surface of the crystal. The pulse travels as a shock wave through the solid and emerges on the other side taking with it an entire crystal layer; the ejected layer carrying away a definite amount of momentum and energy behaving, as it were, like a coherent "quasi particle" in a completely classical context. This results in a prominent peak in the absorption spectrum. We believe that this driven layer ejection may have practical applications apart from its interest from a fundamental viewpoint. The transfer of energy through the interface is characterized by the Kapitza or contact resistance which we measure using non-equilibrium molecular dynamics where a temperature gradient is setup using proper boundary conditions. We observe that the Kapitza resistance shows a discontinuity at the layering transition. This may enable one in future to design interfaces with controllable thermal properties

Contents

1 Introduction to interfaces and summary of the thesis

To a large extent, the properties of most everyday materials are determined by the properties of their internal interfaces [1, 2]. This is equally true, for example for a block of steel, where grain boundaries interact with dislocations to produce hardness and resistance to plastic deformation, or a catalytic convertor in an automobile exhaust where interface properties control crucial chemical reactions, or in a mammalian lung tissue where lung surfactants residing in the inner lining of alveoli reduce the amount of work required in breathing and thereby contribute directly to the survival of the organism.

It is therefore obvious that any means that we discover, which alters the properties of interfaces will have a profound effect on the overall structure and properties of many materials of technological importance. Indeed, a large amount of work exists [3–5] which attempts precisely that. Interfacial properties may be altered using alloying elements [6] which either segregate or prevents segregation of specific elements at interfaces, surfactants [7] which reduce the surface tension, stress etc.

In this thesis, we explore the possibility of tuning interfacial structure and properties using non-uniform external fields. We show that large potential gradients at interfaces reduces the dominant low-energy, long wavelength fluctuations. Instead of such interfaces becoming inert, however we show that novel fluctuations are generated which lead to interesting behaviour which may have some technological applications. Such fine tuning of interfacial fluctuations may be of use in the emerging area of nanotechnology [8] where the properties of interfaces at the length and time scales of interest in this thesis, is crucial.

We begin this chapter by providing a brief introduction to the thermodynamics of interfaces followed by a discussion of the dominant low energy equilibrium fluctuations. We then introduce the basic paradigms for understanding the dynamics of driven interfaces. We end this chapter with a systematic overview and summary of the rest of the chapters of this thesis.

1.1 Definition of interfaces and interfacial region

By definition, bulk phases are regions of configuration space associated with a global minimum of an appropriate free energy. Often, instead of a single phase, one obtains a mixture of two or more phases which coexist. The region in-between two coexisting bulk phases is an interface, a surface being simply an interface where one of the bulk phases happens to be a gas or vacuum. An interface can also be composed of a material that is different from the two bulk phases such as surface coatings, epitaxial layers and membranes composed of amphiphilic molecules that may lie between bulk domains of water and oil. Although one may think of an interface as being of negligible thickness, in fact the thickness of the interfacial region is significant and definitely non-zero, when we consider phenomena occurring at nano-meter scales.

Any intensive property, such as density, varying from, say, its value in a liquid phase through the interface to a gas phase gives a plot such as that in Fig. 1.1. In this case the density shows
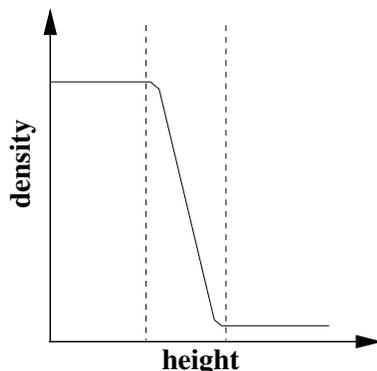
FIGURE 1.1: Variation of density from the high density liquid to the lower density gas phase. Dashed lines indicate the interfacial region

a smooth transition from the high density of the liquid to the much lower density of the gas. The bulk phases can be separated from the interface by two surfaces parallel to one another and positioned so that the bulk phases are homogeneous and uniform (uniform density in this case) while the inhomogeneity and non-uniformity are connected entirely within the interfacial region lying between the two surfaces. The dashed lines in Fig. 1.1 illustrate this point. However we should note that for some properties the transition from one bulk phase to another does not follow a smooth monotonic form such as that in Fig. 1.1. Instead we may have a behavior as shown in Fig. 1.2. As an example, the concentration of some solutes at the gas-solution interface may reach values much higher than those in either bulk phase and exhibit a profile such as that in Fig. 1.2(a). Such quantities are said to show an interfacial excess. Conversely, there may be relative depletion of the concentration of a solute at an interface (Fig. 1.2(b))
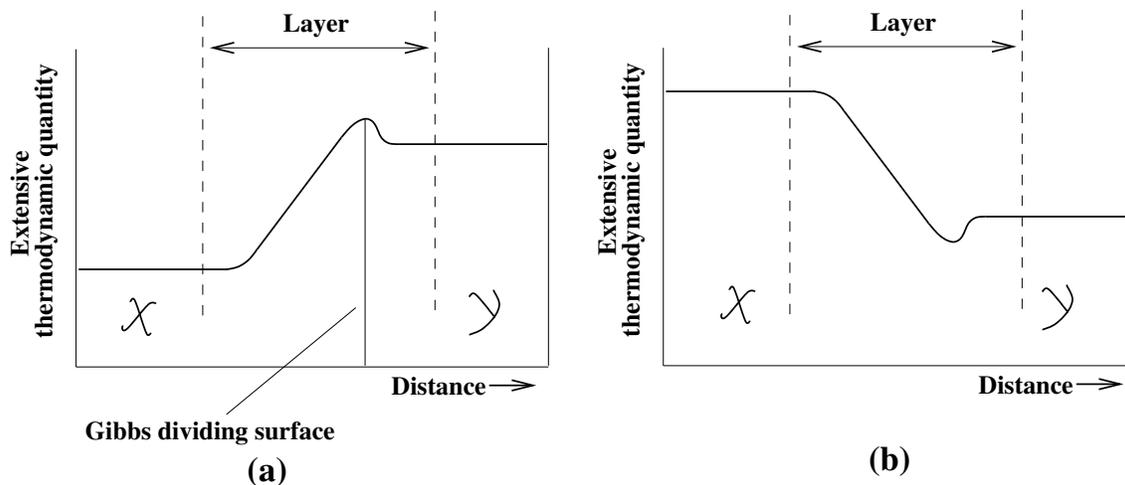
FIGURE 1.2: (a) Variation of an extensive thermodynamic quantity with distance across an interface between $\mathcal{X}$ and $\mathcal{Y}$ phases. The layer between the two dashed lines includes the interfacial region. Also shown is the "dividing surface" of Gibbs (b) Variation of the same except that here there is a relative depletion as opposed to interface excess in (a).

1.2 The thermodynamics of interfaces

Given the above definition of an interface it is possible to define interfacial analogues of bulk thermodynamic quantities. Formally, this may be achieved in several equivalent ways. Below, we follow the method of Cahn [9]. An alternative derivation was formulated by Gibbs more than a century ago [1].

1.2.1 The interface free energy : Cahn's method

Consider a system consisting of two bulk phases, $\mathcal{X}$ and $\mathcal{Y}$, each containing $\mathcal{C}$ components, which are in contact along a flat interface. The interface is growing in equilibrium within a container in contact with suitable reservoirs. The entire system, including the reservoirs, is maintained at constant temperature, $\mathcal{T}$, hydrostatic pressure, $\mathcal{P}$, and chemical potential, μ_i, for each of the components. The increase in internal energy, $d\mathcal{E}$, due to the accretion of $d\mathcal{N}_i$ particles of component leading to corresponding changes in the entropy $\mathcal{S}$, volume $\mathcal{V}$ and area $\mathcal{A}$ is given by,

$$d\mathcal{E} \;=\; \mathcal{T}d\mathcal{S} - \mathcal{P}d\mathcal{V} + \sum_{i=1}^{\mathcal{C}} \mu_i d\mathcal{N}_i + \sigma_f d\mathcal{A} \tag{1.1}$$

Eqn. 1.1 contains the usual bulk term plus the added term $\sigma_f d\mathcal{A}$ which is required to account for the increase in internal energy of the system which is associated with the increase in the area

of the interface. From Eqn. 1.1, we have

$$\sigma_f = [\frac{\partial \mathcal{E}}{\partial \mathcal{A}}]_{\mathcal{S},\mathcal{V},\mathcal{N}_i}, \tag{1.2}$$

and σ_f, the interfacial free energy per unit area, is therefore defined as the increase in internal energy of the entire system per unit increase in interface area at constant $\mathcal{S}$ and $\mathcal{V}$ and $\mathcal{N}_i$ are held constant. We may as well define σ_f in terms of the Gibbs free energy, $\mathcal{G}$, the Helmholtz free energy, $\mathcal{F}$, and the grand potential, Ω, as

$$\sigma_f = \left[\frac{\partial \mathcal{G}}{\partial \mathcal{A}}\right]_{\mathcal{T},\mathcal{P},\mathcal{N}_\rangle} = \left[\frac{\partial \mathcal{F}}{\partial \mathcal{A}}\right]_{\mathcal{T},\mathcal{V},\mathcal{N}_i} = \left[\frac{\partial \Omega}{\partial \mathcal{A}}\right]_{\mathcal{T},\mathcal{V},\mu_i}. \tag{1.3}$$

Further, on integrating Eqn 1.1, we obtain finally

$$\sigma_f = \frac{1}{\mathcal{A}}\left[\mathcal{G} - \mu_i \mathcal{N}_i\right]. \tag{1.4}$$

where $\mathcal{G} = \mathcal{E} + \mathcal{P}\mathcal{V} - \mathcal{T}\mathcal{S}$ Since the quantity $\sum_{i=1}^{C} \mu_i \mathcal{N}_i$ is the total Gibbs free energy which the homogeneous $\mathcal{X}$ and $\mathcal{Y}$ phases would possess together, we may identify σ_f simply as the excess Gibbs free energy of the entire system per unit interface area due to the presence of the interface. Note that the entire contribution to σ_f arises from the excess Gibbs free energy of the interfacial region. There is no contribution from the bulk. This ensures that σ_f is independent of our choice for the width of the interface as long as it is large enough to contain the full variation of all intensive interfacial quantities e.g., the region between the dashed lines in Fig. 1.1.

1.3 Equilibrium fluctuations of interfaces

Interfaces in equilibrium rarely remain flat. As can be easily seen, translating a planar interface between two coexisting phases in equilibrium in a direction perpendicular to the interface costs no energy. It therefore follows that long wavelength fluctuations of the interface would be energetically cheap and would therefore dominate and roughen the regions between two materials. How strong these effects are depends on dimensionality (i.e., if the interface is a line or a plane) and on temperature. For instance, for fluid interfaces, two-dimensional systems with one-dimensional interfaces have a mean-square roughness of the interface that varies linearly with system size; the corresponding quantity in three-dimensional systems is logarithmic with the system size. To understand the role of fluctuations in interfaces, we consider first the simplest case where the fluctuations are thermal in origin. For fluid interfaces, in the limit of zero viscosity, these fluctuations are known as capillary waves.

1.3.1 Thermal fluctuations

Consider the fluctuation [2, 10] of a two-dimensional surface defined in the Monge representation as $z = h(x, y)$. The area of the flat surface is denoted by A. For slowly varying fluctuations of this surface about a flat shape ($h = h_0$, where h_0 is a constant) the additional surface free energy of the undulated interface over that of the flat one ($\Delta \mathcal{F}_s = \mathcal{F}_s - \gamma \mathcal{A}$) is approximately

$$\Delta \mathcal{F}_s = \frac{1}{2} \gamma \int dx dy ((\frac{\partial h}{\partial x})^2 + (\frac{\partial h}{\partial y})^2) \tag{1.5}$$

Note that the free energy $\Delta \mathcal{F}_s$ is independent of h itself and depends only on the derivatives, due to translational invariance. In Fourier space,

$$\Delta \mathcal{F}_s = \frac{1}{2} \gamma \sum_{\mathbf{q}} q^2 |h(\mathbf{q})|^2 \tag{1.6}$$

The mean-square value of the fluctuating variable $h(\mathbf{q})$, using equipartition, can be written as

$$< |h(\mathbf{q})|^2 > = \frac{\mathcal{T}}{\gamma q^2} \tag{1.7}$$

This gives the mean-square value of each Fourier mode in thermal equilibrium.

The mean-squared, real-space fluctuations of the surface about a flat profile, are given by

$$< h^2(\mathbf{r}) > = \frac{1}{A} \sum_{\mathbf{q}} < |h(\mathbf{q})|^2 > = \frac{1}{(2\pi)^2} \int d\mathbf{q} < |h(\mathbf{q})|^2 > \tag{1.8}$$

To avoid logarithmic divergences (when $\mathbf{q}$ is two-dimensional) while performing the integral, we introduce a lower limit to the integral, π/L, related to the finite size of the system ($L \propto \sqrt{A}$) and an upper limit, π/a due to the finite molecular size (proportional to a, the intermolecular separation). Then we have [2],

$$< h^2(\mathbf{r}) > = \frac{1}{2\pi\gamma} log \frac{L}{a} \tag{1.9}$$

By symmetry, $< h^2(\mathbf{r}) >$ is independent of the point $\mathbf{r}$ in the $x - y$ plane at which the fluctuation is calculated. Note that the mean-square fluctuation diverges as the logarithm of the system size. For a one-dimensional interface (i.e., a line instead of a surface) this divergence is even more severe and increases linearly with the size of the system. Thus, due to reduced dimensionality of these interfaces, the thermal fluctuations can have drastic effects on the "flatness" of the interfaces.

1.3.2 Capillary waves

For fluid interfaces, in the limit of negligible viscosity, the dominant fluctuations are capillary waves. We first write down the potential energy of an incompressible fluid surface acting under

gravity and surface tension. The free energy, $\mathcal{F}_s$, is given by a constant term that comes from the bulk (where density variations are not allowed) free energy, $\mathcal{F}_0$, and a contribution from the surface tension and gravitational terms :

$$\mathcal{F}_s = \mathcal{F}_l + \frac{1}{2} \int dA [\rho_0 g h^2 + \gamma |\nabla h|^2] \tag{1.10}$$

where A is the area, ρ_0 is the density, and γ is the surface tension. Solving the equation of motion for the interfacial position $h(x, y)$ resulting from the above free energy in the undamped, zero viscosity, inertial limit, we can obtain the dispersion relation [2]

$$\omega = \sqrt{q \left(g + \frac{\gamma q^2}{\rho_0} \right)} \tag{1.11}$$

which shows that the frequency of such capillary fluctuations, $\omega \to 0$, as $q \to 0$. For a liquid solid interface, these capillary fluctuations are known as "crystallization waves" [11]. For most ordinary solids, such waves are highly damped, however, though they have been experimentally studied in great detail for liq helium at temperatures 0.03 to 0.5 K [12, 13]

1.4 Morphology and dynamics of growth of interfaces

In most situations, interfaces are actually not in equilibrium and it is difficult to define equilibrium structural and thermodynamic quantities. In such cases however, certain scaling laws, which determine how non-equilibrium interfacial fluctuations behave with time and system size come in useful in characterizing the structure of an interface. The scaling exponents behave similar to the exponents well known from studies of equilibrium critical point phenomena such that they can be used to define distinct "universality classes" of non-equilibrium, driven interfaces. In this section, we discuss briefly two such universality classes, viz. the Edwards-Wilkinson and the Kardar-Parisi-Zhang.

1.4.1 Scaling concepts

Consider a one-dimensional interface between two phases in two dimensions. Let us consider a situation where one of the phases is growing at the expense of the other. To describe the growth of this one-dimensional interface quantitatively, we introduce two functions [10].

- The *mean height* of the surface, $\overline{h}$, is defined by

$$\overline{h}(t) \equiv \frac{1}{L} \int_0^L dx\, h(x, t) \tag{1.12}$$

where $h(x,t)$ is the position of the interface at x at time t. The mean height increases linearly with time,

$$\overline{h}(t) \sim t \tag{1.13}$$

if the interface moves at a constant rate.

- The *interface width*, which characterizes the *roughness* of the interface, is defined by the rms fluctuation in the height,

$$w(L,t) \equiv \sqrt{\frac{1}{L} \int_0^L [h(x,t) - \overline{h}(t)]^2} \tag{1.14}$$

The time evolution of the surface width has two regions separated by a "crossover" time t_x [10]

(i) Initially, the width increases as a power of time,

$$w(L,t) \sim t^\beta \qquad\qquad [t << t_x] \tag{1.15}$$

The exponent β, which we call the *growth exponent*, characterizes the time-dependent dynamics of the roughening process.

(ii) This is followed by a saturation regime during which the width reaches a *saturation value*, w_{sat}. As L increases, the saturation width, w_{sat}, increases as a power law,

$$w_{sat}(L) \sim L^\alpha \qquad\qquad [t >> t_x] \tag{1.16}$$

The exponent α, called the *roughness exponent*, characterizes the roughness of the saturated interface.

(iii) The crossover time t_x (or *saturation* time) at which the interface crosses over from the behavior of (i) to that of (ii) depends on the system size,

$$t_x \sim L^z \tag{1.17}$$

where z is called the *dynamic exponent*.

The exponents α, β and z are not independent. If we approach the crossover point $(t_x, w(t_x))$ from the left, we find, according to Eqn. 1.15, that $w(t_x) \sim t_x^\beta$. However, approaching the same point from the right, we have from Eqn. 1.16, $w(t_x) \sim L^\alpha$. From these two relations follows $t_x^\beta \sim L^\alpha$ which according to Eqn. 1.17, implies that

$$z = \frac{\alpha}{\beta} \tag{1.18}$$

Eqn 1.18, a scaling law linking the three exponents, is valid for any growth process that obeys the *Family-Vicsek* scaling relation [10]

$$w(L,t) \sim L^\alpha f\left(\frac{t}{L^z}\right) \tag{1.19}$$

1.4.2 The Edwards-Wilkinson equation

Consider an interface, defined by a height function $h(\mathbf{x}, t)$ which obeys the following stochastic growth equation,

$$\frac{\partial h(\mathbf{x}, t)}{\partial t} = G(h, \mathbf{x}, t) + \eta(\mathbf{x}, t) \tag{1.20}$$

where $\eta(\mathbf{x}, t)$ is a random noise and $G(h, \mathbf{x}, t)$ contains the deterministic part. Consider also that the equation of motion Eqn. 1.20 obeys the following symmetries [10]:

(i) *Invariance under translation in time.* The growth equation is invariant under the transformation $t \to t + \delta_t$. This symmetry rules out an explicit time dependence of G.

(ii) *Translation invariance along the growth direction.* The growth rule is independent of where we define $h = 0$, so the growth equation should be invariant under the translation $h \to h + \delta_h$. This symmetry rules out the explicit h dependence of G, so that the equation must be constructed from combinations of $\nabla h, \nabla^2 h, ..., \nabla^n h$, etc.

(iii) *Translation invariance in the direction perpendicular to the growth direction.* The equation is independent of the actual value of $\mathbf{x}$, having the symmetry $\mathbf{x} \to \mathbf{x} + \delta_x$. This exclude explicit $\mathbf{x}$ dependence of G.

(iv) *Rotation and inversion symmetry about the growth direction* $\mathbf{n}$. This rules out odd order derivatives in the coordinates, excluding vectors such as $\nabla h, \nabla(\nabla^2 h)$, etc.

(v) *Up/down symmetry for h.* The interface fluctuations are similar with respect to the mean interface height. This rules out even powers of h, terms such as $(\nabla h)^2, (\nabla h)^4$, etc. A moments reflection tells us that this symmetry implies that $h(\mathbf{x}, t)$ represents in this case an interface between two equilibrium coexisting phases.

The final form of the growth equation, consistent with all the symmetries listed above is,

$$\frac{\partial h(\mathbf{x}, t)}{\partial t} = (\nabla^2 h) + (\nabla^4 h) + ... + (\nabla^{2n} h) + (\nabla^2 h)(\nabla h)^2 + ...$$
$$+ (\nabla^{2k} h)(\nabla h)^{2j} + \eta(\mathbf{x}, t), \tag{1.21}$$

where n, k, j can take any positive integer value. For simplicity of notation we do not explicitly indicate the coefficients in front of the terms.

Since we are interested in the scaling properties, we focus on the long-time $(t \to \infty)$, long-distance $(x \to \infty)$ behavior of functions that characterize the surface. In this *hydrodynamic limit*, higher order derivatives should be less important compared to the lowest order derivatives, as can be confirmed using scaling arguments.

The noise term, $\eta(\mathbf{x}, t)$ in Eqn. 1.21 incorporates the stochastic character of the fluctuation process and is assumed to be uncorrelated, with the properties

$$\langle \eta(\mathbf{x}, t) \rangle = 0 \tag{1.22}$$

$$< \eta(\mathbf{x}, t) \eta(\mathbf{x}', t') > = 2D\delta^d(\mathbf{x} - \mathbf{x}')\delta(t - t') \tag{1.23}$$

Thus, the simplest equation describing the fluctuations of an equilibrium interface, called the Edwards-Wilkinson (EW) equation [14] has the form

$$\frac{\partial h(\mathbf{x}, t)}{\partial t} = \nu \nabla^2 h + \eta(\mathbf{x}, t) \tag{1.24}$$

Here ν is sometimes called a "surface tension", for the $\nu \nabla^2 h$ term tends to smoothen the interface. Eqn 1.24 is valid in the small gradient approximation, i.e., in the limit $(\nabla h) << 1$.

The average velocity of the interface is zero, which can be seen by using Eqn 1.24,

$$v \equiv \int_0^L d^d\mathbf{x} \left\langle \frac{\partial h}{\partial t} \right\rangle = 0. \tag{1.25}$$

The contribution from the Laplacian term is zero, due to the periodic boundary conditions, and since the noise has zero average according to Eqn 1.22.

The scaling exponents of the EW equation can be obtained either by using scaling arguments or by solving the equation. The exponents in d-dimensions are given as follows :

$$\alpha = \frac{2-d}{2}, \quad \beta = \frac{2-d}{4}, \quad z = 2 \tag{1.26}$$

Thus for $d = 2$, we find that $\alpha = \beta = 0$, i.e., the width scales logarithmically with time at early times, and the saturation width depends on the logarithm of the system size. For $d > 2$, the roughness exponent α becomes negative, which means that the interface is flat, because the surface tension suppresses any noise-induced irregularity.

1.4.3 Non-equilibrium interface : Kardar-Parisi-Zhang equation

The first extension of the EW equation to include non-linear terms was proposed by Kardar, Parisi and Zhang (KPZ) [10, 15]. The KPZ equation is the simplest growth equation which has the symmetries (i)-(iv) of the linear theory discussed in Eqn. 1.21, but the up-down symmetry of the interface height $h(\mathbf{x}, t)$ is broken. The source of the symmetry breaking is, of course, the existence of a driving force, F, perpendicular to the interface, and uniform in space and time which selects a particular growth direction for the interface. In the linear theory this up-down symmetry excludes terms such as $(\nabla h)^{2n}$ from the growth equation. The lowest order term of this sort is $(\nabla h)^2$ which, if added to the EW Eqn. 1.26, results in the KPZ equation given as

$$\frac{\partial h(\mathbf{x}, t)}{\partial t} = \nu \nabla^2 h + \frac{\lambda}{2} (\nabla h)^2 + \eta(\mathbf{x}, t) \tag{1.27}$$

In general, the existence of a driving force is a *necessary*, but not *sufficient* condition for the broken up-down symmetry in h, and hence for the appearance of the nonlinear term. As an example, consider the random deposition (RD) model with surface relaxation [16]. In the RD

model, each particle falls along a single column toward the surface until it reaches the top of the interface, whereupon it sticks irreversibly. To include surface relaxation, the deposited particle is allowed to diffuse along the surface up to a finite distance, stopping when it finds the position with the *lowest* height. In this model, particle deposition generates a driving force that makes the interface grow. Deposition apparently breaks the up-down symmetry of the growth, but the model is nevertheless described by the EW equation, so in fact no symmetry breaking occurs. If we transform to a system of coordinates moving together with the interface, the model generates an interface which is invariant under the transformation $h \rightarrow -h$.

Scaling exponents for the KPZ equation can be obtained exactly for $d = 1$ via a dynamical renormalization group calculation, to be $\alpha = 1/2$, $\beta = 1/3$ and $z = 3/2$. However for $d > 1$, dynamic RG analysis does not give the scaling exponents. There are several models that predict the scaling exponents in higher dimensions but none of them are exact. For $d = 2$, large scale simulations predict that $\beta = \alpha/z = 0.240 \pm 0.0001$ (see [10] and references therein). There is however a scaling relation that is true in any dimensions :

$$\alpha + z = 2 \qquad (1.28)$$

1.5 Plan of the thesis

In the previous sections we have tried to define and describe equilibrium and driven interfaces in general terms as briefly as possible. There are extensive review articles [13] and books [1, 2, 10] on this subject and the reader is referred to them for details. In this thesis, we study a special class of interfaces which are produced by non-uniform fields which vary sharply in the direction perpendicular to the interface. The primary function of this field is to break the translational symmetry along the growth direction. Breaking this symmetry implies a non zero energy cost for long wavelength fluctuations of the interface which primarily tends to stabilize the sort of planar interfaces discussed in Section 1.3. Surprisingly, however, we discover, in each case, the existence of residual fluctuations which produce novel phenomena.

In Chapter 2, we specialize our discussion of interfaces to interfaces in the Ising model. We introduce the model and discuss the equilibrium phases. The importance of Ising model in the sense that a variety of other statistical mechanical systems can be described by it, is then pointed out. In particular, reference is made to the mapping to lattice gas and binary alloy. Next we review existing literature on interfaces in the ferromagnetic Ising model. A study of the physics of single surfaces or interfaces begins with the characterization of the shape of the interface. In this regard, we study the structure of the Ising interface. We derive the interfacial profile using the continuum ϕ^4 theory. We discuss the stability of a flat interface in the two-dimensional Ising model. The role of fluctuations is pointed out in detail. The time-dependent properties of

an inclined interface separating up and down spin regions in a two-dimensional nearest-neighbor Ising model evolving under Glauber dynamics in a non-zero but uniform field is discussed. We show that the for a constant magnetic field, the equation of motion for the interface reduces to the KPZ equation as expected. In the limit of large exchange coupling, the model reduces to the single-step model for ballistic growth and thence to the asymmetric exclusion process which describes a driven diffusive system of hard core particles on an one- dimensional lattice. The drift velocity of the interface is found as a function of field, temperature and inclination, and interface correlation functions are related to sliding tag correlation functions in the particle system. The non-linear dependence of the current on density leads to kinematic waves which involves moving density fluctuations.

In Chapter 3, we study the steady state structure and dynamics of a two-dimensional Ising interface placed in an *inhomogeneous* external field translated with velocity v_e. The non-uniform field has a profile with a fixed shape which is designed to stabilize a flat interface. For small velocities the interface is stuck to the profile and is rippled with a periodicity which may be either commensurate or incommensurate with the lattice parameter of the square lattice. For a general orientation of the profile, the local slope of the interface locks in to one of infinitely many rational directions producing a "devil's staircase" structure. These "lock-in" or commensurate structures disappear as v_e increases through a kinetics driven commensurate - incommensurate transition. For large v_e the interface becomes detached from the field profile and coarsens with KPZ exponents. The complete phase -diagram and the multifractal spectrum corresponding to these structures are obtained numerically together with several analytic results concerning the dynamics of the rippled phases. The fact that interfacial fluctuations are partially suppressed by the external field is manifested in the exact agreement between a mean field theory and simulation results. However small interfacial fluctuations produce a dynamical phase diagram showing infinitely many dynamical phases and dynamic phase transitions.

Next we turn our attention to more realistic systems viz., solid - liquid interfaces. In Chapter 4, we introduce and describe atomic systems and discuss the need to study such systems. Before we go on to study interfaces in atomic systems we use this chapter to introduce the models and computational techniques (e.g. Monte Carlo and molecular dynamics simulations) that are used in this thesis. The relevance of these simulation techniques in the context of the thesis is pointed out. Specific techniques to simulate hard systems are also described. Bulk thermodynamic, structural and dynamic quantities that characterize different phases are described in some detail. We reproduce existing data in order to validate our computational methods to be used for subsequent calculations.

In Chapter 5, we show how one can create a solid - liquid interface using a non - uniform external field. This is a direct analog of the Ising interface studied in Chapter 3. In contrast to the Ising interface, elastic deformations of the solid are allowed and play a prominent part in

determining the properties of the interface. In fact, we show that a thin strip of solid placed within a bath of its own liquid relieves stress by novel interfacial fluctuations which involve addition or deletion of entire lattice layers of the crystal. Local analogues of the bulk quantities defined in Chapter 4 are calculated along the length of the system in the direction perpendicular to the interface. The "layering" transition is shown to be a generic feature of systems interacting via any interatomic potential.

In Chapter 6, we show how these interfacial fluctuations influence mass, momentum and energy transport properties across the interface. Tiny momentum impulses are seen to produce shock waves which travel through the liquid solid interface and causes the spallation of crystal layers into the liquid. We show how kinetic and energetic constraints prevents the spallation of partial layers from the crystal, making this process suitable for creating nano-layer and coatings or for making nano-wires. We also study heat transport through the liquid solid interface and obtain the contact or Kapitza resistance of the interface as a function of the depth of the potential well.

2 Interfaces in the Ising model

After an introduction to the structure and properties of interfaces in general, in this chapter we specialize our discussion to a study of interfaces in the particularly simple context of the Ising model. The Ising model [17] tries to imitate behaviour in which individual elements (e.g., atoms, animals, protein folds, biological membrane, social behavior, etc.) modify their behavior so as to conform to the behavior of other individuals in their vicinity. The Ising model has more recently been used to model phase separation in binary alloys [17] and spin glasses [18]. In biology, it can model neural networks [19], flocking birds [20], or beating heart cells [21]. It can also be applied in sociology [22].

In this chapter we start by giving an introduction of the Ising model and its importance in explaining several phenomena. We discuss briefly the mapping of the Ising model to binary alloy and lattice gas models. We then discuss the structure and stability of the Ising interface in the low temperature limit when the interface may be described by a single valued "height" function $h(x,t)$. Finally we discuss in detail the effect of a homogeneous external field on the Ising interface with special emphasis on the nature of fluctuations of the interface about the mean position $\overline{h}(t)$ of the interface.

2.1 Ising model

The Ising model was proposed in the doctoral thesis of Ernst Ising, a student of W. Lenz. Ising [23] tried to explain certain empirically observed facts about ferromagnetic materials using a model proposed by Lenz [24]. It was referred to in Heisenberg's [25] paper which used the exchange mechanism to describe ferromagnetism. The name became well-established with the publication of a paper by Peierls [26], which gave a non-rigorous proof that spontaneous magnetization must exist. A breakthrough occurred when it was shown that a matrix formulation of the model allows the partition function to be related to the largest eigenvalue of the matrix (Kramers and Wannier [27], Montroll [28, 29], Kubo [30]. Kramers and Wannier calculated the Curie temperature using a two-dimensional Ising model, and a complete analytic solution was subsequently given by Onsager [31].

Consider a lattice in d dimensions of sites i labelled $1, 2, ...\mathcal{N}(\Omega)$, which we will take to be hypercubic, unless otherwise stated. The degrees of freedom are classical spin variables, S_i,

residing on the vertices of the lattice, which take only two values : up or down, or more usefully,

$$S_i = \pm 1 \tag{2.1}$$

The total number of states of the system is $2^{\mathcal{N}(\Omega)}$. The spins interact with an external field (in principle varying from site-to-site) H_i and with each other through exchange interactions $J_{ij}, K_{ijk}, ..$ which couple two spins, three spins, ... etc.

A general form of the Hamiltonian is

$$-\mathcal{H}_\Omega = \sum_{i \in \Omega} H_i S_i + \sum_{ij} J_{ij} S_i S_j + \sum_{ijk} K_{ijk} S_i S_j S_k + ... \tag{2.2}$$

The free energy is given by

$$\mathcal{F}_\Omega(\mathcal{T}, H_i, J_{ij}...) = -k_B \mathcal{T} \log Tr e^{-\beta \mathcal{H}_\Omega} \tag{2.3}$$

where the trace operation is a sum over all possible configurations of the spin S_i, and thermodynamic properties can be obtained by differentiating the free energy.

To discuss the phase transition of the Ising model, we consider the simple case of the nearest neighbour Hamiltonian

$$-\mathcal{H}_\Omega = H \sum_{i=1}^{\mathcal{N}(\Omega)} S_i + J \sum_{<ij>} S_i S_j \tag{2.4}$$

where we have assumed that the external magnetic field H is uniform in space, and that the only interaction between spins is that between *neighbouring* spins, with strength denoted by J. We consider the case $J > 0$. With a uniform external magnetic field, we can define the magnetization or magnetic moment per site, M :

$$M \equiv \frac{1}{\mathcal{N}(\Omega)} \sum_{i=1}^{\mathcal{N}(\Omega)} \langle S_i \rangle. \tag{2.5}$$

Now consider the case when $H = 0$. The spins then seek configurations that at constant $\mathcal{T}$, will minimize the Helmholtz free energy $\mathcal{F}_\Omega = \mathcal{E} - \mathcal{T}\mathcal{S}$. At high $\mathcal{T}$, $\mathcal{F}_\Omega$ is clearly minimized by maximizing the entropy, S. The maximally disordered state has the highest entropy, implying that the equilibrium state at high temperatures is the *paramagnetic* state with no average alignment of spins, i.e., no magnetization. At low temperatures, the internal energy dominates over $\mathcal{T}\mathcal{S}$, and the state that minimizes $\mathcal{F}_\Omega$ is one that minimizes $\mathcal{E}$. States which minimize $\mathcal{E}$ have a non-vanishing magnetization, and the low temperature equilibrium phase is the $ferromagnetic$ phase with nonzero magnetization M. At some temperature $\mathcal{T}_c$, there is a phase transition from the entropy dominated paramagnetic state to the energy dominated ferromagnetic state.

The magnetization M is called the *order parameter* of the ferromagnetic phase and takes two degenerate values $\pm M(\mathcal{T}) \to \pm 1$ as $\mathcal{T} \to 0$. The two degenerate states correspond to cases where the spins are either all up ($S_i = +1$) or all down ($S_i = -1$). At $\mathcal{T} = 0$, all spins are perfectly aligned to either of the two possible values. At any nonzero temperature, domains of one phase in the other are stabilized due to entropy. These domains cost positive interfacial energy and grow in response to external fields.

2.1.1 Mapping to other models

The usefulness of the Ising model stems to large extent, from its generality. The Ising model maps onto a large number of simple statistical models for complex phenomena in material science as well as biology, economics and sociology. We show below three common mappings which are included as illustrative examples [17].

A. Ising antiferromagnetic model : If we replace J in Eqn. 2.4 by $-J$ ($J > 0$) then energy is lowered for neighbouring spins with different signs. At low temperatures neighbouring spins are antiparallel. This becomes the antiferromagnetic model. In bipartite lattices where the lattice naturally breaks up into two interpenetrating sub lattices (e.g., square lattice in two dimensions and the body centered cubic lattice in three), the Ising antiferromagnet is mathematically identical to the ferromagnetic case. Indeed for, $H = 0$, if we write every alternate S_i as $-S_i$, then $\mathcal{H}_\Omega$ is the same as before because the extra minus sign cancels that from $-J$. In other words, if $H = 0$, the sign of J does not affect the thermodynamic potential. The order parameter for the Ising antiferromagnet is the "staggered" magnetization, M_s, which is the difference of the individual magnetizations of the two sub lattices. The analogue of the external field, H, is the "staggered field", H_s, which has opposite signs for each sublattice.

B. Model of binary alloy : Let $S_i = 1$ represent an atom of type A at point i and $S_i = -1$ represent an atom of type B at point i. Let $\epsilon_{AA}, \epsilon_{BB}, \epsilon_{AB}$ be the interaction energies between neighbouring atoms. A binary substitutional alloy which has either A or B types of atoms at each site may be described by the Ising model [32]. The energy of a pair of neighbouring atoms i, j can be written as

$$
\begin{aligned}
\epsilon_{ij} &= -JS_iS_j - \frac{1}{\zeta}H(S_i + S_j) + \mathcal{K} \\
\mathcal{H}_\Omega &= \frac{1}{2}\sum_{i,j}\epsilon_{ij}
\end{aligned}
\tag{2.6}
$$

where ζ is the number of nearest neighbours for each spin.

Comparing the energies of a two atom cluster containing either AA, BB or AB types and solving for J, H and $\mathcal{K}$ we get :

$$
\begin{aligned}
J &= \frac{1}{2}\epsilon_{AB} - \frac{1}{4}(\epsilon_{AA} + \epsilon_{BB}) \\
\mathcal{K} &= \frac{1}{2}\epsilon_{AB} + \frac{1}{4}(\epsilon_{AA} + \epsilon_{BB}) \\
H &= \frac{\zeta}{4}(\epsilon_{BB} - \epsilon_{AA})
\end{aligned}
\tag{2.7}
$$

Using Eqn. 2.7, Eqn. 2.4 now describes the binary alloy. If $(\epsilon_{AA} + \epsilon_{BB})/2 < \epsilon_{AB}(J > 0)$, at sufficiently low temperatures the atoms A will gather together while atoms B will form another clsuter. Hence we have a model for a *de-mixing* transition. If $J < 0$ and the temperature is low, the atoms A and B will arrange alternately, leading to a *order-disorder* transition. The paramagnetic phase at high temperature of course, represents a randomly substituted alloy - the mixed phase.

C. Lattice gas model : Let $S_i = 1$ represent a molecule at site i, and $S_i = -1$ represent no molecule at site i. We assume that the same site cannot accommodate two or more molecules. Let the interaction energy of neighbouring molecules be $-\epsilon$. Then we may write the energy between two neighbouring lattice sites as

$$
\begin{aligned}
-J - \frac{2H}{\zeta} + \mathcal{K} &= -\epsilon \ , \quad S_i = S_j = 1 \\
-J + \frac{2H}{\zeta} + \mathcal{K} &= 0 \quad , \quad S_i = S_j = 1 \\
J + \mathcal{K} &= 0 \quad , \quad S_i = 1, \ S_j = -1
\end{aligned}
\tag{2.8}
$$

Solving these, we get

$$
\begin{aligned}
J &= \frac{1}{4}\epsilon \\
H &= \frac{\zeta}{4}\epsilon
\end{aligned}
\tag{2.9}
$$

Therefore, Eqn. 2.4 is also a model of gas molecules, where $-\epsilon$ represents the attraction between the gas molecules. The restriction of at most one molecule per site represents short-range repulsion. The high density state, i.e. $\langle S_i \rangle > 0$ corresponds to the liquid phase while the low density state, i.e. $\langle S_i \rangle > 0$ corresponds to the gas phase. Although this model may seem rather contrived since there is no underlying lattice in a real liquid-gas transition, surprisingly, the critical properties of this model turn out to be identical to real experimental gases due to universality [33, 34].

2.1.2 Structure of interfaces in the Ising model

As mentioned above, at any non-zero temperature the Ising model contains domains populated by either one of the two ground states. At low enough temperatures, these domains are separated by well defined interfaces which fluctuate and move as one phase grows at the expense of the other. In this section, we shall study Ising interfaces for zero external field, where the two phases on either side of the interface are degenerate in energy. We shall also implicitly assume here and elsewhere in this thesis that the temperature is low enough compared to the coupling parameter J so that the interface can be represented either as a flat boundary or at least as a single valued curve which does not loop back on itself (i.e., contains no overhangs). To find the structure and behavior of the Ising interface we start with the Ginzburg-Landau free energy expansion

$$\mathcal{F} = \int d\mathbf{r} [-\frac{\Psi}{2}\phi(\mathbf{r})^2 + \frac{c}{4}\phi(\mathbf{r})^4 + \frac{B}{2}|\nabla\phi(\mathbf{r})|^2] \tag{2.10}$$

where the coefficients Ψ, c and B are related to the microscopic parameters and ϕ is the space dependent coarse grained magnetisation. In particular Ψ vanishes at the critical point given by $\mathcal{T}_c$. The function $\phi(\mathbf{r})$ which minimizes $\mathcal{F}$ is determined by the equation :

$$\frac{\delta\mathcal{F}}{\delta\phi(\mathbf{r})} = \frac{\partial f}{\partial\phi} - \frac{\partial}{\partial r_i}\frac{\partial f}{\partial\phi_{r_i}} = 0 \tag{2.11}$$

where $\phi_{r_i} = \partial\phi/\partial r_i$. The repeated index i and $\mathbf{r}_i = (x, y, z)$ are summed over in Eqn. 2.11. The resulting equation is

$$-\Psi\phi + c\phi^3 - B\nabla^2\phi = 0 \tag{2.12}$$

with the boundary conditions that the system is uniform away from the interface. Far away from the interface, we expect the two phases to have their equilibrium values of the composition. Assuming that ϕ is small we get,

$$\phi_0 = \pm\sqrt{\frac{\Psi}{c}} \tag{2.13}$$

Consider now a one-dimensional concentration variation, $\phi(z)$, with boundary conditions $d\phi/dz = 0$ at $z = \pm\infty$, which ensure the equilibrium phases at these limits and represents a flat interface. The solution is then

$$\phi(z) = \sqrt{\frac{\Psi}{c}}\tanh\frac{z}{\xi} \tag{2.14}$$

where the width of the interfacial region is given by $\xi = \sqrt{2B/\Psi}$, which is the bulk correlation length and diverges as $\Psi \to 0$ or $\mathcal{T} \to \mathcal{T}_c$. Thus, for $z \to \pm\infty$, ϕ approaches its equilibrium, uniform values of $\pm\sqrt{\Psi/c}$ as shown in the Fig. 2.1. The width of the interfacial region is proportional to $1/\sqrt{\Psi}$, so that as the critical point is approached ($\Psi \to 0$) the interfacial width diverges.
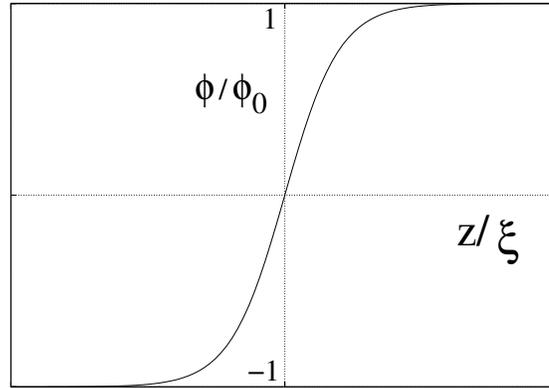
FIGURE 2.1: A plot of the interfacial profile
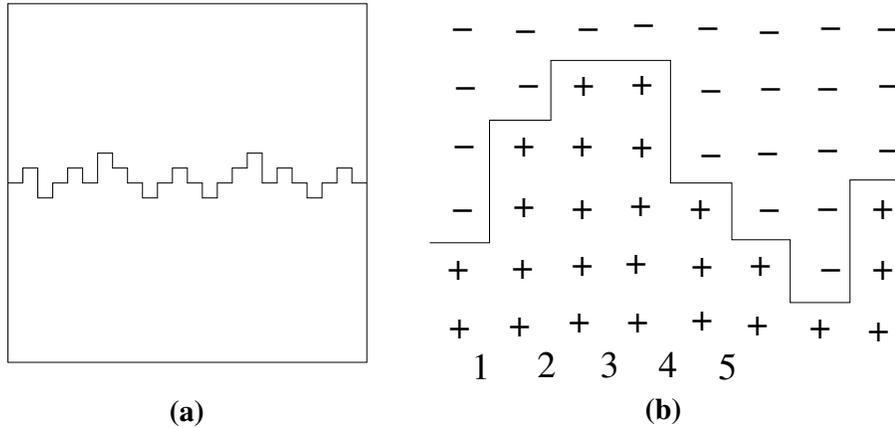
FIGURE 2.2: (a) Boundary line for a square lattice. (b) An enlargement of a portion of (a).

2.1.3 Stability of the Ising interface

To discuss the stability of the flat Ising interface described above, let us consider a square lattice of Ising spins with a boundary line (interface) separating up and down spin regions as shown in the Fig. 2.2. The energy of the interface is its total length times $2J$. The total length is

$$L = L_0 + \sum_{k=1}^{L_0} |y_k|$$

(2.15)

Here, y_k is the length of the $k - th$ boundary counting from the left. In Fig. 2.2 $y_1 = 2, y_2 = 1, y_3 = 0, y_4 = -2, y_5 = -1, \dots$ etc. Therefore the thermodynamic potential $\mathcal{F}$ of the full

interface in the limit of large L_0, is

$$
\begin{aligned}
\mathcal{F} &= -k_B \mathcal{T} \ln \mathcal{Z} \\
\mathcal{Z} &= \sum_{y_1=-\infty}^{\infty} \sum_{y_2=-\infty}^{\infty} \ldots \sum_{y_{L_0}=-\infty}^{\infty} e^{-2JL/k_B \mathcal{T}}
\end{aligned}
\tag{2.16}
$$

Now, in the k-th horizontal position, the height of the boundary is

$$
h_k = \sum_{j=1}^{k} y_j
\tag{2.17}
$$

Hence, the difference in height between two points on the interface is

$$
\Delta h \equiv h_{k+n} - h_k = \sum_{j=k+1}^{k+n} y_j
\tag{2.18}
$$

If $n << L_0$, each y_j will be independent variables. Using the central limit theorem we get the distribution of Δh :

$$
\begin{aligned}
f(\Delta h) &\simeq \frac{1}{\sqrt{2\pi}\sigma} e^{-(\Delta h)^2/2\sigma^2} \\
w^2 &= n\langle y^2 \rangle \\
&= \frac{n}{2\sinh^2(J/k_B \mathcal{T})}
\end{aligned}
\tag{2.19}
$$

Hence the interface fluctuates violently in the same manner as a one dimensional random walker. The amplitude of fluctuation in the middle is about $\sqrt{L_0}/\sinh(J/k_B \mathcal{T})$. Although $\sqrt{L_0}$ is much smaller than L_0, it is still not a microscopic length scale. Therefore, this interface is a wiggly and rough curve, not smooth and flat. In this analysis we have not considered "overhangs" or isolated regions. However the conclusion that the interface is rough is valid even if we include these effects.

2.2 Driven Interfaces in the Ising model

When there is an external field, the interface in an Ising model moves in a way that increases the size of the domains which are aligned in the direction of the field. The general problem of such a driven interface even for a simple model system like the Ising model is quite complex. In this section we show how, by using simplifying assumptions one can study such a driven interface in the two-dimensional Ising system. This is a reproduction of earlier work on constant field driven interface by Majumdar and Barma [35–38]. In the limit that the field H and temperature $\mathcal{T}$ are both much smaller than the nearest neighbour exchange coupling J (assumed isotropic), one can
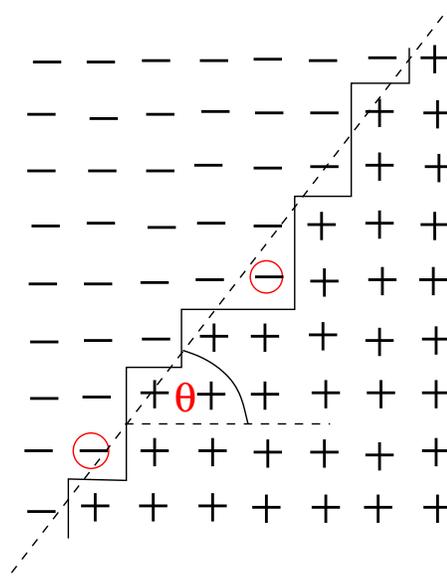
FIGURE 2.3: An Ising interface (bold line) between up and down Ising spins. Since J is very large, only spins at the corners, like the circled ones (coloured red) can flip. The orientation θ of the interface is also shown in the figure.

neglect overhangs so that the interface can as before be represented as a single valued function. The interface moves in steady state with a velocity v_f which depends on the external field H and on the orientation θ of the interface, measured with respect to the horizontal (Fig. 2.3). As the Ising spins obey single-spin flip Glauber dynamics, and $H, \mathcal{T} << J$ holds, the interface moves by "corner flips" where a vertical bond and a horizontal bond at a corner exchange places.

We shall show how such driven interfaces may be described using the KPZ equation. We will derive this dynamical equation first from the time dependent Ginzberg-Landau equation (TDGL) [33], and then once again after mapping the corner flip dynamics of the two-dimensional Ising model to the dynamics of a one-dimensional gas of hard core particles (the exclusion process) in the limit $H/J, \mathcal{T}/J \to 0$. We shall use the latter mapping to deduce some important dynamical properties of this interface.

2.2.1 Derivation of KPZ from TDGL

We consider, for the moment, that the inclination of the interface $\theta = 0$. The interface is given by the function $h(x,t)$. The coarse grained, space dependent magnetization ϕ is given by a function which is uniform everywhere except near the interface, $h(x,t)$ such that $\phi = \phi(y - h(x,t))$. The

function ϕ has a profile similar to Fig. 2.1. Model A dynamics [33] for ϕ then implies,

$$\frac{\partial \phi}{\partial t} = -\Gamma \frac{\delta \mathcal{H}_T}{\delta \phi} + \zeta(\mathbf{r}, t) \tag{2.20}$$

where

$$\mathcal{H}_T = \int d\mathbf{r}[a_1\phi^2 + a_2\phi^4 + a_3(\nabla\phi)^2 - H\phi] \tag{2.21}$$

is the coarse-grained Hamiltonian (which, for the moment, ignores the lattice) of an Ising system in a external field H and ζ is a Gaussian white noise with zero mean and

$$< \zeta(\mathbf{r}, t)\zeta(\mathbf{r}', t') > = 2k_BT\Gamma\delta(\mathbf{r} - \mathbf{r}')\delta(t - t') \tag{2.22}$$

Using $\mathcal{H}_T$ in Eqn. 2.20, taking $y - h(x,t) = \nu$ and converting all derivatives to derivatives over the profile $h(x,t)$, we have,

$$
\begin{aligned}
-\phi'(\nu)\frac{\partial h}{\partial t} = & - \Gamma[2a_1\phi(\nu) + 4a_2\phi^3(\nu) - 2a_3\phi''(\nu) + 2a_3\phi'(\nu)\frac{\partial^2 h}{\partial x^2} \\
& - 2a_3\phi''(\nu)(\frac{\partial h}{\partial t})^2 - H] + \zeta(\mathbf{r}, t)
\end{aligned}
\tag{2.23}
$$

where primes denotes derivatives with respect to ν. We then choose a ϕ dependent mobility Γ contributing to the lowest order in ϕ consistent with symmetry viz. $\Gamma = \Gamma_0 + \Gamma_1(\nabla\phi)^2$. Substituting for Γ and integrating both sides of the equation with respect to h between limits $(h - \chi/2)$ and $(h + \chi/2)$ i.e. over the interfacial region, we finally get an equation of motion for the interface.

$$\frac{\partial h}{\partial t} = \lambda_1\frac{\partial^2 h}{\partial x^2} - \lambda_2\left(\frac{\partial h}{\partial x}\right)^2 - \lambda_3 + \zeta(x, t) \tag{2.24}$$

where λ_1, λ_2 and λ_3 are parameters which involves the integral of $\phi(\nu), \phi'(\nu)$ and $\phi'(\nu)$ over the regions of the interface. Note that Eqn. 2.24 lacks Galilean invariance [39] $h' \to h + \epsilon x, \ x' \to x - \lambda_2\epsilon t, \ t' \to t$. Eqn. 2.25 is the familiar KPZ equation and therefore the interface grows with KPZ exponents $\alpha = 1/2, \beta = 1/3$.

2.2.2 Mapping to the Exclusion Process

In the exclusion process we consider a one-dimensional lattice of $\mathcal{N}_s$ sites, of which $\mathcal{N}_p = \rho\mathcal{N}_s$ are occupied by particles, and assume periodic boundary conditions [35, 37, 38]. In the simple exclusion process, a particle chosen at random attempts to hop with probability p to the right and probability q to the left, with $p + q = 1$. Because of the hard core constraint, the hop actually takes place if the sought site is vacant. $\mathcal{N}_p$ such attempted hops constitute a single time step.

In the steady state, every configuration of of the $\mathcal{N}_p$ particles is equally likely [40, 41]. Let us label the particles $n = 1, 2, ..., \mathcal{N}_p$ sequentially at $t = 0$. The ordering is preserved by

the dynamics of the exclusion process. The configuration of the system is specified by the set $\{h(n)\}$ where $h(n)$ denotes the location of the nth particle. The corresponding interface model, called the particle height (PH) model, is obtained by interpreting the tag label n as a horizontal coordinate, and $h(n)$ as a local height. Each configuration $\{h(n)\}$ then defines a one- dimensional interface in the form of a staircase inclined to the horizontal with mean slope $\tan\theta = 1/\rho$. The interface coordinates satisfy $h(n+1) \geq h(n)+1$, and the periodic boundary conditions translate into $h(n + \mathcal{N}_p) = h(n) \pm \mathcal{N}_s$. The evolution rule is as follows: in each time step, $h(n)$ tends to increase (or decrease) by 1 with probability p (or q); it actually increases (or decreases) if and only if $h(n + 1) - h(n) > 1$ (or $h(n) - h(n - 1) > 1$). In the unbiased case ($p = q = 1/2$), the interface does not move with a net velocity, but fluctuates around its initial position. But in the biased case ($p \neq q$), the interface moves vertically with the particle drift velocity v_p. The probabilities p and q can be related to the Ising model parameters on noting that ratio of the rates of up-down and down-up flips is $\exp(-2\beta H)$; thus $p = \exp(\beta H)/(2\cosh(\beta H))$ and the bias $\Delta = p - q = \tanh(\beta H)$.

$$v_p \equiv< (h(n,t) - h(n,0) >= (1 - \rho)(p - q) \tag{2.25}$$

where $h(n,t)$ is the location of the nth particle at time t.

2.2.3 Some Exact Results

It is straight-forward to derive [40, 41] the expression for v_p and the particle current j. The particle velocity,

$$v_p \equiv< (h(n,t) - h(n,0) >= (1 - \rho)(p - q) \tag{2.26}$$

which is the statement of the fact that in order for a particle to move one needs a bias *and* a hole to move into. Although we have defined the exclusion process in terms of particle hopping, it can equally well be viewed as the backward motion of holes(sites on which there are no particles). The drift velocity for labelled holes is $v_{ho} = -(p - q)\rho$ and the steady state current is

$$j = \rho v_p = (1 - \rho)v_{ho} = \rho(1 - \rho)(p - q) \tag{2.27}$$

In time t, the mean vertical shift of the interface is given by the average number of particles which pass by a given hole, namely, $\rho(v_p - v_{ho})t$. The magnitude of the normal velocity is then $v_f = \rho(v_p - v_{ho})cos\theta = j(\sin\theta + \cos\theta)$ which may be rewritten as

$$v_f = \frac{\tanh\beta H}{(\sec\theta + \mathrm{cosec}\theta)}. \tag{2.28}$$
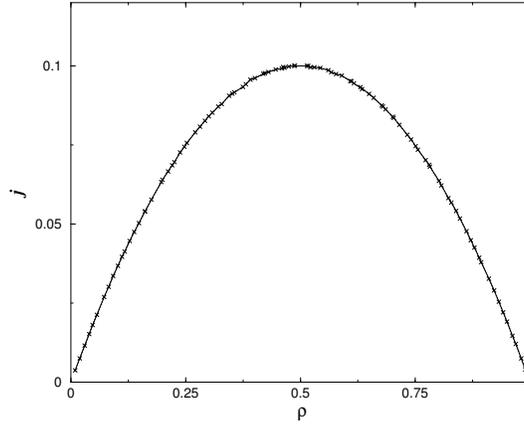
FIGURE 2.4: Plot of j versus density

The space dependent coarse-grained density $\rho(n)$ and current $J(n)$ are related through the continuity equation [36]

$$\frac{\partial \rho}{\partial t} + \frac{\partial J(n)}{\partial n} = 0. \tag{2.29}$$

Now the current $J(n)$ can be written as [42],

$$J(n) = -D\frac{\partial \rho}{\partial n} + j(\rho) + \eta, \tag{2.30}$$

where the first term is the usual diffusion of particles with diffusion constant D, η is a Gaussian white noise and $j(\rho)$ is the current due to the local density $\rho \equiv \rho(n)$. We may replace $j(\rho)$ by its macroscopic value (Eqn. 2.27) and expand it in power series in the density deviation $\Lambda = \rho - \overline{\rho}$ around the average density $\overline{\rho} = \mathcal{N}_p/\mathcal{N}$.

$$j(\rho) = \sum j_m \Lambda^m, \tag{2.31}$$

with $m! j_m = \partial^m J/\partial \rho^m$. The density fluctuation field $\Lambda(n, t)$ is related to the height variable $h(n, t)$ which measures the transverse displacement of the interface:

$$h(n, t) = \int_{n_0}^{n} \Lambda(n', t) dn'. \tag{2.32}$$

Differentiating Eqn. 2.32 and using Eqn. 2.29 and Eqn. 2.30 one can show that h satisfies the equation by KPZ [15]. The equation of motion of the interface is

$$\frac{\partial h}{\partial t} = D\frac{\partial^2 h}{\partial n^2} + \sum_m j_m [\frac{\partial h}{\partial n}]^m + \eta(n, t) \tag{2.33}$$

We consider the height fluctuation correlation function $S(n, t)$ defined by

$$S^2(n, t) \;\; = \;\; < (h(n, t) - h(n, 0) - v_p t)^2 > \tag{2.34}$$

The large-distance large-time behaviour of S(n,t) depends strongly on the first few coefficients j_m in Eqn. 2.33. The constant j_0 is equal to the macroscopic current (Eqn. 2.27) and determines the mean rate of growth of the interface. It can be eliminated by the boost $h \rightarrow h + j_0 t$.
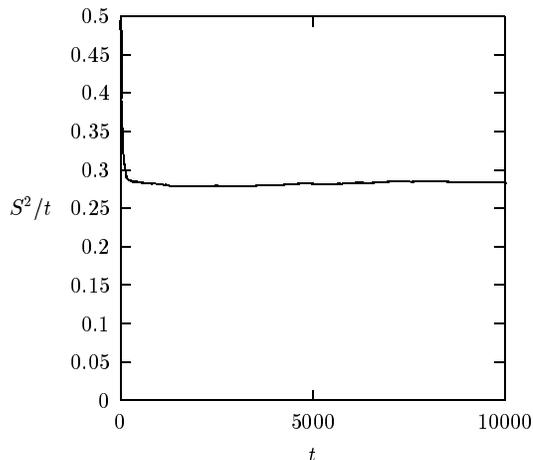
FIGURE 2.5: The second moment of the height distribution S^2/t as a function of time t.

The first-order gradient term j_1 is equal to U, the speed of local density variations or kinematic waves [43]. Kinematic waves, which transport density fluctuations in the lattice system, correspond to the movement of transverse fluctuations in the interface problem and owes its existence to the conservation of particle number. The term j_1 can be eliminated from Eqn. 2.34 by making the Galilean shift $x \rightarrow x + j_1 t$. This has the effect of moving to a coordinate system in which the wave is stationary. If the j_0 term is eliminated but j_1 is not, it can be shown that $S(0, t)$ grows as $t^{1/2}$. Since the sliding of the wave is the dominant physical effect so $S(0, t)$ is approximated by the equal time correlation function $S(n = Ut, 0)$. Since equal-time height fluctuations are determined by fluctuations of particle number, these grow as $n^{1/2}$, and it follows that

$$S(0, t) \sim (Ut)^{1/2}. \tag{2.35}$$

We have performed Monte Carlo simulations with random sequential updates of the particles to reproduce these exact results. This constituted the benchmarking and validation for our codes which were subsequently used to study the system discussed in Chapter 3. In Fig. 2.4 we show a plot of the measured current as a function of the density together with the exact result. $\mathcal{N}_s = 10000$ was used in this run. In Fig. 2.5 we have shown our results for the second moment of the height distribution function. Our Monte Carlo results clearly depicted the $t^{1/2}$ behaviour. We used $\mathcal{N}_s = 80000$ for this calculation.

3 Ising Interfaces in spatially varying external field : Novel fluctuations

In the last chapter we introduced the Ising model and the Ising interface. We studied the structure of this interface in two-dimensions and discovered that at any non zero temperature the interface is never flat but fluctuates rather strongly. The random fluctuations of the interface diverge as the system size as $L^{1/2}$ and with time as $t^{1/3}$.

In this chapter, we discover how to control these interfacial fluctuations and create an essentially flat interface. The ability to grow flat solid surfaces [44, 45] is often of major technological concern, for example, in the fabrication of magnetic materials for recording devices where surface roughness [46] causes a sharp deterioration of magnetic properties. We show that non-uniform external fields[1] which have a sharp gradient at the position of the interface, suppresses height fluctuations to a large extent. This is a direct consequence of the fact that such spatially varying fields break the translational symmetry of the interface in the direction of growth so that long wavelength fluctuations now do cost non zero interfacial energy. Surprisingly however we show that this suppression of long wavelength fluctuations generate new *short wavelength* structures and patterns. Driving the ineterface by using a moving field profile causes interesting dynamical transitions between patterns which are either commensurate or incommensurate with the underlying lattice structure over which the Ising model is defined.

Commensurate-in -commensurate (C-I) transitions [33] have been extensively studied over almost half a century following early experiments on noble gases adsorbed on a crystalline substrate [48] eg. Kr on graphite. Depending on coverage and temperature, adsorbates may show high density periodic structures the reciprocal lattice vectors (RLVs) of which are either a rational (commensurate) or irrational (in -commensurate) multiple of a substrate RLV. By changing external parameters (eg. temperature) one may induce phase-transitions between these structures. Recently, the upsurge of interest in the fabrication of nano-devices have meant a renewed interest in this field following a large number of experimental observations on "self-assembled" domain patterns (stripes or droplets) on epitaxially grown thin films for eg. Ag films on Ru(0001) or

---

[1]There are several practical examples where non-uniform fields drive interfaces. Some of them include zone purification of Si where the controlled motion of a temperature field profile is used to preferentially segregate impurities [47], magnetization of a bar of iron with a permanent magnet, phase transitions induced by a travelling heat (welding) or pressure (metamorphosis of rocks) fronts etc.

Cu-Pb films on Cu(111) [49] etc. The whole area of surface structure modifications and surface patterns has tremendous technological implications for example in opto-electronics, recording industry, coatings and paints, etc.

Almost universally, C-I transitions may be understood using some version of the simple Frenkel - Kontorova [50] model, which models them as arising from a competition between the elastic energy associated with the distortion of the adsorbate lattice and substrate -adsorbate interactions. A complicated phase diagram involving an infinity of phases corresponding to various possible commensuration ratios (rational fractions) is obtained as a function of the two energy scales. In-between two commensurate structures one obtains regions where the periodicity of the adsorbate lattice is in -commensurate.

The structures obtained in our interfacial problem, on the other hand, undergo C-I transitions which are entirely dynamical in origin and can be controlled by adjusting the velocity of the interface. Short periodic structures are stabilized at lower velocities. As the velocity of the interface approaches a limiting velocity v_∞, the patterns disappear and the interface begins to fluctuate over all length scales. Beyond v_∞, KPZ behaviour takes over.

3.1 The Model

We show in Fig. 3.1 a one-dimensional interface $h(x,t)$ between phases with magnetization, $\phi(x,y,t) > 0$ and $\phi(x,y,t) < 0$, in a two-dimensional Ising model on a square lattice [51] obeying single-spin flip Glauber dynamics [52] in the limit $H/J, \mathcal{T}/J \to 0$. An external non-uniform field is applied such that $H = H_{max}$ in the +ve and $-H_{max}$ in the -ve ϕ regions separated by a sharp *edge*. The *edge* of the field (i.e. where the field changes sign) lies at S_e. The *front* or interface, $h(x,t)$, (no overhangs !) separates up and down spin phases. The interface is shown as a bold curved line with the average position S_f. To move the interface we move the edge with
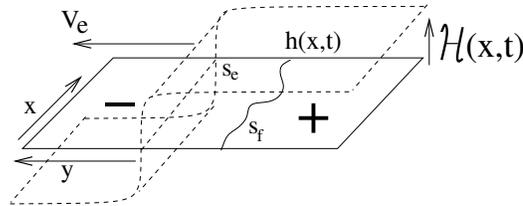
FIGURE 3.1: An Ising interface $h(x,t)$ (bold curved line) between regions of positive (marked $+$) and negative (marked $-$) magnetization in an external, inhomogeneous field with a profile which is as shown(dashed line). The positions of the edge of the field profile and that of the interface are labelled S_e and S_f respectively.

velocity v_e; in response the front moves with velocity v_f. Parts of the front which leads (lags) the

edge of the field experience a backward (forward) force pulling it towards the edge. The driving force therefore varies in both space and time and depends on the relative position of the front compared to that of the edge of the dragging field. In the low temperature limit the interface moves solely by random corner flips [10] , the fluctuations necessary for nucleating islands of the minority phase in any region being absent. We study the behaviour of the front velocity v_f and the structure of the interface as a function of v_e and orientation.
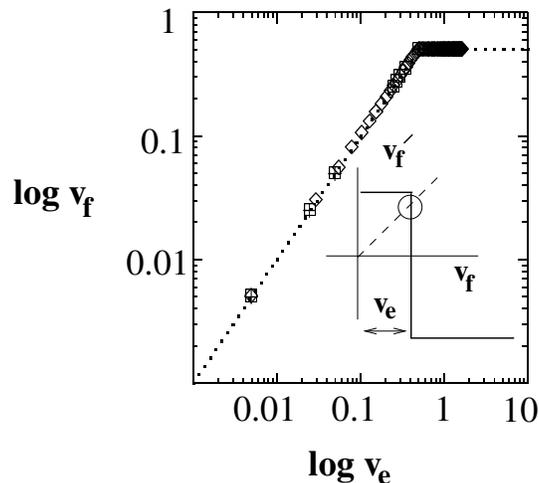
FIGURE 3.2: The interface velocity v_f as a function of the velocity of the dragging edge v_e for $\mathcal{N}_s = 100(\square), 1000(\lozenge), 10000(+)$ and $\rho = 0.5$. All the data $(\square, \lozenge, +)$ collapse on the mean field solution (dashed line). Inset shows the graphical solution (circled) of the self-consistency equation for v_f; dashed line represents $v_f = v_f$.

Naively, one would expect fluctuations of the interfacial coordinate $h(x,t)$ to be completely suppressed in the presence of a field profile. This expectation, is only partially true. While, as we show below, a mean field theory gives the exact behaviour of the front velocity v_f as a function of v_e; small interfacial fluctuations produce a dynamical phase diagram showing infinitely many dynamical phases. For $v_e < v_\infty$ the interface is stuck to the profile $v_f = v_e$. The stuck phase has a rich structure showing microscopic, "lock-in", commensurate ripples. These disappear at high velocities through a dynamical C-I transition. For large v_e the interface detaches from the profile and moves at velocity v_∞ corresponding to an uniform field of magnitude $H = H_{max}$ independent of v_e and coarsens with KPZ exponents.

3.2 Continuum Description

In the continuum description of this model, we need to substitute $H = H(h,t) = H_{max}f(h,t)$ with $f(h,t) = \tanh((h - v_e t)/\chi)$ where χ is the width of the profile (see Fig 3.1) in the equation

for the Hamiltonian in Eqn. 2.22. Carrying out an analogous procedure for obtaining the equation of motion for the interface we obtain a generalized KPZ equation for the dynamics of the interface in a spatially varying field. The result analogous to Eqn. 2.24 is

$$\frac{\partial h}{\partial t} = \lambda_1 \frac{\partial^2 h}{\partial x^2} - \lambda_2 \left(\frac{\partial h}{\partial x}\right)^2 f(h, t) - \lambda_3 f(h, t) + \zeta(x, t) \tag{3.1}$$

A mean field calculation amounts to taking $h \equiv h(t)$ i.e. neglecting spatial fluctuations of the interface and noise. For large times $(t \to \infty)$, $h \to v_f t$, where v_f is obtained by solving the self-consistency equation;

$$\begin{aligned} v_f &= \lim_{t \to \infty} -\lambda_3 \tanh\left(\frac{(v_f - v_e)t}{\chi}\right) \\ &= -\lambda_3 \operatorname{sign}(v_f - v_e) \end{aligned} \tag{3.2}$$

For small v_e the only solution to Eqn. 3.2 is $v_f = v_e$ and for $v_e > v_\infty$, where $v_\infty = \lambda_3$ we get $v_f = \lambda_3 = v_\infty$. We thus have a sharp transition (Fig. 3.2) from a region where the interface is stuck to the edge to one where it moves with a constant velocity. How is this result altered by including spatial fluctuations of h ? We answer this question by mapping the interface problem to an asymmetric exclusion process [10, 40, 41] and studying the dynamics both analytically and numerically using computer simulations.

3.3 Beyond Mean Field Theory

The mapping to the exclusion process follows [35, 37, 40, 41, 53] as in the previous chapter by distributing $\mathcal{N}_p$ particles among $\mathcal{N}_s$ sites of a 1-d lattice. The particles are labelled $i = 1, 2, \ldots, \mathcal{N}_p$ sequentially at $t = 0$. Any configuration of the system is specified by the set of integers $\{h_i\}$ where h_i denotes the location of the ith particle. In the interface picture i maps onto a horizontal coordinate (x in Fig. 3.1), and h_i as the local height $h(x)$. Each configuration $\{h_i\}$ defines a one-dimensional interface inclined to the horizontal with mean slope $\tan\theta_f = 1/\rho$ where $\rho = \mathcal{N}_p/\mathcal{N}_s$. The h_i satisfy the hard core constraint $h_{i+1} \geq h_i + 1$. The local slope near particle i is given by $h_{i+1} - h_i$ and is equal to the inverse *local* density ρ_i measured in a region around the ith particle. Alternatively, one associates a vertical bond with a particle and a horizontal bond with a hole [35, 53], in which case, again, we obtain an interface with a slope $\tan\theta'_f = \rho/(1 - \rho)$. The two mappings are distinct but equivalent. Periodic boundary conditions amount to setting $h_{i+\mathcal{N}_p} = h_i \pm \mathcal{N}_s$. Motion of the interface, by corner flips corresponds to the hopping of particles. In each time step ($\mathcal{N}_p$ attempted hops with particles chosen randomly and sequentially [40, 41]), h_i tends to increase (or decrease) by 1 with probability p (or q); it actually increases (or decreases) if and only if $h_{i+1} - h_i > 1$. The dynamics involving random sequential updates is known to introduce the least amount of correlations among h_i which enables one

to derive exact analytic expressions for dynamical quantities using simple mean field arguments [40, 41] (see chapter 2). The right and left jump probabilities p and q $(p + q = 1)$ themselves depend on the relative position of the interface h_i and the edge of the field profile $i/\rho + v_e t$. Note that this relative position is defined in a moving reference frame with velocity $v_f(t)$, the instantaneous average particle velocity defined as the total number of particles moving right per time step. We use a bias $\Delta_i(t) = p - q = \Delta \operatorname{sign}(h_i - i/\rho - v_e t)$ with $\Delta = 1$ unless otherwise stated. Our model is thus a generalization of the one-dimensional exclusion process with space dependent, dynamic jump probabilities [37, 38]. In addition to the front velocity v_f, we also examine the behaviour of the average position,

$$< h(t) > = \mathcal{N}_p^{-1} \sum_{i=1, \mathcal{N}_p} h_i(t) \tag{3.3}$$

and the width of the interface:

$$w^2(t) \quad = \quad \mathcal{N}_p^{-1} \sum_{i=1, \mathcal{N}_p} < (h_i(t) - < h_i(t) >)^2 > \tag{3.4}$$

as a function of time and system size $\mathcal{N}_s$. Here, $< h_i(t) > = i/\rho + v_e t$. Angular brackets denotes an average over the realizations of the random noise. Note that the usual particle hole symmetry for an exclusion process [10, 40, 41] is violated since exchanging particles and holes changes the relative position of the interface compared to the edge. This violation is, of course, completely equivalent to the breaking of translation symmetry of the interface in the growth direction as mentioned before (chapter 1).

We perform numerical simulations of the above model for $\mathcal{N}_s$ upto 10^4 to obtain v_f for the steady state interface as a function of v_e as shown in Fig. 3.2. A sharp dynamical transition from an initially stuck interface with $v_f = v_e$ to a free, detached interface with $v_f = v_\infty = \Delta(1 - \rho)$ is clearly evident as predicted by mean field theory. The detached interface coarsens with KPZ exponents [54]. Note that, even though the mean field solution for $v_f(v_e)$ neglects the fluctuations present in our simulation, it is exact. The detailed nature of the stuck phase ($v_f = v_e$ and w bounded) is, on the other hand, considerably more complicated than the mean field assumption $h(x, t) = h(t)$. Below we analyse the nature of the stuck phase starting from the ground state configurations at $v_e = 0$.

3.3.1 The Ground State and the Devil's Staircase

The ground state of the interface in the presence of a stationary ($v_e = 0$) field profile is obtained by minimizing $E = \sum_i (h_i - i/\rho - c)^2$ with respect to the set $\{h_i\}$ and c. This maybe shown from Eqn 3.1 by neglecting terms containing spatial derivatives of h; the resulting equation of motion, for small deviations of h from the edge may be derived from the effective Hamiltonian

E. The form of E leads to an infinite range, non-local, repulsive, interaction between particles in addition to hard core repulsion and the minimization is subject to the constraint that h_i be an integer. For our system, the result for the energy may be obtained exactly for density $\rho = m/n$, an arbitrary rational fraction. For even m we have the following expression.

$$
\begin{aligned}
E &= \frac{1}{m}\left[(\frac{1}{m} - c)^2 + (\frac{1}{m} + c)^2 + (\frac{2}{m} - c)^2 + (\frac{2}{m} + c)^2\right.\\
&\quad + \quad .... + (\frac{\frac{m}{2}}{m} - c)^2 + (\frac{\frac{m}{2}}{m} + c)^2 + (\frac{1}{2} - c)^2 + c^2\left.\right]\\
&= \frac{1}{6}(\frac{1}{2} - \frac{1}{m})(1 - \frac{1}{m}) + \frac{1}{m}(mc^2 + \frac{1}{4} - c) \quad\quad (3.5)
\end{aligned}
$$

Minimising with respect to c, we get $c = \frac{1}{2m}$. Substituting for c we get the expression for minimized energy as

$$
E = \frac{1}{6}(\frac{1}{2} - \frac{1}{m})(1 - \frac{1}{m}) + \frac{1}{4m} - \frac{1}{4m^2} \quad\quad (3.6)
$$

Similarly for odd m we have the following expression for energy,

$$
\begin{aligned}
E &= \frac{1}{m}\left[(\frac{1}{m} - c)^2 + (\frac{1}{m} + c)^2 + (\frac{2}{m} - c)^2 + (\frac{2}{m} + c)^2\right.\\
&\quad + \quad .... + (\frac{\frac{m}{2}}{m} - c)^2 + (\frac{\frac{m}{2}}{m} + c)^2 + c^2\left.\right]\\
&= \frac{1}{12}(1 - \frac{1}{m^2}) + c^2 \quad\quad (3.7)
\end{aligned}
$$

which when minimised with respect to c gives $c = 0$. Hence, the minimised energy for odd m is given by

$$
E = \frac{1}{12}(1 - \frac{1}{m^2}) \qu\quad (3.8)
$$

The resulting ground state profiles are shown in Fig. 3.4. The lower bound for $E(\rho)$ is zero which is the energy for all $\rho = 1/n$. For irrational ρ the energy is given by $\lim_{m\to\infty} E(m/n) = 1/12$ for both even and odd m which constitutes an upper bound (Fig. 3.3). For an arbitrary $0 < \rho < 1$ the system ($\{h_i\}$) therefore prefers to distort, conforming within local regions, to the nearest low-lying rational slope $1/\tilde{\rho}$ interspersed with "discommensurations" of density $\rho_d = |\rho - \tilde{\rho}|$ and sign +ve (-ve) if these regions are shifted towards (away) from each other by 1. A plot of $\tilde{\rho}(\rho)$ shows a "Devil's staircase" structure [55, 56]. We observe this in our simulations by analysing the instantaneous distribution of the local density of the particle-hole system to obtain weights for various rational fractions. A time average of these weights then give us the most probable density $\tilde{\rho}$ - distinct from the average ρ which is constrained to be the inverse slope of the interface.
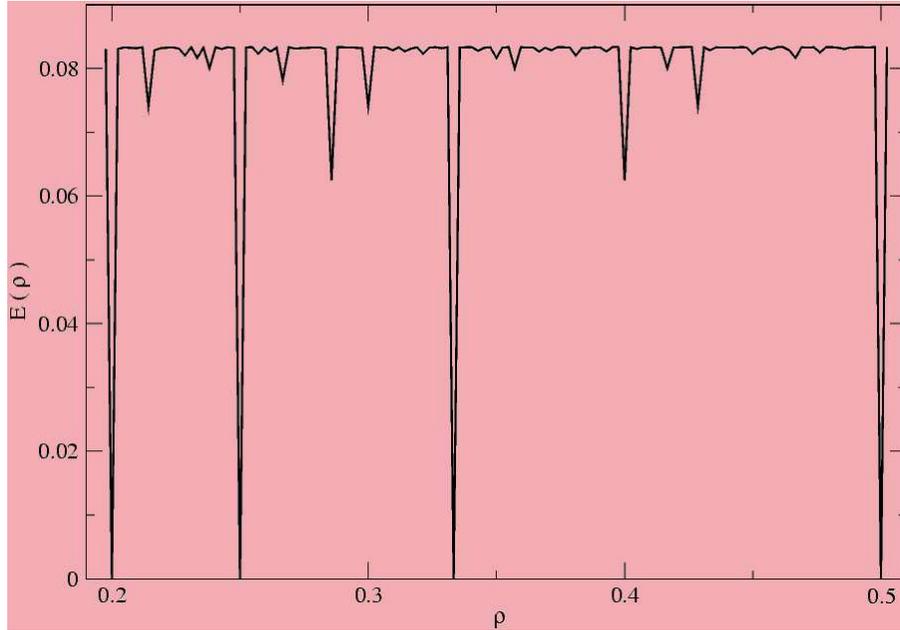
FIGURE 3.3: Plot of $E(\rho)$ for a $\mathcal{N}_s = 420$ site system.

3.3.2 Dynamics of interfacial patterns for small v_e

What are the low lying excitations of the ground state structures ? For low velocities and density where correlation effects due to the hard core constraint are negligible, the dynamics of the interface may also be obtained exactly. Under these circumstances the $\mathcal{N}_p$ particle probability distribution for the h_i's, $P(h_1, h_2, \cdots, h_{\mathcal{N}_p})$ factorizes into single particle terms $P(h_i)$. Knowing the time development of $P(h_i)$ and the ground state structure the motion of the interface at subsequent times may be trivially computed as a sum of single particle motions. A single particle (with say index i) moves with the bias $\Delta_i(v_e\,t)$ which, in general, may change sign at $h < i/\rho + v_e\,t < h + 1$. Then $P(h_i)$ satisfies the following set of master equations,

$$\begin{aligned}
\dot{P}(h_i) &= -P(h_i) + P(h_i + 1) & \text{for } h_i > h+1 \\
\dot{P}(h_i) &= P(h_i - 1) - P(h_i) + P(h_i + 1) & \text{for } h_i = h, h+1 \\
\dot{P}(h_i) &= -P(h_i) + P(h_i - 1) & \text{for } h_i < h.
\end{aligned} \tag{3.9}$$

Note that the average position of the particle is given simply by $< h_i(t) >= \sum_{h_i=-\infty}^{\infty} h_i\,P(h_i)$ and the spread by $w^2(t) = \sum_{h_i=-\infty}^{\infty}(h_i - < h_i(t) >)^2\,P(h_i)$. Solving the appropriate set of master equations we obtain, for $v_e << 1$ the rather obvious steady state solution $P(h_i) = 1/2(\delta_{h_i,h} + \delta_{h_i,h+1})$ and the particle oscillates between h and $h+1$. Subsequently, when $i/\rho + v_e\,t \geq h+1$, the particle jumps to the next position and $P(h_i)$ relaxes exponentially with a time constant
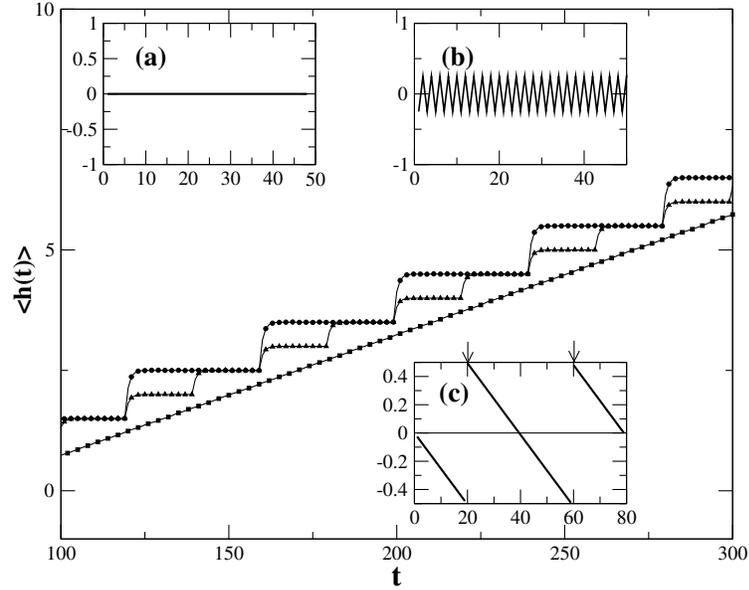
FIGURE 3.4: Variation of $< h(t) >$ with t for $v_e = 0.025$ and $p = 1.0$. Lines denote analytic results while points denote Monte Carlo data for $\rho = 1/5$ (uppermost curve), $2/5$ and an incommensurate ρ near $1/3$. Inset (a)-(c) shows the corresponding ground state interfaces ($h_i - i/\rho$). The arrows in (c) mark the positions of two discommensurations.

$\tau = 1$ to it's new value with $h \to h + 1$. For $\rho = 1/n$ the entire interface moves as a single particle and the average position advances in steps with a periodicity of $1/v_e$ (see Fig. 3.4)

In general, for rational $\rho = m/n$, the motion of the interface is composed of the independent motions of m particles each separated by a time lag of $\tau_L = 1/m\,v_e$. The result of the analytic calculation for small v_e and ρ has been compared to those from simulations in Fig. 3.4 for $\rho = 1/5$ and $2/5$. For a general irrational $\rho < 1/2$, $m \to \infty$ consequently, $\tau_L \to 0$. The h_i's are distributed uniformly around the mean implying $w^2 = 1/3$ independent of system size and time. For $\rho > 1/2$ the width $w^2 = (1 - \rho)/3\rho$ since the number of mobile particles decreases by a factor of $(1 - \rho)/\rho$.

In chapter 2, we encountered kinematic waves which were travelling density modulations in the exclusion process which, in the interface picture, represent height fluctuations which travel along the interface with velocity $U = \partial J/\partial \rho$. In this case too, the forward motion of the interface is accompanied by the motion of discommensurations along the interface. The velocity of these kinematic waves in this system, however, is constrained to be equal to v_e.

As the velocity v_e is increased, the time lag, τ_L, decreases and the patterns begin to get distorted τ_L becomes comparable with the MC time step. The instantaneous values of $\tilde{\rho}$ begins to make excursions to other nearby fractions and eventually becomes free. Since τ_L is smaller for large m, higher order fractions becomes unstable earlier. In Fig. 3.5, thus effect is clearly
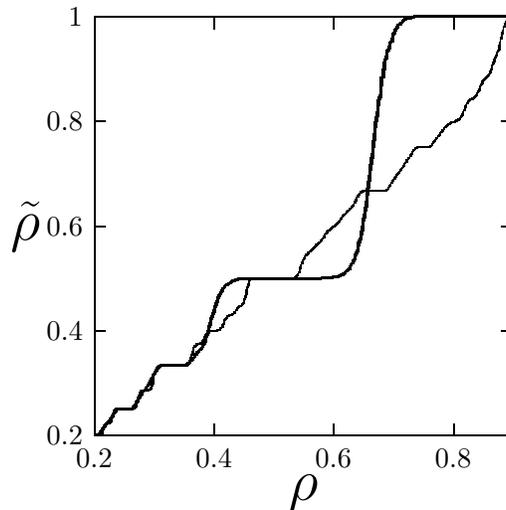
FIGURE 3.5: Devil's staircase structure for two different velocities. Steps disappear as velocity of the edge increases.

visible; the Devil's staircase for the $\tilde{\rho}(\overline{\rho})$ curve for the higher velocity has fewer steps. Steps corresponding to $\tilde{\rho} = m/n$ disappear (i.e. $\tilde{\rho} \to \rho$) sequentially in order of decreasing m and the interface losses the ripple patterns.

3.3.3 Dynamical transitions and the dynamical phase diagram

The beginning and end points of each step in the $\tilde{\rho}(\overline{\rho})$ curve (Fig. 3.5) mark the stability limits for each of the patterns which may be regarded as distinct dynamical phases. The locus of these points as a function of v_e trace out the dynamical phase diagram which is shown in Fig. 3.6. As expected, fractions with higher values of m disappear as v_e increases making way for simpler structures. We thus have true dynamical transitions from more complicated to simpler patterns as v_e approaches v_∞. Beyond v_∞, the interface detaches and we get back the KPZ interface.

The sequential smoothening of the Devil's staircase may be naturally described using the language of multifractals. For every v_e, we first obtain the generalized dimension D_k. For this purpose we obtain the scales l_i which are the differences in ρ between subsequent rational fractions in the Farey construction (e.g. $\rho = 0, 1, 1/2, 1/3, 2/3$, etc). For every scale, the corresponding measure π_i is given by the jump in $\tilde{\rho}$ which depends on v_e and the structure of the Devil's staircase. The generalized dimension D_k is obtained for any given value of k by solving

$$\sum_i (\pi_i^k / l_i^{(k-1)D_k}) = 1. \tag{3.10}$$

Once D_k is obtained as a function of k, $f(\alpha)$, the multifractal spectrum of singularities, is
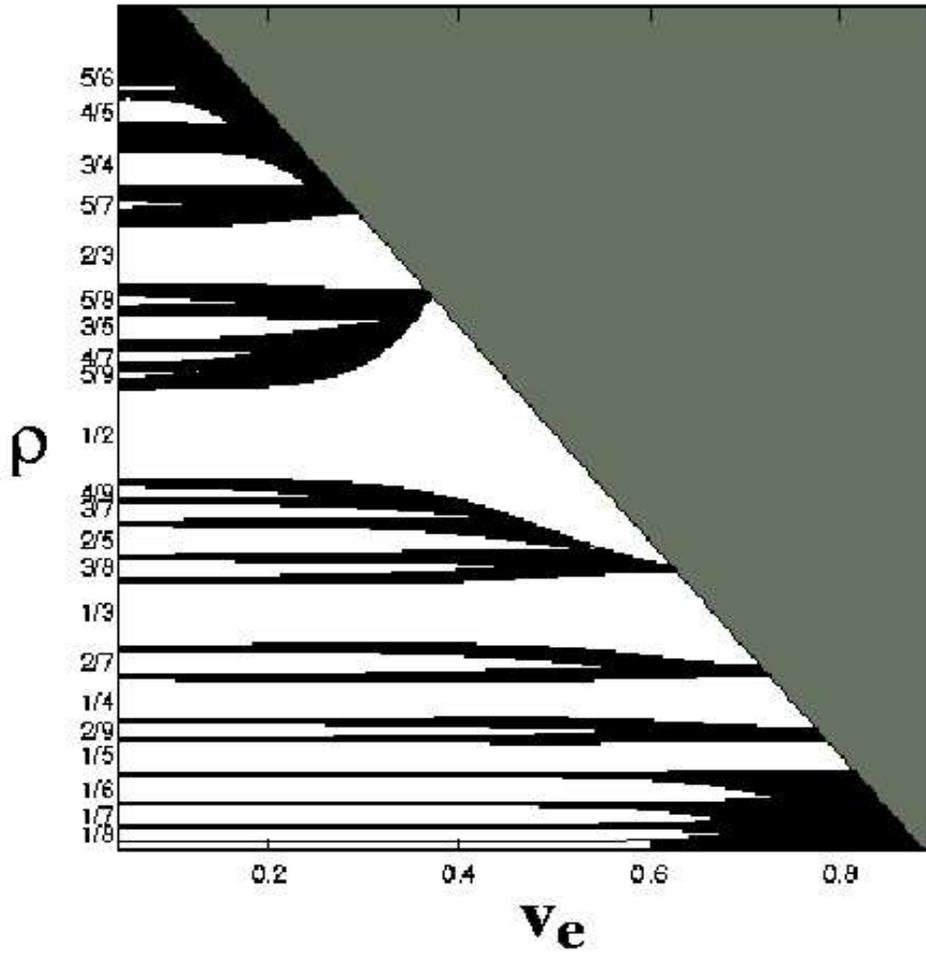
FIGURE 3.6: The dynamical phase diagram in v_e and ρ plane. The numbers on the ρ axis mark the fractions $\tilde{\rho}$, which determines the orientation of the lock-in phase. The three regions white, black and grey correspond to the rippled, the disordered and the detached phases respectively.

obtained by a Legendre transform of $(k-1)D_k$ (see Fig. 3.7).

$$\alpha(k) = \frac{d}{dk}[(k-1)D_k]$$

$$f(\alpha) = k\frac{d}{dk}[(k-1)D_k] - (k-1)D_k \qquad (3.11)$$

In the vicinity of the primary steps corresponding to $\rho = 1/n$, $\tilde{\rho} \sim (\rho - \rho_{max})^\xi$ where ρ_{max} is the largest density at which the step is stable. This universal critical exponent [57] $\xi = D_\infty$ has been determined to be $0.71 \pm .001$ from our data at $v_e/(1-\rho) = 0.1$. The exponent ξ determines how strongly $\tilde{\rho}$ diverges away from its value at a step for small changes in ρ. Since the density ρ is related to the average orientation of the interface which is in turn determined by the orientation
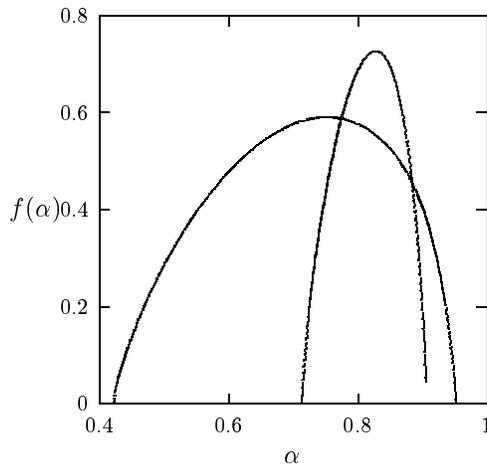
FIGURE 3.7: The multifractal spectrum $f(\alpha)$ for two different velocities $v_e/(1-\rho) = 0.1$ and 0.5.. Note that with increasing velocity, $\alpha_{min} \to 0$ (see text).

of the external field profile, ξ determines the stability of the ripple pattern to small changes in the external field. As v_e increases, $\xi \to 0$ implying that the $1/n$ steps become extremely stable at the expense of those corresponding to higher order rational fractions.

The nature of the C-I transitions discussed here is essentially new and fundamentally different from that described within the Frenkel-Kontorowa (F-K) model. Indeed the control parameter for our phase diagram is v_e - a dynamical parameter. Also, the non local $E(\rho)$ and the non linear constraint $h_i = integer$ makes it impossible to devise a natural mapping of this problem to an effective F-K model. We therefore use a different approach as discussed below.

3.4 Langevin Dynamics

While the stability of mismatch domains [56] is decided, mainly, by competition between mechanical, long-ranged (elastic) and short-ranged (atomistic) interactions [55], dynamical ripples vanish with increasing v_e through increased fluctuations. We argue that it is sufficient to project the entire configuration space h_i of the stuck interface onto the single variable ρ. As is obvious from the energy versus rho diagram (Fig. 3.3) $E(\rho)$ has a structure similar to the free energy surface of a 1-d "trap" model [58] often used to describe glassy dynamics. The distinction, of course, is the fact that the energies of the traps in this case are highly correlated. We now attempt to describe the dynamics of the stuck interface as the Langevin dynamics viz.

$$
\begin{aligned}
\dot{\rho}' &= -\frac{dF}{d\rho'} + \eta_{\rho'} \\
< \eta_{\rho'}(t)\eta_{\rho'}(t') > &= 2\,T\,\delta(t-t')
\end{aligned}
\tag{3.12}
$$
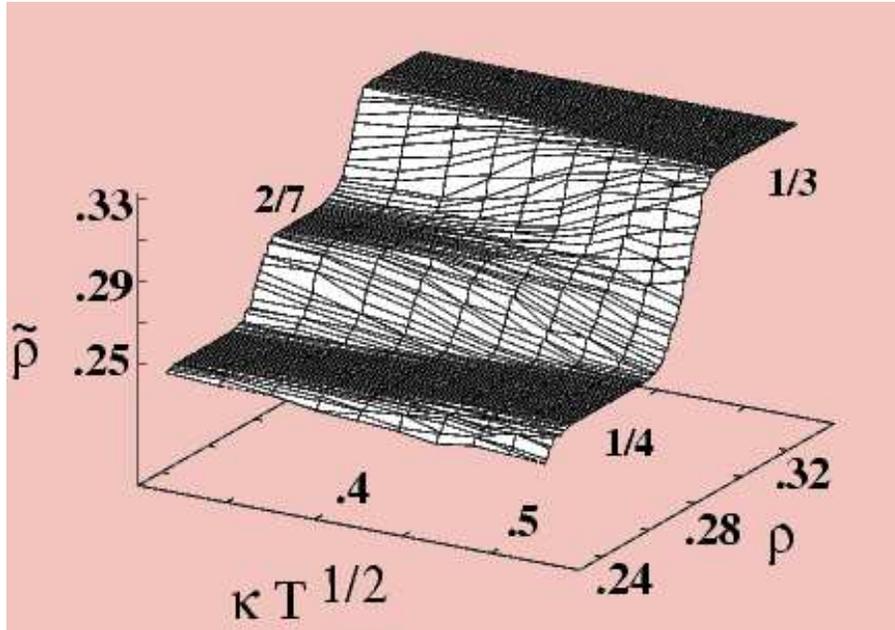
FIGURE 3.8: A surface plot of $\tilde{\rho}$ vs ρ and $\sqrt{T}\kappa$ showing steps for the fractions $1/4, 2/7$ and $1/3$. Note that the step corresponding to $2/7$ vanishes at $\sqrt{T}\kappa > 0.5$.

of a single particle with coordinate ρ' diffusing on a energy surface given by,

$$F(\rho') = E(\rho') + \kappa \left(\rho' - \rho\right)^2. \tag{3.13}$$

The particle is kicked by a Gaussian white noise (η_ρ) of strength T. The second term, containing the modulus κ, ensures that for infinitely large times ρ' always relaxes to the true global minimum $\rho' = \rho$. At intermediate times, however, the system may get trapped indefinitely in some nearby low-lying minimum with $\rho' = \tilde{\rho}$ if the noise strength T is not large enough. When the time taken for jumping between minima exceeds the residence time in any minimum because of enhanced noise, we have a fluctuation induced C-I transition (Fig. 3.8) from that density ρ. To show this we obtain the limiting value of ρ' averaged over realisations of the noise as a function of ρ and T from a numerical solution of Eqn. 3.12. While it is difficult to make a direct quantitative connection between T and v_e symmetry considerations would require $T \propto v_e^2$. In Fig. 3.8 we have plotted $\tilde{\rho}(\rho, T)$ for $1/4 < \rho < 1/3$ showing prominent steps for $\tilde{\rho}$ corresponding to the rational fractions $1/4, 1/3$ and $2/7$. The steps for $2/7$ vanish at the square root of the noise amplitudes as $1/2$ which is as expected.

3.5 Behavior at the transition point

We want to determine scaling form for $w(t)$ at the transition point viz. the growth exponent β, the roughness exponent α and the dynamic exponent z. In the detached phase we know from renormalization group analysis that the exponents are in the KPZ universality class [10, 15] viz. $\beta = 1/3$, $\alpha = 1/2$ and $z = \alpha/\beta = 3/2$. To determine these exponents at the transition point we make use of *Family-Vicsek* scaling relation [10]

$$w(L,t) \sim \mathcal{N}_s^\alpha f(t/\mathcal{N}_s^z) \tag{3.14}$$

Fig. 3.9 shows the variation of $t/\mathcal{N}_s^z$ with $w(L,t)/\mathcal{N}_s^\alpha$ for different p and different system sizes $\mathcal{N}_s$. The curves collapse onto one curve once an intrinsic width w_i, arising from finite-size and crossover effects [10], is subtracted out. The exponents were found to be KPZ.
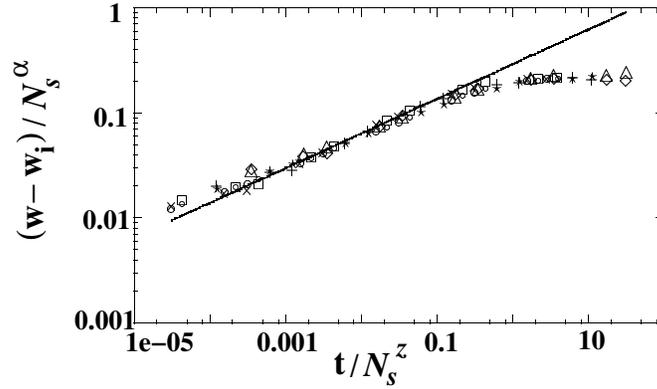
FIGURE 3.9: Monte Carlo data $(w - w_i)/\mathcal{N}_s^\alpha$ vs $t/\mathcal{N}_s^z$ for $p = 1.0$, $p = 0.7$ and with $\mathcal{N}_s = 1000$ [$\times$,$\bigcirc$] , 800 [$\square$,$\circ$] , 400 [$+$,$\star$] , 200 [$\Diamond$,$\triangle$]. All the curves collapse to a single universal function showing KPZ scaling.

To understand why this happens we go back to our modified KPZ equation Eqn. 3.1 and make the transformation $h = h' + v_f t$. We get

$$\begin{aligned}
\frac{\partial h'}{\partial t} + v_f &= \lambda_1 \frac{\partial^2 h'}{\partial h^2} - \lambda_2 \left(\frac{\partial h'}{\partial h}\right)^2 \tanh\left(\frac{(v_f - v_e)t + h'}{\chi}\right) \\
&\quad - \lambda_3 \tanh\left(\frac{(v_f - v_e)t + h'}{\chi}\right) + \zeta'(h', t)
\end{aligned} \tag{3.15}$$

Now substituting the mean field result for v_f (Eqn. 3.2), making use of the fact that at the transition point $v_f = \lambda_3$ and simplifying one can show that the above equation reduces to the familiar KPZ equation in h'.

3.6 Overview, caveats and conclusion

In this chapter we have shown how Ising interfaces in spatially varying, dynamical fields can give rise to interesting and new phenomena like dynamical C-I transitions. We hope that our study may lead to experimental work on real interfaces in carefully controlled and shaped external fields which may be used to carve static or dynamical patterns with technological applications. There are several problems which need to be sorted out before these techniques begin to have any practical application.
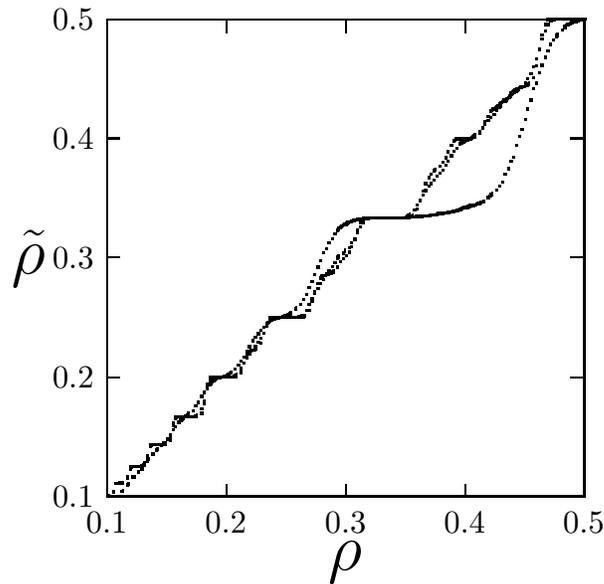
FIGURE 3.10: Devil's staircase structure for $v_e = 0.05$ and $1/\chi = 0.01, 1, 5$.

Firstly, the sharpness of the field profile directly influences the "resolution" of the patterns, Even at small velocities, as the width of the profile χ increases, the steps in the Devil's staircase corresponding to particular patterns disappear (Fig. 3.10) - simpler patterns being more stable as expected. In order to obtain the more interesting patterns therefore one needs the field profile to be atomistically sharp. Secondly, the most useful interfaces are two dimensional and therefore our studies need to be extended to higher dimensions and for other underlying crystal structures. We believe that there are exciting possibilities to be explored in this direction. Lastly, Ising interfaces miss two very important characteristics of real interfaces. (1) Elastic distortions and the effects of interfacial stress and (2) the possibility of particle transfers between the two phases. It is this last possibility that we explore in the subsequent chapters where we look at a two dimensional liquid solid interface stabilized by a spatially varying chemical potential field.

4 Atomic Systems

4.1 Introduction

In the last two chapters we have concentrated on interfaces in the two dimensional Ising model. Ising interfaces are particularly simple because they represent spatial variation of only a single scalar order parameter - the magnetization. Real interfaces in condensed matter systems are much more complex. In a liquid - solid interface for example, in principle, one has to consider the variation of an infinity of order parameters corresponding to all the Fourier components of the non-uniform solid density $\rho(r)$. We shall study liquid - solid interface in Chapters 5 and 6. This will involve simulations of systems composed of particles, or atoms, with interatomic potentials. Before we go on to describe our work on atomic systems, we use this chapter to introduce the model interatomic potentials we consider. We then briefly describe the computational techniques employed to compute a host of useful thermodynamic, structural and dynamical quantities after defining each of them appropriately. Wherever possible, we have compared our results with those available in the literature. This constitutes a check on our methods and a verification of the codes that we use later to perform simulations of the liquid - solid interface.

4.2 Models for atomistic systems

Consider a system containing $\mathcal{N}$ atoms. We may divide the potential energy into terms depending on the coordinates of individual atoms, pairs, triplets, etc. as :

$$\mathcal{V} = \sum_i u_1(\mathbf{r}_i) + \sum_i \sum_{j>i} u_2(\mathbf{r}_i, \mathbf{r}_j) + \sum_i \sum_{j>i} \sum_{k>j>i} u_2(\mathbf{r}_i, \mathbf{r}_j, \mathbf{r}_k) + ... \qquad (4.1)$$

$\sum_i \sum_{j>i}$ notation indicates a summation over all distinct pairs i and j without counting any pair twice; similarly for triplets, etc. The first term $\sum_i u_1(\mathbf{r_i})$ represents the effect of an external field on the system. The remaining terms represent particle interactions. The second term, u_2, the pair potential, depends on the magnitude of the pair separation $r_{ij} = |\mathbf{r}_i - \mathbf{r}_j|$, so it may be written $u_2(r_{ij})$. The triplet u_3 term is ignored in our thesis The pairwise approximation gives a remarkably good description of most atomic systems because the average three-body effects can

be usually included by defining an "effective" pair potential. To do this, we rewrite Eqn. (4.1) in the form

$$\mathcal{V} \approx \sum_i u_1(\mathbf{r}_i) + \sum_i \sum_{j>i} u_2^{eff}(\mathbf{r}_i, \mathbf{r}_j) \tag{4.2}$$

For simplicity, we use the notation $u(r_{ij})$ or $u(r)$ for the pair potential.

Effective pair potentials

In our simulations to model atomistic systems we have chosen different pair potentials. We discuss them briefly with special emphasis on two-dimensional results.

- The hard core potential is defined by a pair interaction between two classical particles with a non-overlap condition. It is given as

$$
\begin{aligned}
u^{HS}(r) &= \infty \quad (r < \sigma) \\
&= 0 \quad (\sigma \leq r)
\end{aligned}
\tag{4.3}
$$

  where σ is the diameter of the spheres and r is the distance between the two centers of the spheres. A peculiarity of the hard core potential is that it sets a length scale, σ, but it does not set any energy scale. A configuration of two overlapping spheres cost an infinite energy. Since u^{HS} can only take two values 0 and ∞, therefore, for the Boltzmann factor, we get, $e^{-\beta u^{HS}} = e^{-u^{HS}}$, $\beta = 1/k_B \mathcal{T}$. Thus, the temperature scales out trivially. Or, in other words, hard objects are *athermal*; all their structural and thermodynamical properties do not depend on temperature so that the density $\rho = N/V$ (or the packing fraction η, which is the ratio of the volume of the N spheres and the total accessible volume, V) is the only relevant thermodynamical variable. Due to this temperature independence, the hard sphere model is the simplest non-trivial model for an interaction. A lot of results exist for the hard sphere model (see [59] and references therein) which makes it useful as a reference system for systems with more complicated interactions and particle shapes. Moreover, the equilibrium thermodynamic properties of the hard sphere model can actually be probed in nature by examining suspensions of spherical sterically-stabilized colloidal particles [59].

  In the two-dimensional case of hard disks the close-packed area fraction is $\eta_c \equiv \pi \rho_c \sigma^2/4 = \pi/2\sqrt{3} = 0.907...$ corresponding to a perfect triangular lattice with long-ranged translational order. The existence of only two phases, fluid and solid, and a freezing transition from one to the other as the packing fraction is changed has been confirmed by extensive simulations of this model system [60, 61]. Hard disks form a key system in our understanding of both equilibrium and dynamical aspects of a model liquid-solid interface.

- The soft sphere potential is defined as

$$u^{SS}(r) = \epsilon \left(\frac{\sigma}{r}\right)^{\nu} = ar^{-\nu} \tag{4.4}$$

where ν is a parameter, often chosen to be an integer. σ and ϵ have the dimensions of length and energy. The soft-sphere potential becomes progressively "harder" as ν is increased. Soft sphere potentials contain no attractive part. This retains some of the simplicity of hard spheres in the sense that there is again one thermodynamic variable. To understand this, note that we can eliminate the explicit temperature dependence by defining $\sigma* = (\beta\epsilon)^{1/\nu}\sigma$ and rewriting Eqn. 4.4 as $\beta u^{SS}(r) = (\sigma*/r)^{\nu}$. The dimensionless excess (over the ideal gas) thermodynamic properties then depend only on the single dimensionless state variable

$$\rho* \equiv \rho\sigma*^{2} = \rho\sigma^{2}(\beta\epsilon)^{2/\nu} \tag{4.5}$$

Here again we have only two phases but unlike hard systems, soft sphere potential is analytic everywhere. In our simulation we use $\nu = 12$. For the two dimensional system of soft disks (with $\nu = 12$), a lot of simulation results exist, including the phase diagram and an empirical equation of state [62].

- The Lennard-Jones 12-6 potential :

$$u^{LJ}(r) = 4\epsilon \left[\left(\frac{\sigma}{r}\right)^{12} - \left(\frac{\sigma}{r}\right)^{6}\right] \tag{4.6}$$

This potential has a long-range attractive tail of the form $-1/r^{6}$, a negative well of depth ϵ, and a steeply rising repulsive wall at distances less than $r \sim \sigma$. The Lennard-Jones potential is extensively used to model atomistic systems and indeed provides a fair description of the interaction between pairs of rare-gas atoms [63].

4.3 Methods for simulations

We shall now introduce the various simulation methods that are generally used in simulating atomic systems and in particular those that we have used in this thesis to understand the behavior of liquid - solid interfaces. We begin by briefly discussing the generic Monte Carlo and molecular dynamics methods. Special emphasis has been given to explain the simulation of hard systems which require some care during simulations to handle the associated non analyticities. We include this section in this thesis mainly for completeness. There exist, of course, excellent textbooks [64, 65] which explains these techniques in great detail.

4.3.1 The Monte Carlo method

Consider the $\mathcal{N}$ particle system. The classical expression for the thermal average of an observable $\mathcal{A}$ is given by

$$\langle\mathcal{A}\rangle = \frac{\int d\mathbf{p}^N d\mathbf{r}^N \mathcal{A}(\mathbf{r}^\mathcal{N}, \mathbf{p}^\mathcal{N}) \exp[-\beta\mathcal{H}(\mathbf{r}^N, \mathbf{p}^N)]}{\int d\mathbf{p}^N d\mathbf{r}^N \exp[-\beta\mathcal{H}(\mathbf{r}^N, \mathbf{p}^N)]} \tag{4.7}$$

where $\mathbf{r}^N$ stands for the coordinates of all N particles, and $\mathbf{p}^N$ for the corresponding momenta and $\beta = 1/k_B T$. $\mathcal{H}(\mathbf{r}^N, \mathbf{p}^N)$ is the Hamiltonian of the system. As $\mathcal{H}$ is a quadratic function of the momenta, the integration over momenta can be carried out analytically. The integral over particle coordinates is carried out numerically by the Monte Carlo method or, more precisely, the Monte Carlo importance-sampling algorithm introduced in 1953 by Metropolis *et. al.*.

A basic Monte Carlo algorithm

In the approach introduced by Metropolis *et. al.* the following scheme is proposed :

- Select a particle at random, and calculate its energy $\mathcal{U}(\mathbf{r}^N)$.

- Give the particle a random displacement; $r' = r + \Delta$, and calculate its new energy $\mathcal{U}(\mathbf{r}'^N)$

- Accept the move from $\mathbf{r}^N$ to $\mathbf{r}'^N$ with probability

  $$acc(o \rightarrow n) = min(1, \exp\{-\beta[\mathcal{U}(n) - \mathcal{U}(o)]\}) \tag{4.8}$$

  In order to decide whether to accept or reject the trial move, we generate a random number, denoted by Ranf, from a uniform distribution in the interval [0,1]. The probability that Ranf is less than $acc(o \rightarrow n)$ is equal to $acc(o \rightarrow n)$. Therefore, we accept the trial move if $\mathrm{Ranf} < acc(o \rightarrow n)$ and reject it otherwise. This rule guarantees that the probability to accept a trial move from o to n is indeed equal to $acc(o \rightarrow n)$.

Using the Monte Carlo method it is particularly easy to to simulate a system of particles interacting via hard potentials. The same Metropolis procedure is used, except that, in this case, the overlap of two spheres results in an infinite positive energy change and $\exp\{-\beta[\mathcal{U}(n) - \mathcal{U}(o)]\} = 0$. Thus we immediately reject all trial moves involving an overlap since $\exp\{-\beta[\mathcal{U}(n) - \mathcal{U}(o)]\} < \mathrm{Ranf}$. Equally all moves that do not involve overlap are immediately accepted. As in soft potentials, in the case a move is rejected, the old configuration is recounted in the average.

4.3.2 The Molecular Dynamics method

As described in the last section, in a Monte Carlo simulation we compute the average behavior of a system in a purely static sense : *ensemble* average. In most experiments, however, we perform

a series of measurements during a certain time interval and then determine the average of these measurements. The basic idea behind molecular dynamics simulations is precisely that we can study the average behavior of system simply by computing the natural time evolution of that system numerically. After that we average the quantity of interest over a sufficiently long time. The time averaged value of some observable $\mathcal{A}$ is therefore given by

$$\overline{A(r)} = \lim_{t \to \infty} \frac{1}{t} \int_0^t dt' A(r; t') \tag{4.9}$$

"Ergodic hypothesis" states that, if we wish to compute the average of a function of the coordinates and momenta of a many-particle system, we can *either* compute the quantity by time averaging (the "MD" approach) *or* by ensemble averaging (the "MC" approach). The molecular dynamics approach is also useful if we want to look at systems which are driven far from equilibrium where it is hard to define an "ensemble" average. We shall use the MD approach for our studies of the dynamics of liquids and the liquid solid interface in Chapter 6.

A basic molecular dynamics algorithm

- We read in the parameters that specify the conditions of the run (e.g., initial temperature, number of particles, density, time step).

- We initialize the system (i.e., we select initial positions and velocities).

- We compute the forces on all particles.

- We integrate Newton's equations of motion. The step and the previous one make up the core of the simulation. They are repeated until we have computed the time evolution of the system for the desired length of time. To integrate the equations of motion we use the "velocity Verlet" algorithm which is implemented in two stages. Firstly, the new positions at time $t + \Delta t$ are calculated using the equation,

$$r(t + \Delta t) = r(t) + v(t)\Delta t + \frac{f(t)}{2m}\Delta t^2 \tag{4.10}$$

and the velocities at mid step are computed using

$$v(t + \frac{1}{2}\Delta t) = v(t) + \frac{1}{2m}f(t)\Delta t \tag{4.11}$$

The forces and accelerations at time $t + \Delta t$ are then computed, and the velocity move completed

$$v(t + \Delta t) = v(t + \frac{1}{2}\Delta t) + \frac{1}{2m}f(t + \Delta t)\Delta t \tag{4.12}$$

At this point, the kinetic energy at time $t + \Delta t$ is available. The potential energy at this time will have been evaluated in the force loop. Note that if we use the kinetic energy per particle as a measure of the instantaneous temperature, then we would find that, in the canonical ensemble, this temperature fluctuates. To avoid this, we use either simple temperature rescaling or proper heat baths [64].

- After completion of the central loop, we compute and print the averages of measured quantities, and stop.

If we have a system of particles interacting via hard potentials then we have to take a different approach. Whenever two such particles come close enough to reach a point of discontinuity in the potential, then there is a "collision". Therefore, in such a system, the primary aim is to calculate the time, collision partners, and all impact parameters, for every collision occurring in the system. Unlike soft potentials, hard potential programs evolve on a collision-by-collision basis. The general scheme is as follows :

- locate next collision

- move all particles forward until collision occurs

- implement collision dynamics for the colliding pair

- calculate any properties of interest, ready for averaging, before returning to the first step.

Although the above scheme is the basis for simulating hard core systems, the introduction of an external potential renders the simulation technique difficult to implement. This is because in the presence of an external potential the particles will experience a force $\mathbf{f_{ij}}$ and the collision equation that we need to solve is given by

$$|\mathbf{r}_{ij}(t + t_{ij})| = |\mathbf{r}_{ij} + \mathbf{v}_{ij}t_{ij} + (1/2)\mathbf{f}_{ij}t_{ij}^2| = \sigma \qquad (4.13)$$

where $\mathbf{r}_{ij} = \mathbf{r}_i - \mathbf{r}_j$ and $\mathbf{v}_{ij} = \mathbf{v}_i - \mathbf{v}_j$ and σ is the hard core diameter. Therefore we now have a quartic equation in t_{ij} and it is highly non- trivial and time consuming to find the solution. Therefore, to simulate a hard disk system in the presence of an external potential, we use multiple time step molecular dynamics that we use for soft potentials. However, in the position and velocity update scheme, we introduce the additional restriction that if two particles overlap, then they are retained in their old positions but their velocities are interchanged. This of course introduces an error in the simulation procedure but we choose a sufficiently small time scale and benchmark our simulation against standard results for the velocity of sound in hard disk liquid. In our simulations, the unit of time, t, is $\tau = \sqrt{m\sigma^2/k_B T}$, where $m (= 1)$ is the mass of the hard disks. We find that a time step of $\Delta t = 10^{-4}$ conserves the total energy to within 1 in 10^3 (at worst) - 10^6.

4.4 Bulk variables

From computer simulations, we get information at the microscopic level - atomic and molecular positions, velocities, etc. With the help of statistical mechanics we convert this very detailed information into macroscopic terms such as pressure, internal energy, etc. In this chapter, we focus on the determination of bulk quantities which are averaged over the entire system and are meaningful only for homogeneous phases. The analogous space dependent local quantities at interfaces are described and discussed in the next chapter.

4.4.1 Thermodynamic variables

Bulk thermodynamic variables such as density, pressure, stress etc. can be easily calculated. For a system of $\mathcal{N}$ particles in a volume $\mathcal{V}$, in a homogeneous phase the average density is given simply as $\rho = \mathcal{N}/\mathcal{V}$. The pressure may be calculated from the equation ($\langle \cdot \rangle$ denotes the ensemble average)

$$\mathcal{P}\mathcal{V} = \mathcal{N}k_B\mathcal{T} + \langle \mathcal{W} \rangle \tag{4.14}$$

where $\mathcal{W}$ is the 'internal virial' given as

$$\mathcal{W} = \frac{1}{2}\sum_{i=1}^{\mathcal{N}} \mathbf{r}_i \cdot \mathbf{f}_i \tag{4.15}$$

in two-dimensions. $\mathbf{f}_i$ is the force on some particle i. For pairwise interactions, $\sum_i \mathbf{r}_i \cdot \mathbf{f}_i = \sum_i \sum_{j>i} \mathbf{r}_{ij} \cdot \mathbf{f}_i$ where $r_{ij} = r_i - r_j$. We can thus calculate the pressure for various densities. In Figs. 4.1 and 4.2 we plot the equation of states for the soft core and Lennard-Jones liquid in two-dimensions. In both cases, we perform Monte-Carlo simulations in the constant $\mathcal{N}\mathcal{A}\mathcal{T}$ ensemble with $\mathcal{N} = 1200$ and $\mathcal{T} = 1$. The potentials are truncated at $r_c = 2.5$. In our simulations we have used reduced units ($\sigma = \epsilon = m = 1$). The time step of $\delta t = 10^{-3}$ conserves the energy. To compare our simulation results for the soft disk liquid we use the empirical equation of state [62] given as

$$\frac{\beta\Delta\mathcal{P}}{\rho} = 1.77306\rho* + 2.36241\rho*^2 + 1.798198\rho*^3 - 5.648177\rho*^4$$
$$+ 78.65712\rho*^5 - 197.57241\rho*^6 + 212.37417\rho*^7 - 79.57456\rho*^8 \tag{4.16}$$

For the hard disk system the forces are impulsive and one cannot directly use Eqn. 4.15. We however make use of the pair distribution function to calculate the pressure. The pair distribution function is defined in the next section. Thus, the equation of state for the hard disk system is [67]

$$Z \equiv \frac{\beta\mathcal{P}}{\rho} = 1 + 2\eta g(\sigma) \tag{4.17}$$
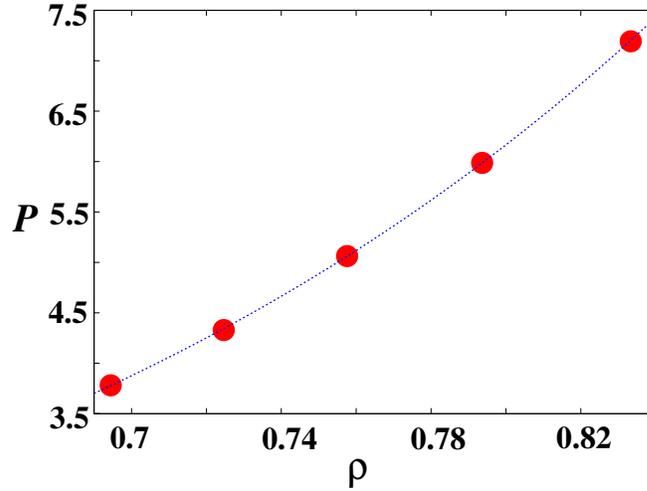
FIGURE 4.1: The equation of state of the soft disk liquid. Symbols are our results, line from [62]
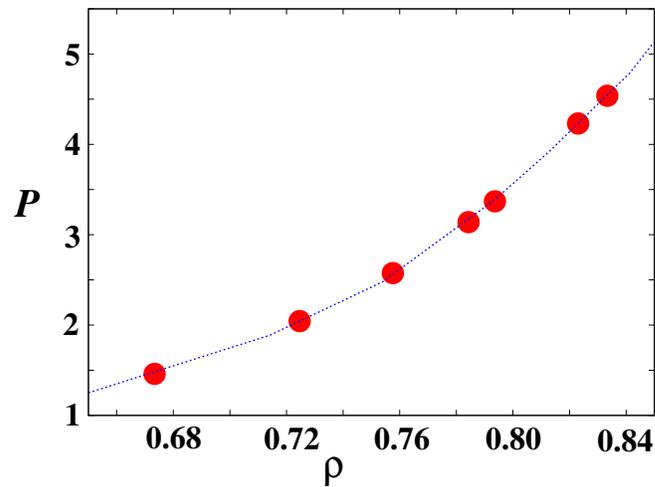
FIGURE 4.2: The equation of state of the Lennard-Jones disk liquid. Symbols are our results, line from [66]

where $g(\sigma)$ is the radial distribution function at $r = \sigma$, the hard disk diameter. We again perform MC simulation in the canonical ensemble with the same number of particles and at the same temperature. We average over 10^4 configurations to obtain the radial distribution functions for various η's and from them derive the corresponding $g(\sigma)$'s. We compare our results with the semi-empirical equation of state given as [69],

$$Z = \left(1 - 2\eta + \frac{2\eta_c - 1}{\eta_c^2}\eta^2\right)^{-1} \tag{4.18}$$
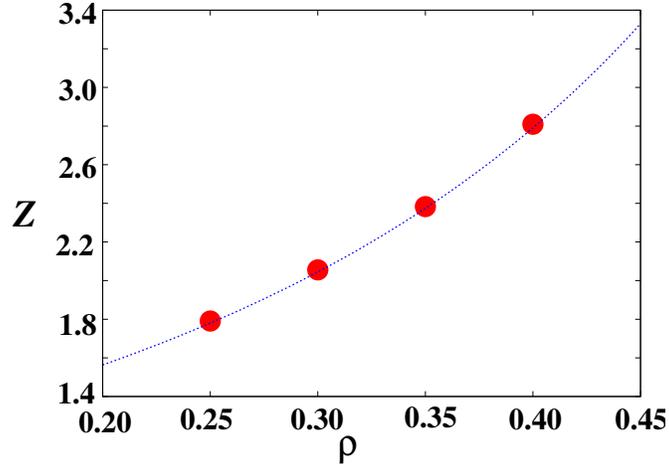
FIGURE 4.3: The equation of state of the hard disk liquid. Symbols are our results, line from [68]

4.4.2 Structural quantities

One important function that characterizes the structure of a homogeneous phase is the pair distribution function $g_2(\mathbf{r}_i, \mathbf{r}_j)$, or $g_2(r_{ij})$ or simply $g(r)$. It is defined as the probability of finding a pair of atoms a distance r apart, relative to the probability expected for a completely random distribution at the same density. A form for $g(r)$ useful for computer simulation purpose is given as

$$g(r) = \rho^{-2}\langle\sum_i\sum_{j\neq i}\delta(\mathbf{r}_i)\delta(\mathbf{r}_j - \mathbf{r})\rangle = \frac{\mathcal{V}}{\mathcal{N}^2}\langle\sum_i\sum_{j\neq i}\delta(\mathbf{r}_j - \mathbf{r})\rangle \tag{4.19}$$

In simulations, the delta function is replaced by a function which is non-zero in a small range of separations, and a histogram is compiled of all pair separations falling within each such range. The pair distribution function is extremely important because we may also express thermodynamic quantities like the energy and the pressure in terms of this function.

One other quantity that is very useful in characterizing the structure of a phase is the structure factor $S(k)$ where k is the wavevector. In a simulation with periodic boundaries, k is restricted by the periodicity of the system, i.e. with the simulation box. The structure factor describes Fourier components of density fluctuations as

$$S(k) = \mathcal{N}^{-1}\langle\rho(k)\rho(-k)\rangle \tag{4.20}$$

where $\rho(k) = \sum_{i=1}^{\mathcal{N}}\exp(i\mathbf{k}\cdot\mathbf{r}_i)$. The structure factor is essentially the Fourier transform of the pair distribution function and is directly measurable in X-ray or neutron diffraction experiments [33].

Apart from these two quantities we may also define the order parameters that distinguish two phases. Here we discuss two such quantities [61] that would be useful to characterize the fluid and solid phases in our analysis of the liquid-solid interface of a two-dimensional system in Chapter 5.

(i) **Bond orientational order parameter** : In a periodic crystal, there is only a discrete set of directions defined by vectors between nearest neighbour particles, which occupy sites on a lattice. These directions are the same throughout the lattice and define a long-range orientational order often called the *bond orientational* order or the *bond-angle* order. The orientational order of a two-dimensional hard disk system can be described by the (global) bond orientational order parameter $\langle \psi_6 \rangle$ where as usual $\langle \cdot \rangle$ denotes ensemble average. The local value of ψ_6 for a particle i located at $\mathbf{r}_i = (x, y)$ is given by

$$\psi_{6,i} = \frac{1}{N_i} \sum_j \exp(6i\theta_{ij}) \qquad (4.21)$$

where the sum on j is over the N_i neighbours of this particle, and θ_{ij} is the angle between the particles i and j and an arbitrary but fixed reference axis. The (global) bond orientational order parameter is then defined as

$$\langle \psi_{6,i} \rangle = \langle | \frac{1}{N} \sum_{i=1}^{N} \psi_{6,i} | \rangle \qquad (4.22)$$

where N is the particle number of the system. For a perfect triangular structure $\psi_6 = 1$. Thus a solid or a hexatic phase will have $\psi_6 \neq 0$. However for the disordered liquid phase ψ_6 will average to zero for $N \to \infty$.

(ii) **Solid order parameter** : In an external field however the bond orientational order may be non-zero even in the fluid phase. This is because, we can now have a "modulated liquid" in which the local hexagons consisting of the six nearest neighbours of a particle are automatically oriented by the external field for example, near the liquid solid interface. Thus ψ_6 is non-zero both in the (modulated) liquid and the crystalline phase and cannot be used to study the freezing transition or liquid solid interface. The order parameters corresponding to the solid phase are the Fourier components of the (nonuniform) density-density correlation $\langle \rho(\mathbf{r}_i) \rho(\mathbf{r}_j) \rangle$ calculated at the reciprocal lattice points $\{\mathbf{G}\}$. This (infinite) set of numbers are all zero (for $\mathbf{G} \neq 0$) in a uniform liquid phase and nonzero in a solid. We restrict ourselves to the star consisting of the six smallest reciprocal lattice vectors of the two dimensional triangular lattice. In modulated liquid phase, the Fourier components corresponding to two out of these six vectors, eg., those in the direction perpendicular to the interface, $\mathbf{G}_1$, are nonzero. The other four components of this set which are equivalent by symmetry ($\mathbf{G}_2$) are zero in the (modulated) liquid and nonzero in the

solid (if there is true long ranged order). Thus, we use the following order parameter :

$$\langle \psi_{\mathbf{G}_k} \rangle = \langle | \sum_{i,j=1}^{N} \exp(-i\mathbf{G}_k \cdot \mathbf{r}_{ij}) | \rangle \qquad (4.23)$$

where $\mathbf{r}_{ij} = \mathbf{r}_i - \mathbf{r}_j$. Note that though the order parameter $\langle \psi_{G_2} \rangle$ decays to zero with increasing system size in the two-dimensional solid - quasi long ranged order - this decay, being weak, does not hinder us from distinguishing, in a finite system, a modulated liquid from the solid phase with positional order.

4.4.3 Dynamic quantities

The important dynamical quantities for our purposes are those which characterize the transfer of mass, momentum and energy across a liquid solid interface. In Chapter 6, we shall study the speed of sound, the sound absorption coefficient and the thermal conductivity of an inhomogeneous system consisting of solid and liquid regions. In this section, we shall show how non-equilibrium molecular dynamics simulations may be used to obtain the sound velocity and the absorption coefficient for a homogeneous hard disk liquid. Consider a rectangular simulation box of length L_x and width L_y. Sound propagation is studied by producing a momentum ($v_y = V_0$) impulse over a thin rectangular region in y spanning the width L_x of the cell. This generates a weak, acoustic, shock [70]. The shock rapidly evolves into a Gaussian pulse which propagates non-linearly with a speed $c_{pulse} \geq c_0(\rho)$, the speed of sound in the liquid which is a function of the density ρ of the hard disk liquid. The deceleration of the pulse follows a pattern which is strongly
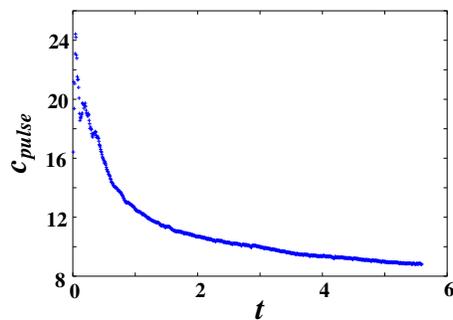
FIGURE 4.4: Speed of propagation of a momentum pulse in the hard disk liquid as a function of time

reminiscent of the propagation of acoustic shock in water after the collapse of a sonoluminiscent bubble. If we fit the time dependent pulse velocity(Fig. 6.2) to a form $c_{pulse}(t) = c_0(\rho) + c_1/t^{\nu}$, we obtain the limiting velocity $c_0(\rho)$ with ν close to 0.5. We now compare the speed of sound

$c_0(\rho)$ with the equation for the speed of sound in a hard disk gas given by [68]

$$c_0 = \sqrt{\frac{2k_BT}{m}\frac{\partial}{\partial\eta}[\eta Z(\eta)]} \tag{4.24}$$

where for $Z(\eta)$ we use the familiar equation of state Eqn. 4.18. We find that the speed of sound measured in this way compares remarkably well with the speed of sound in the hard disk liquid (Fig. 4.5). The calculated $c_0(\rho)$ is of course independent of the initial strength V_0 of the shock. Viscous dissipation spreads the pulse into a smooth Gaussian with a width Δ^2 which, at late
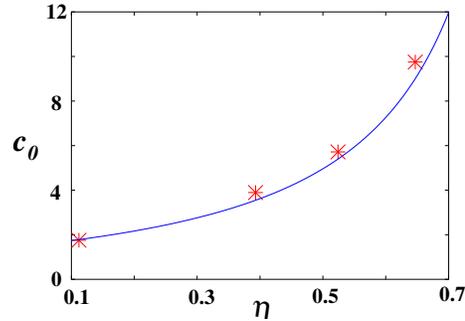
FIGURE 4.5: Extrapolated limiting pulse speed c_0 as a function of the packing fraction, η. The line is a plot of the speed of sound obtained from the equation of state Eqn. 4.24

times, increases linearly with distance s, and the sound absorption [70] coefficient $\alpha = \Delta^2/4c_0^2 s$ is also independent of V_0 (Fig. 4.6). The qth Fourier component of the velocity therefore decays
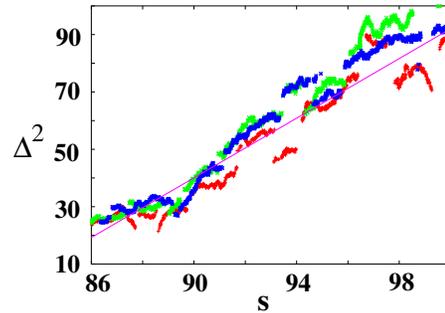
FIGURE 4.6: The absorption coefficient Δ^2 showing the expected linear dependence with distance of propagation s. The different coloured symbols represent different values of the initial momentum shock V_0 red : ...; green : ...., etc.

with s as $v_q(s) = v_q(0)\exp(-\alpha c_0^2 q^2 s)$. In order to obtain a measurable Gaussian we average all quantities over ~ 200 initial velocity configurations chosen from a Maxwellian distribution with temperature $k_BT = 1$.

5 Liquid Solid interfaces : Equilibrium properties

5.1 Introduction and background

In this chapter we shall use the ideas and methods discussed in the last chapter to study interfaces between a liquid and a solid in two dimensions. We shall show that such interfaces may be constructed using external chemical potential fields similar to the simple Ising interface studied in Chapters 2 and 3. Small wavenumber fluctuations, known as crystallization waves, which are dominant in field free liquid solid interfaces are, of course suppressed for reasons similar to the Ising case viz. the explicit breaking of translational invariance of the system perpendicular to the interface. Our interfaces therefore remain planar for the parameters used in our study. However, as we shall see shortly, the planar liquid solid interface is not inert. Particles are transferred across the interface in new and interesting ways. We believe that some of our predictions may be directly checked for liquid solid interfaces in atomic, as well as, colloidal systems where the chemical potential field may be provided either by a laser trap or by adsorbing colloidal particles on a patterned substrate. In the next chapter we shall discover how these interfacial fluctuations influence transport properties of the interface contributing to the resistance offered to the transfer of momentum impulses and of heat.

A liquid is homogeneous and isotropic. The local density $\rho(\mathbf{r})$ is independent of the spatial coordinate $\mathbf{r}$ and has Fourier components which are nonzero only for the $q = 0$ mode. This translational invariance is partially broken in the solid which has Fourier components $\rho_{\mathbf{G}}$ which are nonzero for all wavevectors $\mathbf{G}$ which are members of the reciprocal lattice vector set of the solid. The solid can therefore be described completely using the countably infinite number of Fourier components $\rho_{\mathbf{G}}$. Across a liquid solid interface all the order parameters are expected to go from zero to their value in a solid (close to unity) within a region of width ξ, the interfacial thickness. While, the structure of real liquid-solid interfaces is difficult to determine experimentally in molecular detail, the interface is expected to be sharp with the order parameters building up within a few atomic layers. This is simply a reflection of the fact that the freezing transition is sharply first order in three dimensions [71] with a finite correlation length. Also most liquid solid interfaces are not planar. The finiteness of heat and mass transport coefficients at the

interface generates instabilities, first analyzed by Mullins and Sekerka [6, 72], which grow into non-compact dendritic structures typically observed in most real situations. There has, however, been a number of theoretical and computer simulation studies starting from the pioneering work of Haymet and Oxtoby [73, 74]. Most of these studies refer to a planar interface.

In the next section we shall introduce the local analogs of the thermodynamic and structural quantities introduced in the earlier chapter. All of these quantities will have different values on either side of a liquid solid interface and will be used to define the interface. Next we shall show how non uniform chemical potential fields may be used to generate liquid solid interfaces and shall try to make contact with experiments by calculating approximately the parameters required for constructing a suitable laser trap. We shall plot local thermodynamic and orderparameters to characterize the interface. Our main result of this chapter, namely the existence of complete layer transfers will then be presented for three different systems viz. the hard disk, soft disk and Lennard-Jones system. We shall attempt to understand our result from thermodynamic arguments, for the simplest of the three systems, namely hard disks.

5.2 The liquid solid interface

In this section, we explore the possibility of creating a patterned sequence of confined solid and liquid regions using an external, space-dependent, chemical potential field $\phi(\mathbf{r})$. Consider a two dimensional system (see Fig 5.1) of N atoms of average density (packing fraction) $\eta = \pi N/4A$ within a rectangular cell of size $A = L_x \times L_y$ where the central region $\mathcal{S}$ of area $A_s = L_x \times L_s$ is occupied by N_s atoms arranged as a crystalline solid of density $\eta_s > \eta$, while the rest of the cell is filled with liquid of density $\eta_l < \eta$. The difference in density is produced by an external
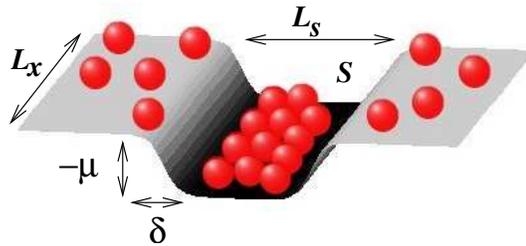
FIGURE 5.1: A cartoon diagram of the system

field $\phi(\mathbf{r}) = -\mu$ for $\mathbf{r} \in \mathcal{S}$; increasing sharply but smoothly to zero elsewhere with a hyperbolic tangent profile of width δ_ϕ. How may $\phi(\mathbf{r})$ be realized in practice? In model solids like colloids [75], one may use a surface template to create a static pattern [76]. In real systems, as well as colloids [77], one may be able to use laser traps [78] or non -uniform electric or magnetic fields.

Usual laser traps for alkali metals or rare gas atoms are in the range of $10mK$ for which a power of about $100mW$ is required.

For specificity and simplicity we first choose the atoms to interact with a *hard disk* potential [79] although we show towards the end of this chapter that qualitative results for more realistic potentials, e.g., soft sphere or Lennard-Jones are the same. We have chosen $\delta_\phi = \sigma/4$, where σ is the hard disk diameter and sets the scale of length. The energy scale for this system is set by $k_B\mathcal{T}$ where k_B is the Boltzmann constant and $\mathcal{T}$ the temperature. In our simulation we set $\sigma = k_B\mathcal{T} = 1$. Most of the qualitative phenomena discussed subsequently are independent of the exact nature of the interactions.

The full configuration dependent Hamiltonian is $\mathcal{H} = \sum_{ij} V_{ij} + \sum_i \phi(\mathbf{r}_i)$. We have carried out extensive MC simulations with usual Metropolis moves [64], periodic boundary conditions in both directions and in the constant number, area and temperature ensemble to obtain the equilibrium behaviour of this system for different μ at fixed η. $N = 1200$ particles occupy an area $A = 22.78 \times 59.18$ with the solid occupying the central third of the cell of size $L_s = 19.73$ The initial configuration is chosen to be a liquid with $\eta = .699$; close to but slightly lower than the freezing [79] density $\eta_f = .706$. On equilibration, $\mathcal{S}$ contains a solid with the closest -packed planes parallel to the solid -liquid interfaces which lie, at all times, along the lines where $\phi(y) \to 0$. The equilibration time is large and many ($\sim 10^7$) Monte Carlo steps (MCS) are discarded before results shown in Figs. 5.2 and 5.3 are obtained.

5.3 Local averages

Since in this chapter we study a liquid solid interface, thermodynamic and structural quantities which are averaged over the entire system makes no sense. We have to, therefore, construct local analogs of these quantities as discussed in Chapter 4. To this purpose, we divide the simulation box into thin rectangular strips with the longer dimension parallel to the interface. Each of these strips are indexed by an integer i which runs from 1 to M, the total number of strips. We shall see that the external potential induces a solid which has a layered structure. Therefore, it is important that while breaking the system up into strips of equal width, the edge of the strips in the solid region always falls between two layers. The index i multiplied by the width of the strip gives the distance in the direction perpendicular to the interface.

The thermodynamic quantities may always be defined as intensive variables containing sums over all the particles of the system divided by the total number of particles. In this case the sums run only over the particles in a strip. Thus for example,

$$\rho_i = \frac{Number\ of\ particles\ in\ strip\ i}{Strip\ width} \tag{5.1}$$

where ρ_i is the local density in strip i, and similarly for other quantities.
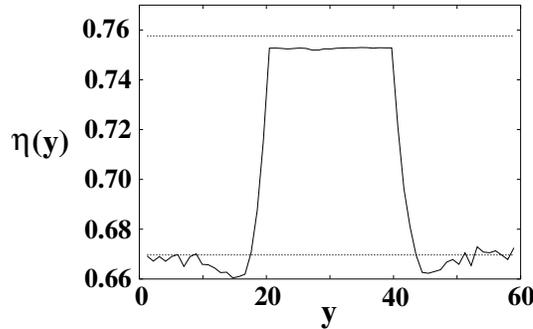
FIGURE 5.2: The density profile $\eta(y)$ coarse grained over strips of width σ (averages taken over 10^3 MC configurations each separated by 10^3 MCS), varies from η_ℓ to η_s as we move into $\mathcal{S}$. The lines show the predictions from a simple thermodynamic theory presented in Section 5.5.1

Structural quantities are typically sums over pairs of particles. Here, we take one of the particles within the strip while its companion lies either in the same strip or in neighbouring strips. The orientational order parameter is calculated in each strip and is averaged over equilibrium configurations. To calculate the local solid order however, we choose area within the solid region and count the number of particles in this area. We then find out the solid order parameter for these particles as a function of the length perpendicular to the interface. We use the same trick for the liquid region and finally merge the two at the interface to get the variation of the solid order parameter for the entire system in the direction perpendicular to the interface. Just as for the orientational order parameter, averaging is done over equilibrium configurations.

In all these definitions, we have of course assumed that there is no systematic variation of any of the quantities in the direction parallel to the interface, in accordance with the symmetry of the problem.

5.4 Order parameter profiles and structure factor

In this section we present all results for the local thermodynamic and structural quantities calculated as above. The density $\eta(y)$ coarse grained over strips of width $\sim \sigma$ varies from its value η_l in the liquid to η_s as we move into (and away from) $\mathcal{S}$ (Fig. 5.2). Averages taken over 10^3 MC configurations each separated by 10^3 MC steps. The trap depth $\mu = 6$, supports an equilibrium solid of density $\eta_s = .753$ in contact with a fluid of density $\eta_\ell = .672$. The horizontal lines are predictions of a simple free-volume based theory (discussed in later sections) for η_s and η_ℓ. A superposition of atomic positions shows a static, flat, liquid solid interface with the solid like order gradually vanishing into the liquid (Fig. 5.3). We have thus created a thin nano-sized crystal which is about 21 atomic layers wide (for a trap depth, $\mu = 6$) and is flanked on either

side by liquid separated by two liquid solid interfaces.
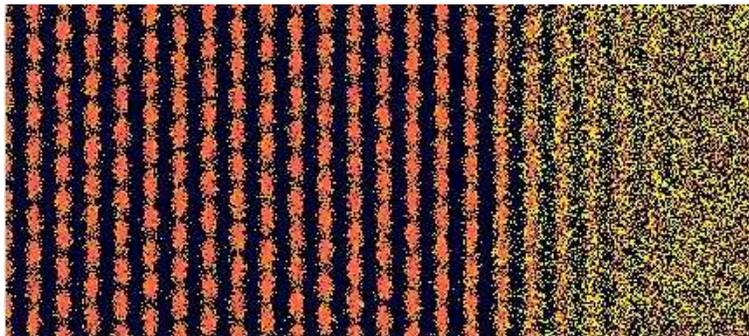
FIGURE 5.3: Superposition of particle configurations from the MC run showing a solid like order (red : high η) gradually vanishing into the fluid (yellow : low η) across a well defined solid-fluid interface.

The bond orientational order parameter $\langle \psi_6(y) \rangle$ coarse grained over strips of width σ (averages taken over 10^3 MC configurations each separated by 10^3 MCS) shows a sharp rise from zero to a value close to one, as we move into the region $\mathcal{S}$. This indicates that the particles in this region are arranged approximately hexagonally. However, this does not necessarily justify the phase to be a solid. Therefore, the need to calculate the solid order parameter. The solid order parameter $\langle \psi_\mathbf{G} \rangle$ in the direction $\mathbf{G}_2$ and the other equivalent to it by symmetry is nonzero in the region $\mathcal{S}$, (Fig. 5.5)indicating without doubt the nucleation of a solid phase. Note that $\langle \psi_6 \rangle$ shows a larger interfacial region than that obtained from $\langle \psi_{\mathbf{G}_2} \rangle$. This is because the liquid near the liquid solid interface is highly orientationally ordered.

The two-dimensional structure factor shows sharp Bragg peaks for the solid region and isotropic pattern for the liquid (Fig. 5.6). Although the structure factor for the solid shows well defined
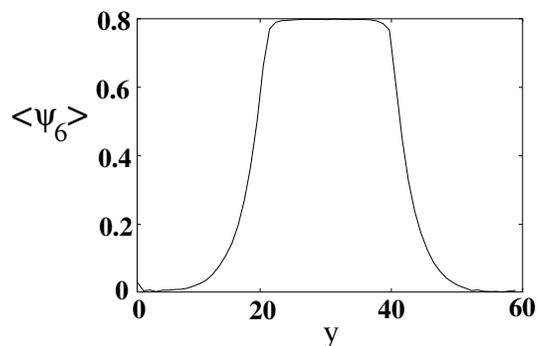
FIGURE 5.4: Bond orientational order parameter across the liquid solid interface for a 21 layered solid surrounded by liquid on both sides.
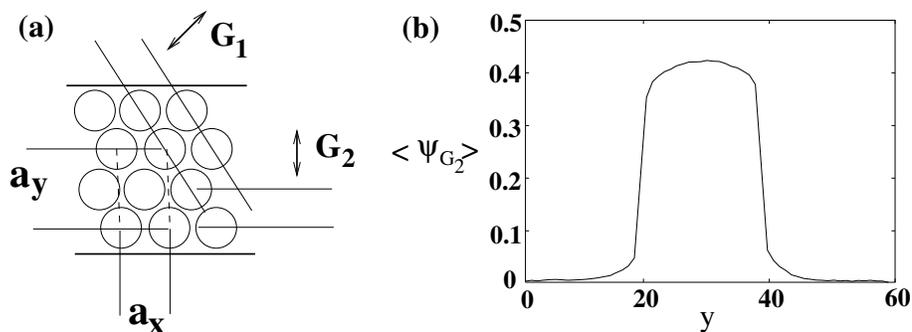
FIGURE 5.5: (a)The reciprocal lattice vectors $\mathbf{G}_1$ and $\mathbf{G}_2$, and the rectangular unit cell. (b) Solid order parameter corresponding to $\mathbf{G}_2$, is nonzero in the region $\mathcal{S}$, indicating a solid

peaks with six-fold symmetry of the triangular lattice, the quasi-onedimensional nature of our system implies that true solid -like order may not be present. However, we do not pursue this question in detail in this thesis. In the interfacial region the peaks are seen to be diffuse indicating once more that the interfacial region is highly orientationally ordered.
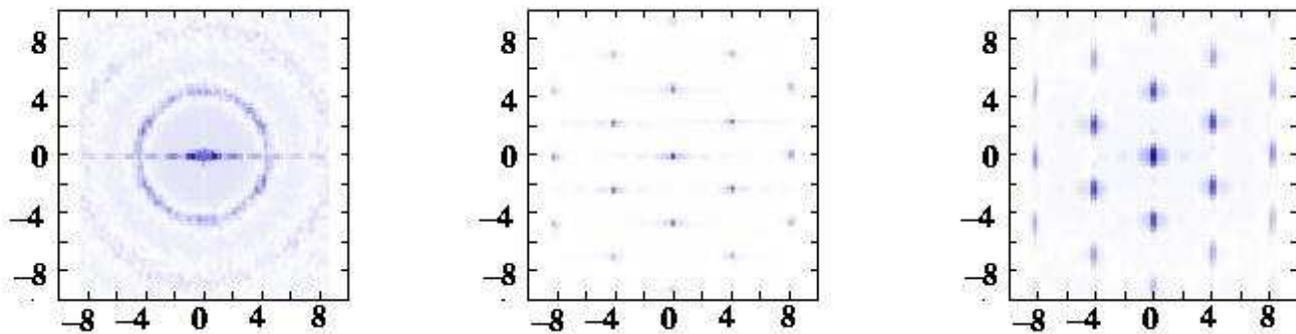
FIGURE 5.6: Two-dimensional structure factor for the liquid, solid and interfacial regions respectively.

5.5 The layering transition

We now calculate the difference in densities between the solid and liquid regions $\Delta\eta = (\eta_s - \eta_l)$ as a function of the strength of the external field μ. While $\Delta\eta/\eta$ increases with increasing μ as expected, the smooth increase is punctuated by a sharp jump (Fig. 5.7). An examination of the particle configuration shows that the jump occurs when an extra close -packed layer enters $\mathcal{S}$ increasing the number of solid layers by one. For the parameters in our simulation, the jump
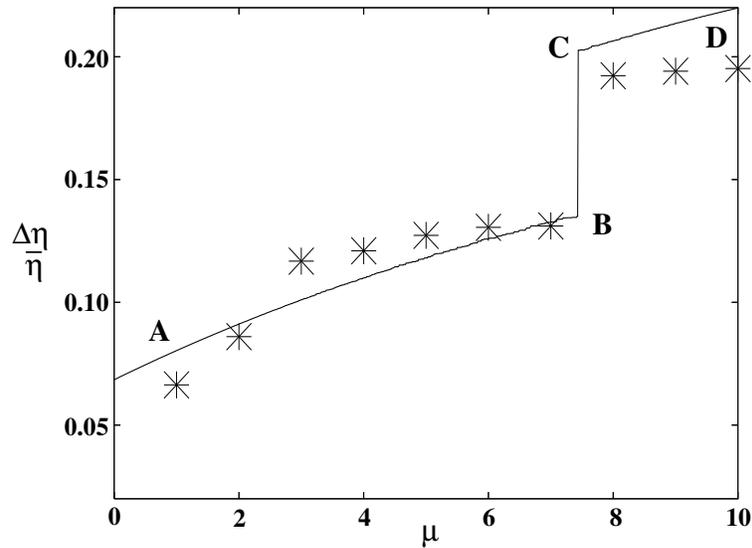
FIGURE 5.7: Plot of the equilibrium fractional density change $\Delta\eta/\eta$ as a function of μ (points (MC data), thick solid line (approximate theory)), showing discontinuous jump at $\mu \approx 8$.

occurs at $\mu \approx 8$ with the number of layers increasing from 21 to 22. The value of μ at the jump is a strong function of L_s. The solid structure is seen to be a defect free triangular lattice with a small rectangular distortion $\varepsilon_d(\eta_s, L_s)$ [80]. We have examined the variation of $\Delta\eta(\mu)/\eta$ by cycling μ adiabatically around the region of the jump. This yields a prominent hysteresis loop as shown in Fig. 5.8 which indicates that 'surface' steps (dislocation pairs) nucleated in the
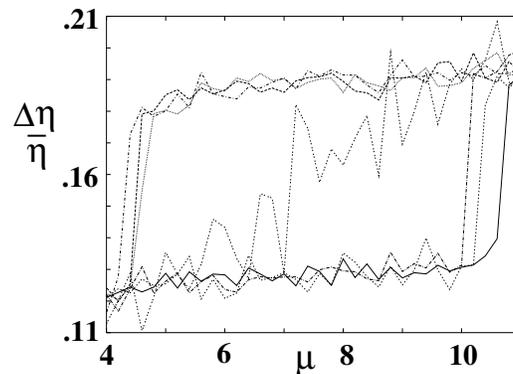
FIGURE 5.8: Cycle-averaged hysteresis loop as μ is cycled at the rate of .2 per 10^6 MCS. The central jagged line is the result of the initial cycle when a single dislocation pair was present in the central solid region.

course of adding (or subtracting) a solid layer, have a vanishingly short lifetime. Consistent with

this we find that the jump in $\Delta\eta(\mu)/\eta$ vanishes when the system is minimised at each μ with a constraint that the solid contains a single dislocation pair (Fig. 5.8). Interestingly, a dislocation pair forced initially into the bulk, rises to the solid-fluid interface due to a gain in strain energy [81], where they form surface indentations flanked by kink-antikink pairs. This costs energy due to the confining potential, as a result, the kink-antikink pair gets quickly annealed by incorporating particles from the adjacent fluid. The jump in $\Delta\eta(\mu)/\eta$ is also seen to decrease with increasing δ_ϕ.

5.5.1 The thermodynamic theory

The qualitative features of these results may be obtained by a simple thermodynamic theory (Fig. 5.7) with harmonic distortions of the solid, ignoring contributions from spatial variations of the density. thermodynamic theory. We first write down the free energy densities of the bulk fluid and solid phases.

Free energy of the solid

For a solid which is only a few atomic layers wide, it is impossible to separate surface and bulk contributions to the free energy. We therefore assume that the dominant effect of confinement of the solid is the introduction of an uniform strain ε_d to be calculated from a reference triangular lattice with the same number of atomic layers [80]. Therefore, we have two terms in the free energy of the bulk solid.

(i)**Free volume part** : In a given solid lattice, the particles have a bulk mean particle distance a_0 which is the distance between nearest neighbours of the lattice. We consider the particles to be confined in independent Wigner-Seitz (or Voronoi) cells of the solid. The cell has a volume $V_b = g_b a_0^D$ where g_b is a geometrical prefactor that depends on the lattice type and on dimensionality D. Each center-of-mass coordinate of the hard disks can move within a free volume of

$$V_{bf} = g_b(a_0 - \sigma)^2 \tag{5.2}$$

without touching the neighbouring disks. Hence, one obtains a lower bound for the bulk partition function, $Q \geq (V_{bf}/\Lambda^2)^{\mathcal{N}}$ which provides an upper bound to the bulk free energy density (free volume contribution)

$$f_\Delta \leq -\mathcal{N}k_B\mathcal{T}\ln\left(\frac{g_b(a_0 - \sigma)^2}{\Lambda^2}\right) \tag{5.3}$$

The upper bound becomes asymptotically exact for close packing. In our calculation for the two-dimensional hard disk solid we calculate $g_b = 1/(0.5231\sigma)^2$ and $a_0 = \sigma\sqrt{\pi/(2\sqrt{3}\eta_s)}$.

(ii)**Elastic contribution** : In order that the solid channel accommodates n_l layers of a homogeneous triangular lattice with lattice parameter a_0 of hard disks of diameter σ, we need

$$L_s = \frac{\sqrt{3}}{2}(n_l - 1)a_0 + \sigma \tag{5.4}$$

Defining

$$\chi(\eta_s, L_s) = 1 + \frac{2(L_s - \sigma)}{\sqrt{3}a_0} \tag{5.5}$$

Eqn. 5.4 then implies $\chi = integer = n_l$ and violation of Eqn. 5.4 implies a rectangular strain away from the reference triangular lattice of n_l layers. The lattice parameters of a centered rectangular lattice (CR) unit cell are a_x and a_y (Fig. 5.5). In general, for a CR lattice with given L_s we have $a_y = 2(L_s - \sigma)/(n_l - 1)$ and, $a_x = 2/\rho a_y$. The normal strain $\varepsilon_d = \varepsilon_{xx} - \varepsilon_{yy}$ is then,

$$\varepsilon_d = \frac{n_l - 1}{\chi - 1} - \frac{\chi - 1}{n_l - 1}, \tag{5.6}$$

where the number of layers n_l is the nearest integer to χ so that ε_d has a discontinuity at half-integral values of χ. For large L_s, this discontinuity and ε_d itself vanishes as $1/L_s$ for all η_s. We therefore have an elastic contribution of $(1/2)K_\Delta \varepsilon_d^2$ in the free energy of the solid.

Incorporating these two factors we may write down the free energy density of the solid phase as

$$f_s = f_\Delta + \frac{1}{2}K_\Delta \varepsilon_d^2, \tag{5.7}$$

where K_Δ is the Young's modulus of an undistorted triangular lattice.

Free energy of the liquid

The free energy density of the liquid bulk phase may be simply written as

$$f_l = \int_0^{\eta_l} d\eta_l' \frac{P/\rho_l - 1}{\eta_l'} + f_{id} \tag{5.8}$$

where the ideal gas Helmholtz free energy per particle $f_{id} = \ln(\rho) - 1$ and we use the semiemperical equation of state for the hard disk liquid [69] given by Eqn. 4.18

Free energy of the system

We now write down the total free energy density of the system (fluid + solid regions) using the free energy density expressions for solid and liquid bulk phases as

$$f = x\left[f_s(\eta_s, L_s) - 4\eta_s\mu/\pi\right] + (1 - x)f_l(\eta_\ell) \tag{5.9}$$

We then minimise this free energy density with the constraint that the average density is fixed, $\eta = x\eta_s + (1-x)\eta_\ell$, where x is the area fraction occupied by $\mathcal{S}$. The result of this calculation is shown in Fig. 5.7 where it is seen to reproduce the jump in $\Delta\eta(\mu)/\eta$.

Why does the solid incorporate layers of atoms from the liquid ? This question may be answered elegantly if one calculates the uniaxial stress in the solid region as a function of the depth of the strain, ε_d. The stress may in fact be obtained in a straight forward fashion from the expression of the free energy. Differentiating the free energy of the solid w.r.t. ε_d we obtain

$$\gamma_d = \frac{\partial f_s}{\partial \varepsilon_d} \tag{5.10}$$

When γ_d is plotted versus the uniaxial strain ε_d, we observe that the solid is not stress free for any arbitrary value of a combination of μ and L_s. In fact, for our parameters, initially the 21 layered solid is under tension. We follow the variation of the tensile stress with the strain as μ is increased from the points $A - D$ in the Fig. 5.9. The state of stress in the solid jumps discontinuously
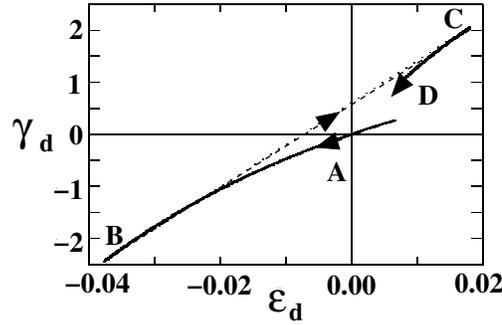
FIGURE 5.9: A plot of the tensile stress γ_d against strain ε_d. The arrows show the behaviour of these quantities as μ is increased from the points marked A – D.

from tensile to compressive from $B \rightarrow C$ due to an increase in the number of solid layers by one accomplished by incorporating particles from the fluid. This transition is reversible and the system relaxes from a state of compression to tension by ejecting this layer as μ is decreased. As μ is increased, the tension increases till it reaches about -2.45 when the corresponding strain is about -0.038. At this point a layer enters the solid region and the stress and strain switches from tensile to compressive. Further increase in μ will now decrease the stress and drive the solid to a state of zero stress. Thus, the layering transition from 21 to 22 layers as observed by us is a mechanism for relieving stress.

Solids subject to large uniaxial deformations, relieve stress either by the generation and mobility of dislocations [47] and/or by the nucleation and growth of cracks [47, 82]. What is the nature of stress relaxation when conditions are arranged such that these conventional mechanisms are suppressed ? Nano-indentation experiments [83, 84] show that if small system size prevents the
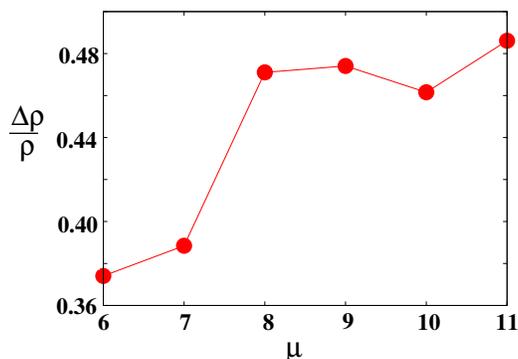
FIGURE 5.10: Plot of the equilibrium fractional density change $\Delta\rho/\rho$ as a function of μ (points (MC data) for soft core; line denotes approximate fit

generation of dislocations [80], solids respond to tensile forces by shedding atoms from the surface layer. What we have shown here using extensive computer simulations and theory, is that a small crystal trapped within a potential well [85] and in contact with its own fluid, a situation easily realised using optical traps, responds to large compressive stresses by a novel mechanism — the transfer of complete lattice layers across the fluid solid interface. In Chapter 6, we study the importance of this "layering" transition by looking at momentum and heat transport across the liquid solid interface and the role this transition plays on transport properties.

5.5.2 Layering in other potentials

If the layering transition observed in the hard disk system is actually a new mechanism for relieving stress in a thin crystal, it should be independent of the details of the potential. Our main results trivially extend to particles interacting with any form of repulsive potential, or even when the interactions are augmented by a short range attraction, provided we choose μ deeper than the depth of the attractive potential. In this section we show explicitly that the layering transition is present in the soft core and Lennard-Jones system. Once again we perform MC simulations in the constant $\mathcal{NAT}$ ensemble with periodic boundary conditions and with the external chemical potential μ. The relevant parameters corresponding to these potentials, namely ϵ and σ in Eqn. 4.4 and Eqn. 4.5, set the energy scale and the length scale respectively. In our simulation $\epsilon = \sigma = 1$ and $\mathcal{N} = 1200$ particles occupy an area $\mathcal{A} = 24 \times 60$ with the solid occupying the central third of the cell of size $L_s = 20$. The average density of the system is therefore $\rho = 0.833$ to be compared with the freezing density of $\rho \sim 1.0$ and $\rho \sim 1.0$ for the soft core and Lennard-Jones systems at this temperature.For the soft core potential, the μ value at the jump in density (Fig. 5.10) is even quantitatively comparable to the corresponding hard core system.
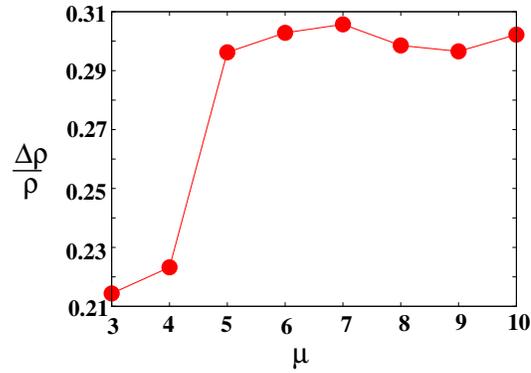
FIGURE 5.11: Plot of the equilibrium fractional density change $\Delta\rho/\rho$ as a function of μ (points (MC data) for Lennard-Jones system; line denotes approximate fit

In the LJ system the jump happens earlier as expected due to the cohesive energy, e_{coh} of the LJ atoms (Fig. 5.11). We estimate, $\mu' = \mu_{HD} - e_{coh}$, where μ_{HD} is the jump potential for the hard disk. Thus $e_{coh} \approx -3.5$. The shift of the layering transition may be used to obtain the cohesive energy of the trapped solid.

6 Liquid solid interfaces : Dynamical properties

6.1 Introduction

In the last chapter, we showed how one might produce a liquid solid interface using a non-uniform external potential. We characterized this interface using a variety of thermodynamic and structural quantities, which were measured as a function of the perpendicular distance from the interface. Finally, we showed that as a function of the depth of the potential well, the trapped solid undergoes, what we called, "layering" transitions which involved the addition (or removal) of an entire layer of solid from or into the surrounding liquid through the interface. The layering transition was accompanied by a sharp jump in the density of the solid. We showed that this layering transition is a novel mechanism by which a stressed nano-solid constrained by an external potential can respond plastically to large stresses *without* nucleating dislocations. Finally, we established that this phenomenon is general and is independent of the particular interatomic potential used.

In this final chapter of the thesis we shall explore how mass, momentum and energy is transported across the liquid solid interface and especially the role of the layering transition on the transport coefficients. We shall show in this chapter that (1) fluctuations associated with this transitions are of a special kind always involving the transfer of complete layers of solid (2) these fluctuations offer resistance to the transfer of momentum and energy through the interface (3) the resistance is maximum when the energy matches that required to raise a complete lattice layer from within the potential well into the surrounding liquid. In the next section we shall begin by studying the stability of surface kinks at the liquid solid interface in the hard disk system. We shall then study the response of the interface to weak acoustic shocks. In the last section we shall use non-equilibrium molecular dynamics to study heat transport through the liquid solid interface in soft disks and obtain the contact or Kapitza resistance of the interface as a function of the depth of the potential well.

In our investigations, to be reported in this chapter we shall exclusively use molecular dynamics simulations since we shall be interested in dynamical quantities.

6.2 Kinetics of layering

The large hysteresis loops associated with the layering transition obtained in Chapter 5 makes it clear that the kinetics of this transition is slow. To study the lifetime of the kink-antikink pairs (surface step), we resort to a MD simulation.

Starting with an equilibrium configuration for the hard disk system, taken from our Monte Carlo runs as discussed in the last chapter (Section 5.2) at $\mu = 9.6$ corresponding to a 22-layer solid, we create a unit surface step of length l by displacing a few interfacial atoms from the solid region into the liquid and 'quench' across the transition to $\mu = 4.8$, where a 21-layer solid is stable. The rest of the parameters are kept identical to those given in chapter 5. We observe that the fluctuation thus created rapidly relaxes back and the surface step vanishes as the atoms are pulled back into the solid. We illustrate this by plotting the number of hard disks within the solid region as a function of the MD time steps (Fig. 6.1). As soon as a step is created, the
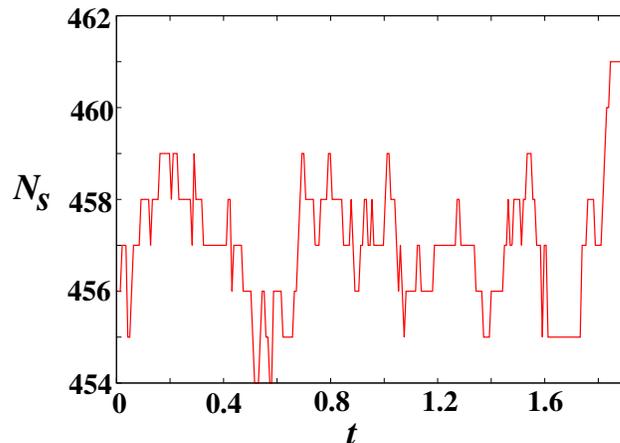
FIGURE 6.1: Plot of the number of particles in the solid region ($\mathcal{N}_s$) as a function of time t clearly shows that the displaced particles are pushed back into the region.

line of atoms in the portion of the solid thus exposed bend to fill up the gap created between the atomic layers and the edge of the potential trap. This generates considerable local elastic stress. Also, the liquid layer lying immediately adjacent to the solid has a lot of orientational and solid-like order. For short times it responds elastically to the presence of an increased local density of atoms. The combined elastic response therefore pushes the displaced atoms back into the solid region thereby annihilating the step. Indeed, a free energy audit involving a bulk free energy gain $\Delta F \sim 1/L_s$, going from a 22 to 21 layered solid, and an elastic energy cost $\sim \log(l)$ for creating a step of size l, reveals that a surface step is stable only if $l \geq l^* \sim 1/L_s$. For small L_s, the critical size l^* may therefore exceed L_x, the total length of the interface. Of course, if

the step spans the entire length of the interface, there is no bending of the atomic lines and there is no elastic energy cost. This explains the slow kinetics since the system has to wait till a rare random fluctuation, which displaces all the atoms in a solid layer across the interface coherently, is required for the layer transition to occur. Although we have explicitly demonstrated this for the hard disk system, we believe that similar considerations should be appropriate for the soft disk and Lennard Jones systems too.

The slow kinetics of the layering transition may have an impact on the transfer of momentum across the liquid solid interface in the form of regular sound waves or acoustic shocks. The large effective compressibility of the solid at the layering transition as evidenced by the jump in the density as the chemical potential is increased by an infinitesimal amount (Fig. 5.7) should reduce the velocity of sound considerably. The propagation and scattering of sound in an inhomogeneous region with coexisting phases has been studied extensively [70, 86–88] in the past. The transfer of mass between coexisting phases at inter-phase boundaries is known to slow down and dissipate sound waves traveling through the system. Our system has an artificially created inhomogeneity, which should have a similar effect on its acoustic properties.

Further, the mechanism of stress relaxation of a thin (L_s small) solid via the transfer of an entire layer of atoms may be exploited for a variety of practical applications. Provided we can eject this layer of atoms deep into the adjoining fluid and enhance its lifetime we may be able to use the ejected layer of atoms to create monolayer atomic films or coatings. Highly stressed mono-atomic layers tend to disintegrate or curl up [89] as they separate off from the parent crystal. It may be possible to bypass this eventuality, if the time scale of separation is made much smaller than the lifetime of the layer. Can acoustic spallation [90] be used to cleave atomic layers from a metastable, stressed nanocrystal?

In the next section, therefore, we study the response of the liquid solid interface in our system of hard disks to acoustic shocks with a view to studying the effect of the layering transition on acoustic shock propagation and dissipation.

6.3 Effect of shock wave

Imagine, therefore, sending in a sharp laser (or ultrasonic) pulse, producing a momentum impulse ($v_y(t = 0) = V_0$) over a thin region in y spanning the length L_x of the simulation cell, which results in a weak acoustic shock [90] (corresponding to a laser power $\approx 10^2$ mW and a pulse duration 1ps for a typical atomic system). The initial momentum pulse travels through the solid and emerges at the far end (Fig. 6.2) as a broadened Gaussian whose width, Δ, is a measure of absorption of the acoustic energy of the pulse due to combined dissipation in the liquid, the solid and at the interfaces [70, 86, 91]. For large enough pulse strengths V_0, this is accompanied by
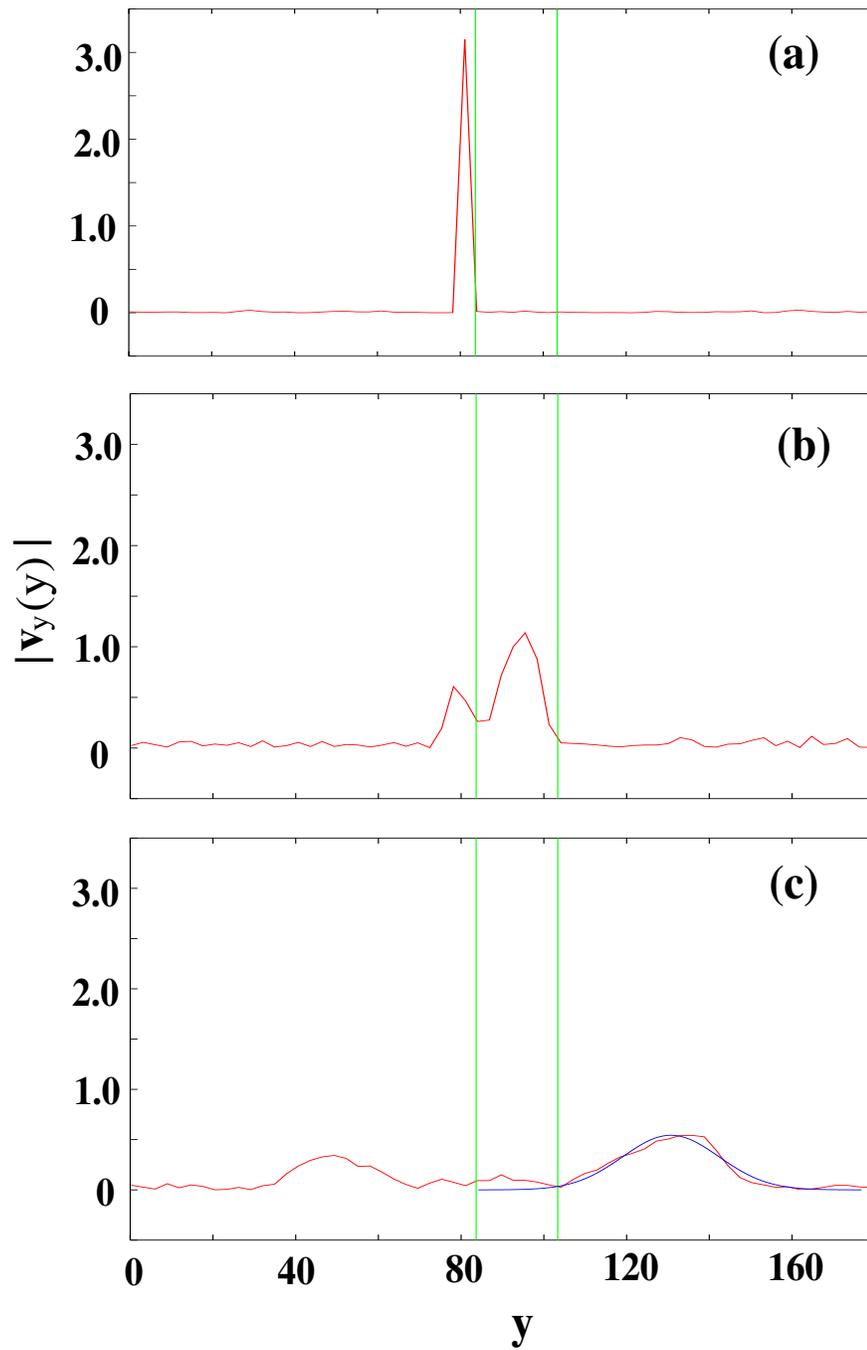
FIGURE 6.2: (a)-(c) Plot of the absolute value of the momentum $|v_y(y)|$ for molecular dynamics times $t = .0007$ (a), $.2828$ (b) and 2.8284 (c). The green lines show the position of the solid -fluid interfaces. The fit to a Gaussian (blue line) is also shown in (c). Curves such as in (a)-(c) are obtained by averaging over $100 - 300$ separate runs using different realizations of the initial momentum distribution.

a *coherent ejection of the (single) outer layer of atoms into the fluid*. Note that in our MD simulations, to reduce interference from the reflected pulse through periodic boundary conditions, we increase the fluid regions on either side, so that for the MD calculations we have a cell of size 22.78×186.98 comprising 3600 particles. In Fig. 6.2 the initial momentum pulse with strength $V_0 = 6.$ is given within a narrow strip of size $\sim \sigma$, just to the left of the solid region and the curves are fitted to a Gaussian (and the width Δ^2 extracted) when the maximum of the pulse reaches a fixed distance of 44.1 from the source. A reflected pulse can also be seen.

When a shock wave, which propagates through a conventional solid emerges from the free surface, the compressed material expands to zero pressure [90]. The unloading (rarefaction) wave travels backwards into the material with the speed of sound. The response of the solid now depends on the specific nature of the shock front. For a shock wave with an approximately Gaussian profile as in our case, significant negative pressures can develop at the interface where the shock emerges due to the interaction of the forward and the reflected waves and a portion of the solid may split off by a process known as "spallation". Spallation in bulk solids like steel
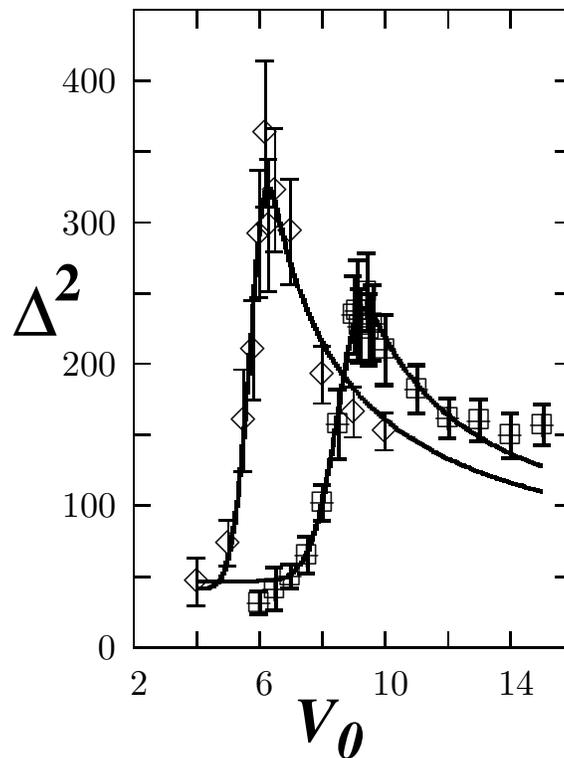
FIGURE 6.3: Plot of the squared width Δ^2 of the momentum pulse after it emerges from the solid as a function of V_0 for $\mu = 4.8\,(\Diamond)$ and $9.6\,(\Box)$. The solid line is a guide to the eye. The peak in $\Delta^2(V_0)$ so produced is more prominent for the metastable 22 layered solid $\mu = 4.8$ than for the stable $(\mu = 9.6)$ system showing a more coherent momentum transfer in the former case.

needs acoustic pressures in excess of 10^5 N/cm^2 [90] usually available only during impulsive loading conditions; the ejected layer is a "chunk" of the surface. In contrast, the pressures generated by the shock wave in our system causing coherent *nanospallation* involves surface stresses of the order $k_B T/\sigma^2 \approx 10^{-5}$ N/cm^2, and are therefore much lower. This difference comes about because unlike a bulk system, a strained nanocrystal on the verge of a transition from a metastable $n+1$ to a n layered state readily absorbs kinetic energy from the pulse. The fact that surface indentations are unstable (Fig. 6.4) unless of a size comparable to the length of the crystal, L_x, ensures that a full atomic layer is evicted almost always, leading to coherent absorption of the pulse energy. The coherence of this absorption mechanism is markedly evident in a plot of Δ^2 against V_0 which shows a sharp peak (Fig. 6.3). Among the two systems studied by us, *viz.*, a metastable ($\mu = 4.8$) and a stable ($\mu = 9.6$) 22 layered solid, the former shows a sharper resonance. Note that the absorption of momentum is largest when the available kinetic energy of the pulse exactly matches the potential energy required to eject a layer. To elucidate this fact further, we plot the configurations of the metastable system ($\mu = 4.8$) as the pulse travels through the system, for two different pulse strengths, $V_0 = 2$ and $V_0 = 6$ (Fig. 6.4). The weaker momentum pulse ($V_0 = 2$) initially ejects a few atoms of the interfacial crystalline layer of the metastable 22 layered solid. However, the resulting large non-uniform elastic strain evidenced by the bending of lattice layers causes these atoms to be subsequently pulled back into the solid. This effect is the same as that seen in Section 6.2. Only a stronger pulse, $V_0 = 6$, capable of ejecting a complete lattice layer succeeds in reducing the number of solid layers by one leading to overall lower elastic energy.

The eviction of the atomic layer is therefore assisted by the strain induced interlayer transition and metastability of the 22 layered solid discussed above. Spallation is also facilitated if the atomic interactions are anisotropic so that attraction within layers is stronger than between layers (eg. graphite and layered oxides [89]), for our model, purely repulsive, hard disk solid, an effective, intralayer attractive potential of mean force is induced by the external potential [80].

The spallated solid layer emerges from the solid surface into the fluid, and travels a distance close to the mean free path; whereupon it disintegrates due to viscous dissipation (Fig. 6.5). To obtain the life time of the spallated layer we calculate the time development of the Fourier component of the local density correlation $\rho_{\mathbf{G}}(y, t)$ obtained by averaging, at each time slice t, the sum $\sum_{j=1,N} \exp(-i\,\mathbf{G} \cdot (\mathbf{r_j} - \mathbf{r_i}))$ over all particle positions $\mathbf{r_i}$ within a strip of width $\sim \sigma$ centered about y and spanning the system in x. The wavenumber $\mathbf{G} = (2\pi/d)\hat{\mathbf{n}}$ where $d = .92$ is the distance between crystal lines in the direction $\hat{\mathbf{n}}$ normal to the fluid-solid interface. The solid (central region with $\rho_{\mathbf{G}}(y, t) \neq 0$) ejects a layer (shown by an arrow in Fig. 6.5) which subsequently dissolves in the fluid. The lifetime of the layer is around 2-3 time units (τ) which translates to a few ps for typical atomic systems. The lifetime increases with decreasing viscosity of the surrounding fluid. Using the Enskog approximation [92] to the hard disk viscosity, we can
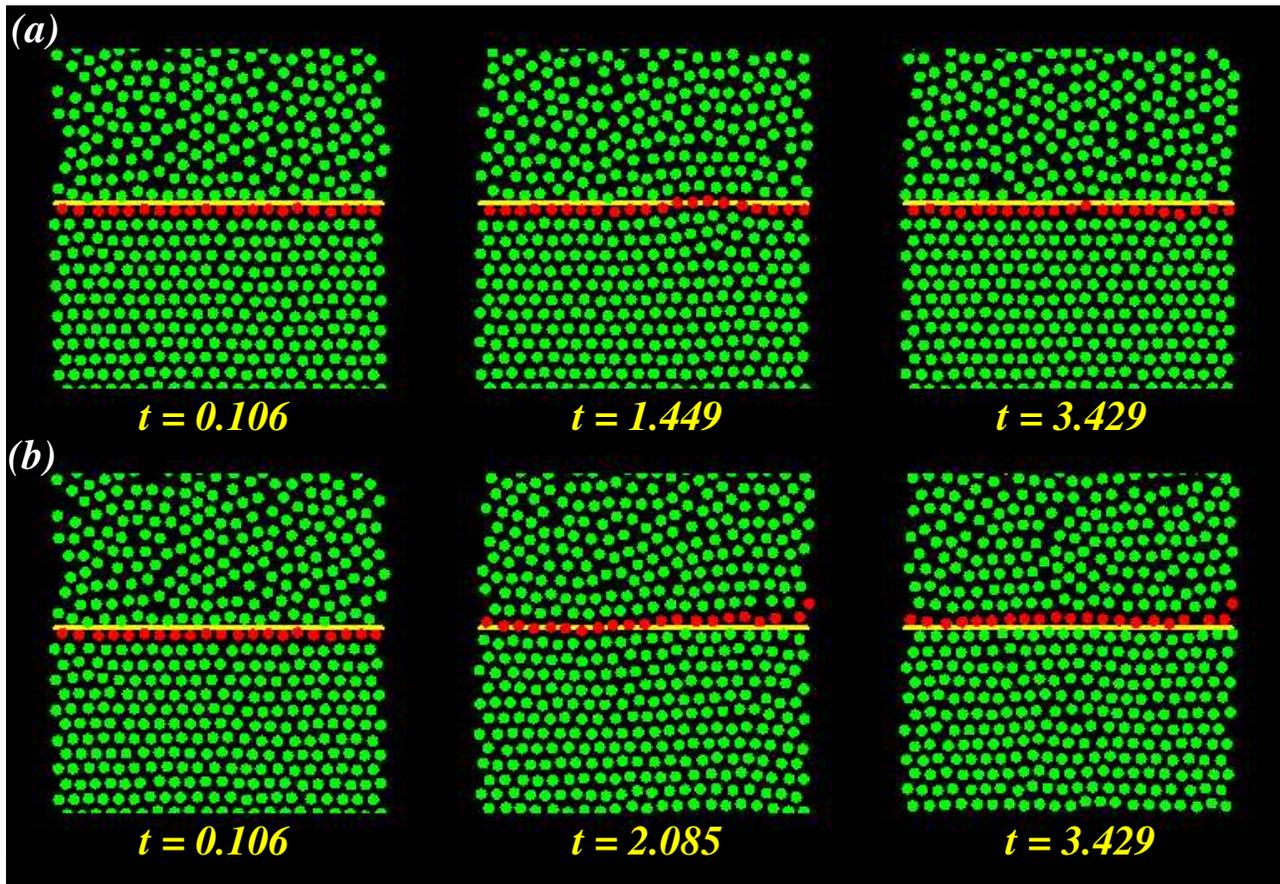
FIGURE 6.4: (a) Configuration snapshot from a portion of our MD cell showing hard disk atoms (green circles) at the solid (bottom)- liquid interface (yellow line) as a weak momentum pulse ($V_0 = 2.$) emerges into the liquid, at three different times, for $\mu = 4.8$. The pulse initially ejects a few atoms from the solid but are subsequently pulled back due to the large elastic strain cost in bending. of the interfacial crystalline layer (red circles) of a metastable (b) The same for a stronger momentum pulse, $V_0 = 6$. This time the pulse strength is sufficient to eject the layer.
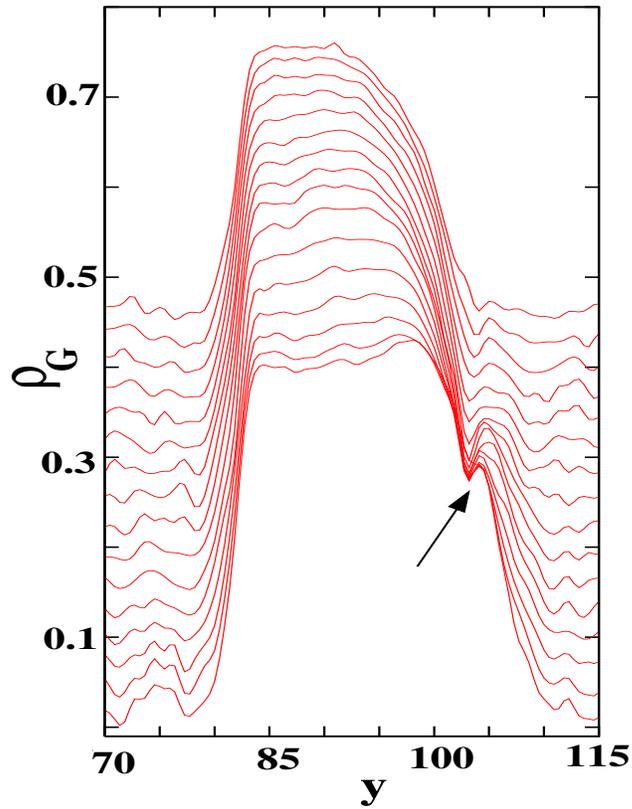
FIGURE 6.5: A plot of the time development $\rho_{\mathbf{G}}(y,t)$ The solid ejects a layer (shown by an arrow) which subsequently dissolves in the fluid. The curves from bottom to top correspond to time slices at intervals of $\Delta t = .07$ starting from $t = 1.06$ (bottom). We have shifted each curve upward by $.03t/\Delta t$ for clarity.

calculate the bulk viscosity for a hard disk fluid to be [92, 93]

$$\zeta_E = \frac{16}{\pi}\zeta_{00}\eta^2 g(\sigma) \qquad (6.1)$$

where ζ_{00} is a constant and $g(\sigma)$ is the pair-correlation function at contact which can be calculated using Eqn. (4.17) and Eqn. (4.18). For a system of hard disks with $m = \sigma = \beta = 1$, we can calculate [93] $\zeta_{00} = 1/2\sqrt{\pi}$. Thus, $\zeta_E \propto \eta^2$ and we estimate that by lowering the fluid density one may increase the lifetime of the layer considerably. The lifetime enhancement is even greater if the fluid in contact is a low density gas (when the interparticle potential has an attractive part [94]).
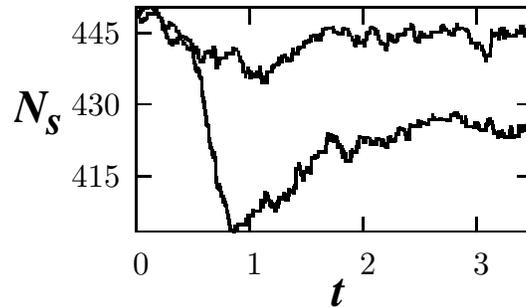
FIGURE 6.6: A plot of the total number of particles N_s within the solid region ($\mu = 4.8$) as a function of time for $V_0 = 1$. (top) and 6.. Note oscillations in N_s; only the stronger pulse changes the number of solid layers from 22 to 21.

6.4 Effective liquid theory

The absorption line -shape may be understood within a phenomenological "effective liquid" approximation. The extra absorption producing the prominent peak in Fig. 6.3 is due to the loss of a whole layer from the solid into the liquid (Fig. 6.4). For small V_0, the confined solid responds by centre of mass fluctuations ($q \rightarrow 0$ phonons) shown by oscillations of N_s with time (Fig. 6.6). Scattering from this and other sources [70, 86–88, 91] constitute a background which we ignore, as a first approximation, for simplicity. Within our approximation, the momentum loss at the interface is modelled as regular dissipation within a liquid strip of (fictitious) width ξ (see Fig. 6.7).
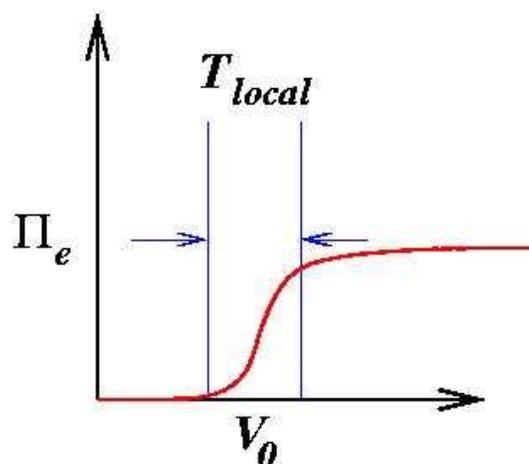
FIGURE 6.7: A cartoon diagram showing the momentum transfer as assumed in our phenomenological theory

The expected momentum transfer at the interface $\Pi_e = \Pi_0\times$ the probability that the momentum Π_0 required to eject the layer, exists. If a local "temperature" T_{local} measures the degree of (de)coherence of the momentum transfer, then $\Pi_e = (1/2)\Pi_0 \text{erfc}[(\Pi_0 - V_0)/\sqrt{2k_B T_{local}}]$ and ξ may be extracted from $V_0 - \Pi_e = V_0 \exp(-\alpha\omega^2\xi)$. Substituting for Π_e we obtain the extra absorption due to the interface,

$$\Delta^2 = 4.\alpha c_0^2 \xi = -a\log[1 - \frac{\Pi_0}{2V_0}\text{erfc}\{\frac{\Pi_0 - V_0}{\sqrt{2k_B T_{local}}}\}] \tag{6.2}$$

We use a, Π_0 and T_{local} as fitting parameters. In Fig. 6.3 we show a fit to Eq. 6.2 of our MD data and observe that it reproduces all the features remarkably well. The larger error-bars near the peak in $\Delta^2(V_0)$ reflects the difficulty of fitting a Gaussian to the transmitted pulse when dissipation is large. Indeed, in this region the pulse shape is systematically distorted away from Gaussian due to effects beyond the scope of our simple theory. Large fluctuations in N_s (Fig. 6.6) lead to expected [70, 86–88] and detectable decrease in average pulse speed (Fig. 6.8).
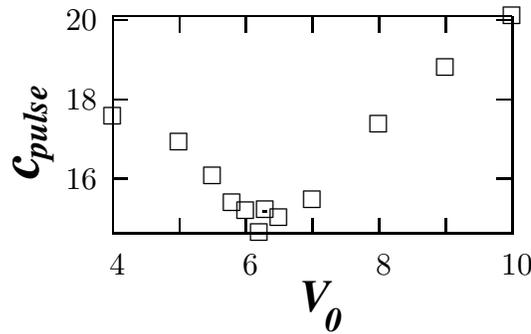
FIGURE 6.8: Average pulse velocity $c_{pulse}(V_0)$ for $\mu = 4.8$; note the dip in c_{pulse} where absorption is strongest.

6.5 Heat transport across the liquid - solid interface

In the last section we studied the effect of the layering transition on the transport of momentum across the liquid solid interface. In this section we shall focus on the transport of energy. The kinetic energy flux $\mathbf{j}_e$ is related to the temperature gradient $\nabla\mathcal{T}$ through the famous Fourier's law, viz.

$$\mathbf{j}_e = -\lambda\nabla\mathcal{T} \tag{6.3}$$

where, the transport coefficient λ is the thermal conductivity. The transport of heat through small and low dimensional system has enormous significance in the context of designing useful

nano-structures [91]. Heat transport across a model liquid solid interface has been studied in three dimensions with the interatomic potential being Lennard-Jones [95]. They have shown that the Kapitza resistance can reach appreciable values when the liquid does not wet the solid. In two dimensions, strictly speaking, Fourier's law needs to be modified by correction terms of the order of the logarithm of the system size [96]. For a small system, however, we shall ignore these corrections and assume it to be valid.

The specific context in which we study thermal properties of the liquid solid interface is the same as that we have used for our studies of the acoustic properties in the last section. Again, a solid region is created within a liquid using an external chemical potential trap. The overall dimensions of the system and the size of the solid region are also identical. The inter-atomic potential however is chosen to be soft sphere with the potential given by Eqn. 4.4. The smooth potential allows us to use standard MD simulations with a velocity Verlet algorithm. The time step of $\delta t = 10^{-3}$ in our MD ensures that the total energy is conserved (in equilibrium) to within 10^{-4}. Periodic boundary conditions are applied in the x-direction. A temperature gradient is generated throughout the simulation cell by coupling the two sides of the system in the y-direction to two reservoirs at different temperatures, which drives the system out of equilibrium. Thus we have a reservoir at $y = 0$ at a temperature $\mathcal{T}_1$ and another at $y = L_y$ at temperature $\mathcal{T}_2$. The coupling to the two reservoirs is implemented by the imposition of "Maxwell boundary conditions": when a particle hits the left (right) boundary it get reflected such that the velocity component parallel to the boundary (v_x) derives a new velocity from normal Maxwell distribution at the given temperature. The velocity component normal to the boundary (v_y) is taken from a Maxwell speed distribution given by

$$f_\alpha(d\mathbf{v}) = \frac{m^2}{2\pi(k_B\mathcal{T}_\alpha)^2}|v_y|\exp\left[-\frac{mv^2}{2k_B\mathcal{T}_\alpha}\right]d\mathbf{v} \qquad \alpha = 1, 2 \tag{6.4}$$

corresponding to a temperature $\mathcal{T}_1(\mathcal{T}_2)$ at the left (right) boundary. When the two temperatures are different, a net energy flux j_E in the y-direction results in the steady state condition, which is computed by averaging the kinetic energy added (or removed) by each reservoir per unit time and surface. Temperature profiles are obtained from the local kinetic energy density. We use the standard velocity Verlet scheme of molecular dynamics with equal time update, except when the particles collide with the "hard wall" reservoirs. We treat the collision between the particles and the reservoir as that between a hard disk of unit diameter colliding against a hard structure less wall. If the time, τ_c, of the next collision with any of the two reservoirs at either end is smaller than δt, the usual update time step of the MD simulation, we update the system with τ_c. During the collision with the walls Maxwell boundary conditions are imposed to simulate the velocity of an atom emerging from a reservoir at temperatures $\mathcal{T}_1$ or $\mathcal{T}_2$.

The system is allowed to reach the steady state where the current is the same in the entire system. To check for local thermal equilibrium , we first define the local temperature $\mathcal{T}(y) =$
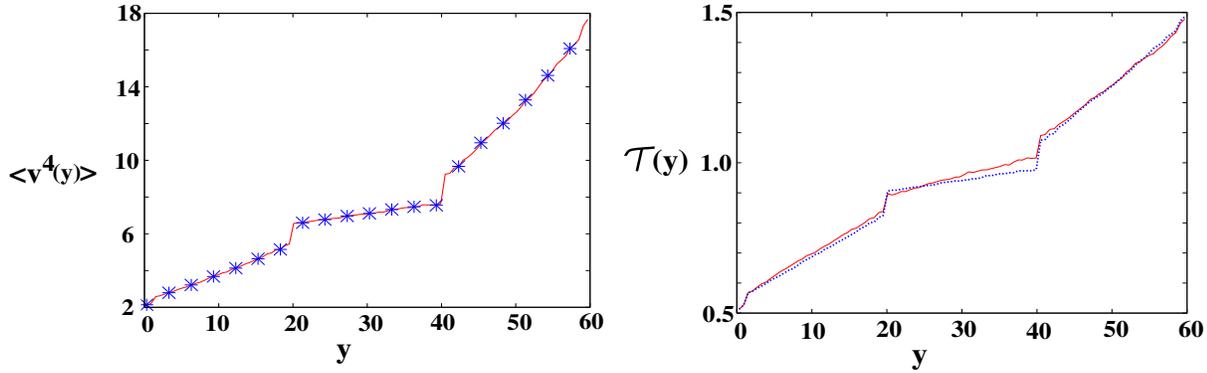
FIGURE 6.9: (a) $\langle v^4(y)\rangle$ and $8\mathcal{T}^2(y)$ as a function of y, the system coordinate perpendicular to the reservoirs, for $\mu = 8.0$. (b) $\mathcal{T}(y)$ as a function of y, the system coordinate perpendicular to the reservoirs, for $\mu = 7.0$ (Red line) and $\mu = 8.0$ (Blue line).

$\langle 1/2\; mv^2(y)\rangle$, where the averaging is done locally over strips parallel to the x-direction. This is called the kinematic temperature. In Fig. 6.9(a) we plot, from the MD simulations with $\mu = 8.0$, $\langle v^4 \rangle$ and see that it overlaps with $8\mathcal{T}^2$ locally. This is consistent with the thermodynamic relation $\langle v^4 \rangle = 8\mathcal{T}^2$. Thus the system preserves local thermal equilibrium. Note that this verification in turn justifies our definition of the local temperature. The temperature profile (Fig. 6.9(b)) shows that (1) the thermal conductivity of the solid region is larger than the liquid, which is expected because of the larger density of the former and (2) there is a significant jump in the temperature as one crosses the two interface. Such a jump in the temperature is also expected and is due to the Kapitza or contact resistance (R_K) [97]. This is defined as,

$$R_K = \frac{\Delta \mathcal{T}}{j_E} \tag{6.5}$$

where $\Delta \mathcal{T}$ is the difference in temperature across the interface. We are next interested in determining this Kapitza resistance across the solid liquid interface as a function of the strength of the external potential μ.

We have already seen that with increasing μ, the system shows a jump in the density of the solid region corresponding to the addition of an entire layer of atoms. From the profile shown in Fig. 6.9(b), the Kapitza resistance is easily obtained by dividing the temperature jump by the energy flux. Note that a slight dependence of R_K on $\mathcal{T}$ is visible in Fig. 6.9(b) with a larger temperature jump on the "warm" side. The results shown correspond to the average values of R_K between the "warm" and "cold" sides.

The plot of R_K as a function of μ shows a distinct jump as a layer is included (for a value of μ close to 7) in the solid region as shown in Fig. 6.10. The jump in R_K is also accompanied by a local peak at the transition. In Fig. 6.11 we have plotted the heat flux through the system
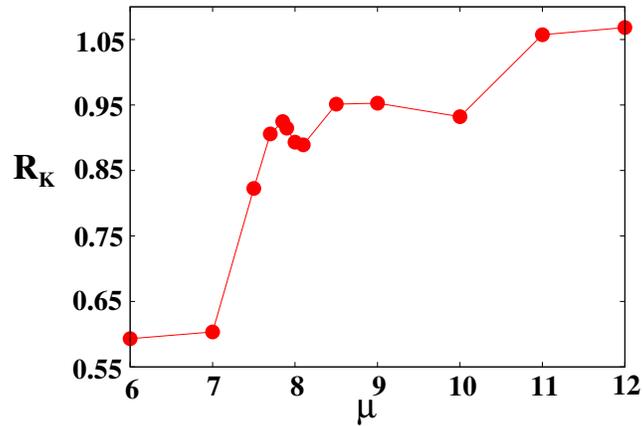
FIGURE 6.10: Plot of the Kapitza resistance, R_K, as a function of μ, shows a jump at the layering transition

as a function of μ. As μ increases, the atoms from the surrounding liquid get attracted into the potential well and the density of the liquid progressively becomes lower than that of the solid. This results in an overall decrease in the heat flux and consequently the overall conductivity. However, close to the layering transition at $\mu \sim 7-8$ there is a local peak in the value of the heat flux suggesting that a significant amount of kinetic energy is exchanged between the liquid and solid through the interface at the layering transition. The thermal conductivity of the solid λ_s also shows a peak at the transition (Fig. 6.12). The combined effect of the enhanced Kapitza resistance as well as enhanced conductivity of the solid can be summarized by defining
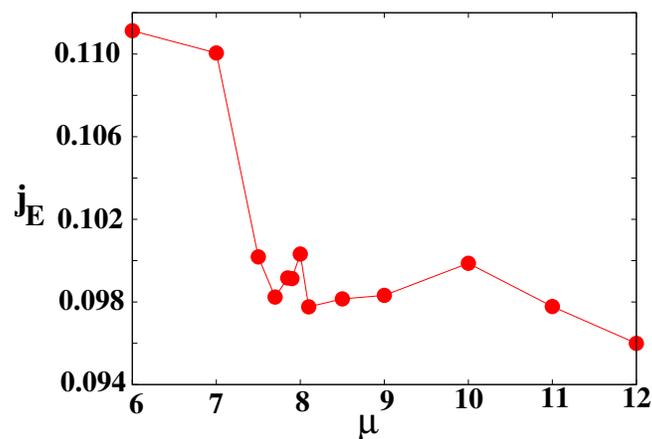
FIGURE 6.11: Plot of the heat flux, j_E, as a function of the trap depth, μ. Note that the overall flux decreases as a function of μ.
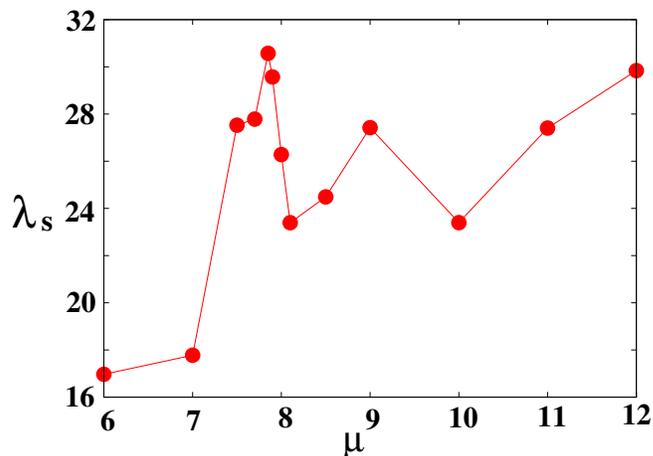
FIGURE 6.12: Plot of the thermal conductivity of the solid, λ_s as a function of μ. λ_s increases as the solid takes in a complete layer of atoms.

the Kapitza length l_K, which is the length of solid which has a thermal resistance equivalent to the liquid solid interface. This is reminiscent of the "effective liquid" concept which has been used in explaining some of the features of acoustic shock absorption in the last section. The Kapitza length is given by,

$$l_K = R_K \lambda_S \tag{6.6}$$

Note that substitution of the definition of the Kapitza length in the equation for the Kapitza
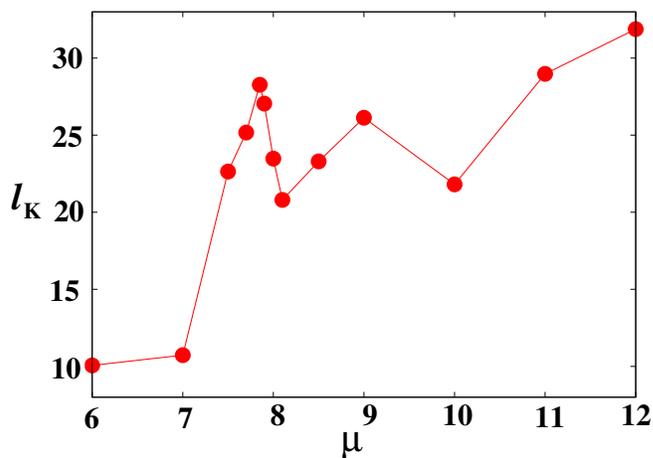
FIGURE 6.13: Plot of Kapitza length, l_K as a function of μ also shows a jump at the layering transition.

resistance (Eqn. 6.3) reproduces Fourier's law once the thermal gradient is identified with $\Delta\mathcal{T}/l_K$. The Kapitza length also shows a peak near the layering transition (Fig. 6.13).

With the help of these results we may conclude that the layering transition has a profound effect on the thermal properties of the liquid solid interface. An important consequence of this study is the possibility that the thermal resistance of interfaces may be altered using external potential which cause layering transitions in a trapped nano solid. We believe that this phenomenon has the potential for useful applications for e.g. as tunable thermal switches or other nano engineered devices.

References

[1] A. P. Sutton and R. W. Balluffi, *Interfaces in crystalline materials* (Oxford Science Pub., Oxford, New York, 1995).

[2] S. A. Safran, *Statistical Thermodynamics of Surfaces. Interfaces, and Membranes* (Addison Wesley, MA, 1994).

[3] S. M. Sze, *Physics of Semiconductor Devices* (Wiley, New York, 1981).

[4] E. H. Rhoderick and R. H. Williams, *Metal-semiconductor contacts* (Oxford University Press, Oxford, 1988).

[5] D. W. Niles and G. Margaritondo, in *Materials Interfaces*, edited by D. Wolf and S. Yip (Chapman and Hall, London, England, 1992).

[6] W. W. Mullins and R. F. Sekerka, J. Appl. Phys. **35**, 444 (1964).

[7] M. J. Rosen, *Surfactants and interfacial phenomena* (Wiley, New York, 1989).

[8] V. Balzani, M. Venturi, and A. Credi, *Molecular devices and machines : a journey into the nano world* (Wiley-VCH, Weinheim, 2003).

[9] J. W. Cahn, in *American Society for Metals*, edited by W. C. Johnson and J. M. Blakely (Metals Park, Ohio, 1979), p. 3.

[10] A. L. Barabasi and H. E. Stanley, *Fractal Concepts in Crystal Growth* (Cambridge University Press, Cambridge, England, 1995).

[11] S. Balibar, H. Alles, and A. Y. Parshin, Rev. Mod. Phys. **77**, 317 (2005).

[12] C. L. Wang and G. Agnolet, Phys. Rev. Lett. **69**, 2102 (1992).

[13] S. Balibar and B. Castaing, Surface Science Reports **5**, 87 (1985).

[14] S. F. Edwards and D. R. Wilkinson, Proc. Roy. Soc. London A **381**, 17 (1982).

[15] M. Kardar, G.Parisi, and Y.C.Zhang, Phys. Rev. Lett. **56**, 889 (1986).

[16] F. Family, J. Phys. A: Math. Gen. **19**, L441 (1986).

[17] S. K. Ma, *Statistical Mechanics* (World Scientific, Singapore, 1985).

[18] S. F. Edwardst and P. W. Anderson, J. Phys. F **5**, 965 (1975).

[19] D. J. Amit, H. Gutfreund, and H. Sompolinsky, Phys. Rev. A **32**, 1007 (1985).

[20] J. Toner and Y. Tu, Phys. Rev. Lett. **75**, 4326 (1995).

[21] J. J. Rice, G. Stolovitzky, Y. Tu, and P. de Tombey, Biophysical Journal **84**, 897 (2003).

[22] S. Galam, cond-mat/9702163 (unpublished).

[23] E. Ising, Z. Physik **31**, 253 (1925).

[24] W. Lenz, Z. Physik **21**, 613 (1920).

[25] W. Heisenberg, Z. Physik **49**, 619 (1928).

[26] R. Peierls, Proc. Cambridge Phil. Soc. **32**, 477 (1936).

[27] H. A. Kramers and G. H. Wannier, Phys. Rev. **60**, 252 (1941).

[28] E. Montroll, J. Chem. Phys. **9**, 706 (1941).

[29] E. Montroll, J. Chem. Phys. **10**, 61 (1942).

[30] R. Kubo, Busseiron-kenkyu **1**, 1 (1943).

[31] L. Onsager, Phys. Rev. **65**, 117 (1944).

[32] T. Saha, I. Dasgupta, and A. Mookerjee, J. Phys.: Condens. Matter **8**, 1979 (1996).

[33] P. M. Chaikin and T. C. Lubensky, *Principles of condensed matter physics* (Cambridge University Press, New York, 1995).

[34] N. Goldenfeld, *Lectures on Phase Transitions and the Renormalization Group* (Perseus Publishing, ADDRESS, 1992).

[35] S. N. Majumdar and M. Barma, Physica **177A**, 366 (1991).

[36] M. Barma, in *Non Linear Phenomena in Materials Science III*, edited by G.Ananthakrishna, L.P.Kubin, and G.Martin (SciTech Publications, Zurich, Switzerland, 1995), Vol. 42-43, p. 19.

[37] M. Barma, J. Phys. A: Math. Gen. **25**, L693 (1992).

[38] S. N. Majumdar and M. Barma, Phys. Rev. B **44**, 5306 (1991).

[39] Note that $f(Y, t)$ in Eq. (2.24) generates a space and time dependent, (annealed) random, Galilean boost. Random Galilean transformations often lead to multifractal steady states; see for eg. U. Frish, *Turbulence* (Cambridge University Press, 1995) .

[40] T. M. Ligget, *Interacting Particle Systems* (Springer, New York, 1985).

[41] N. Rajewsky, L. Santen, A. Schadschneider, and M. Schreckenberg, J. Stat. Phys. **92**, 151 (1998).

[42] H. van Beijeren, R. Kutner, and H. Spohn, Phys. Rev. Lett. **54**, 2026 (1985).

[43] M. J. Lighthill and G. B. Whitham, Proc. Roy. Soc. London A **229**, 282 (1955).

[44] D. Kandel and E. Kaxiras, cond-mat/0402116 (unpublished).

[45] R. K. *et. al.*, *Current Topics in Materials Science* (North Holland, Amsterdam, 1997).

[46] D. Zhao, F. Liu, D. L. Huber, and M. G. Lagally, Phys. Rev. B **62**, 11316 (2000).

[47] R. W. Cahn and P. Haasen, *Physical Metallurgy* (North-Holland, Amsterdam, 1996).

[48] P. W. Stephens, P. Heiney, R. J. Birgeneau, and P. M. Horn, Phys. Rev. Lett. **43**, 47 (1979).

[49] B. D. Krack, V. Ozolins, M. Asta, and I. Daruka, Phys. Rev. Lett. **88**, 186101 (2002).

[50] V. L. Pokrovsky and A. L. Talopov, Soviet Science Reviews (1985).

[51] ϕ represents any scalar order parameter with $h(y, t)$ a field conjugate to ϕ, eg. number density and chemical potential for a growing gas -solid surface .

[52] A. L. C. Ferreira, S. K. Mendiratta, and E. S. Lage, J. Phys. A: Math. Gen. **22**, L431 (1989).

[53] S. N. Majumdar and P. L. Krapivsky, Phys. Rev. E **63**, 45101(R) (2001).

[54] A. Chaudhuri and S. Sengupta, Physica A **318**, 30 (2003).

[55] Y. Frenkel and T. Kontorowa, Zh. Eksp. Teor. Fiz. **8**, 1340 (1938).

[56] P. Bak, D. Mukamel, J. Villain, and K. Wentowska, Phys. Rev. B **19**, 1610 (1979).

[57] A. A. Middleton, O. Biham, P. B. Littlewood, and P. Sibani, Phys. Rev. Lett. **68**, 1586 (1992).

[58] S. Alexander, J. Bernasconi, W. R. Schneider, and R. Orbach, Rev. Mod. Phys. **53**, 175 (1981).

[59] H. Löwen, *Lecture Notes in Physics* (Springer-Verlag, Heidelberg, 2000).

[60] K. J. Strandburg, Rev. Mod. Phys. **60**, 161 (1988).

[61] S. Sengupta, P. Nielaba, and K. Binder, Phys. Rev. E **61**, 6294 (2000).

[62] J. Q. Broughton, G. H. Gilmer, and J. D. Weeks, Phys. Rev. B **25**, 4651 (1982).

[63] J. P. Hansen and I. R. McDonald, *Theory of simple liquids* (Elsevier Academic Press, London, UK, 1986).

[64] D. Frenkel and B. Smit, *Understanding Molecular Simulations* (North Holland, Amsterdam, 2000).

[65] M. P. Allen and D. J. Tildesley, *Computer Simulation of Liquids* (Oxford University Press, New York, 1987).

[66] S. Toxvaerd, Phys. Rev. A **24**, 2735 (1981).

[67] F. H. Ree and W. G. Hoover, J. Chem. Phys. **40**, 939 (1964).

[68] F. L. Román, A. Gonzáles, J. A. White, and L. Velasco, Am. J. Phys. **70**, 847 (2002).

[69] A. Santos, M. L. de Haro, and S. B. Yuste, J. Chem. Phys. **103**, 4622 (1995).

[70] L. D. Landau and E. M. Lifshitz, *Fluid Mechanics*, 2nd ed. (Pergamon Press, Oxford, 1987).

[71] T. V. Ramakrishnan and M. Yussouff, Phys. Rev. B **19**, 2775 (1979).

[72] C. Godreche, *Solids far from equilibrium* (Cambridge University Press, New York, 1991).

[73] A. D. J. Haymet and D. W. Oxtoby, J. Chem. Phys. **74**, 2559 (1981).

[74] A. D. J. Haymet and D. W. Oxtoby, J. Chem. Phys. **76**, 6262 (1982).

[75] I. W. Hamley, *Introduction to Soft Matter: polymer, colloids, amphiphiles and liquid crystals* (Wiley, Cluchester, 2000).

[76] J. P. Hoogenboom *et al.*, Appl. Phys. Lett. **80**, 4828 (2002).

[77] J. Baumgartl, M. Brunner, and C. Bechinger, Phys. Rev. Lett. **93**, 168301 (2004).

[78] W. D. Phillips, Rev. Mod. Phys. **70**, 721 (1998).

[79] A. Jaster, Physica A **277**, 106 (2000).

[80] D. Chaudhuri and S. Sengupta, Phys. Rev. Lett. **93**, 115702 (2004).

[81] L. D. Landau and E. M. Lifshitz, *Theory of Elasticity*, 2nd ed. (Pergamon Press, Oxford, 1987).

[82] J. Fineberg and M. Marder, Phys. Rep. **313**, 1 (1999).

[83] *et al.*. U. Landman, Science **248**, 454 (1990).

[84] A. Sutton and J. Pethica, J. Phys.: Condens. Matter **2**, 5317 (1990).

[85] H. J. Metcalf and P. van der Straten, *Laser Cooling and Trapping* (Springer, Heidelberg, 1999).

[86] C. Zener, Phys. Rev. **53**, 90 (1938).

[87] M. A. Isakovich, Zh. Ek. Teor. Fiz. **18**, 907 (1948).

[88] A. Onuki, Phys. Rev. A **43**, 6740 (1991).

[89] K. S. Novoselov, Proc. Nat. Acad. Sc. **102**, 10451 (2005).

[90] Y. B. Zeldovich and Y. P. Raizer, *Physics of Shock Waves and High-Temperature Hydrodynamic Phenomena* (Dover Publications, New York, 2002).

[91] D. G. Cahill *et al.*, J. Appl. Phys. **93**, 793 (2003).

[92] S. Chapman and T. G. Cowling, *The Mathematical Theory of Non-uniform Gases*, 3rd ed. (Cambridge University Press, London, 1970).

[93] J. J. Erpenbeck and W. W. Wood, Phys. Rev. A **26**, 1648 (1982).

[94] W. G. Hoover *et al.*, Phys. Rev. A **22**, 1690 (1980).

[95] J.-L. Barrat and F. Chiaruttini, Molecular Physics **101**, 1605 (2003).

[96] F. Bonetto, J. L. Lebowitz, and L. Rey-Bellet, math-ph/0002052 (unpublished).

[97] G. L. Pollack, Rev. Mod. Phys. **41**, 48 (1969).